MODELING SOLID PROPELLANT STRAND BURNER EXPERIMENTS WITH CATALYTIC NANOPARTICLE ADDITIVES

A Dissertation

by

COREY ANTHONY FRAZIER

Submitted to the Office of Graduate Studies of
Texas A&M University
in partial fulfillment of the requirements for the degree of

DOCTOR OF PHILOSOPHY

December 2011

Major Subject: Mechanical Engineering

Modeling Solid Propellant Strand Burner Experiments

with Catalytic Additives

MODELING SOLID PROPELLANT STRAND BURNER EXPERIMENTS WITH CATALYTIC ADDITIVES

A Dissertation

by

COREY ANTHONY FRAZIER

Submitted to the Office of Graduate Studies of
Texas A&M University
in partial fulfillment of the requirements for the degree of

DOCTOR OF PHILOSOPHY

Approved by:

Chair of Committee,	Eric Petersen
Committee Members,	Kalyan Annamalai
	Timothy Jacobs
	Adonios Karpetis
Head of Department,	Jerald Caton

December 2011

Major Subject: Mechanical Engineering

ABSTRACT

Modeling Solid Propellant Strand Burner Experiments

with Catalytic Additives. (December 2011)

Corey Anthony Frazier, B.S.; M.S., University of Central Florida

Chair of Advisory Committee: Dr. Eric L. Petersen

This dissertation studies how nanoadditives influence burning rates through the development and use of a model to conduct parametric studies on nanoadditive interaction and to formulate theories. Decades of research have yet to determine the specific mechanisms for additive influence and the theories remain diverse and fragmented. It has been theorized that additives catalyze the combustion and thermal decomposition of AP, influence the condensed phases, and enhance the pyrolysis and regression of the binder. The main focus of the thesis was to approximate the enhanced burning rates seen in the author's laboratory using spray-dried, spray-dried/heat-treated, and premixed TiO_2 nanoadditives with ammonium perchlorate (AP) / hydroxyl-terminated polybutadiene (HTPB) composite propellants. The model is based on the classic Beckstead-Derr-Price (BDP) and Cohen-Strand models and contains a component that determines the pressure changes within the strand burner during a test. The model accurately predicts measured burning rates for baseline propellants without additives over a range of 500 – 3000 psi within 10%. The strand burner component of the model predicts the experimental pressure trace accurately. Further, the strand burner

component determines an average burning rate over time and predicts a transient burning rate if provided a pressure trace.

A parametric study with the model parameters determined that the nanoadditives appear to be increasing the AP condensed phase reaction rate. This conclusion was drawn because only changes in AP condensed-phase reaction rate would adequately and realistically replicate burning rate enhancements seen in laboratory experiments. Parametric studies with binder kinetics, binder regression rate, AP surface kinetics, and primary flame kinetics produced burning rate behavior that did not match that seen in experiments with the additives. The model was further used to develop a theory for how the nanoadditive affects the AP condensed phase, and a new parameter, Ω_c, that influences the AP condensed phase reaction rate was created that replicates spray-dried, spray-dried/heat-treated, and premixed TiO_2 nanoadditive experimental burning rates.

Finally, the model was used to develop a first approximation of predicting anomalous burning rate trends such as a negative pressure dependence and extinguishment. A new term, M_c, that modifies the ratio of binder mass flux to oxidizer mass flux is used in tandem with Ω_c to develop a negative burning rate trend that is close to the experimental result.

ACKNOWLEDGMENTS

I would like to thank my committee chair, Dr. Eric Petersen for his time, effort, guidance, and as usual, his patience in developing me as an engineer and scientist. Also, I appreciate the time and guidance of my committee members, Dr. Kalyan Annamalai, Dr. Timothy Jacobs, and Dr. Adonios Karpetis, for their guidance and support throughout the course of this research. I would also like to thank Dr. Tahir Cagin for his time and input regarding my research.

I want to extend gratitude to my research colleagues who have supported, guided, and educated me over the years including, but not limited to, Kevin Kreitz, Matthew Stephens, Jeffery Johnson, Tyler Allen, Mitch Johnson, Sean Baker, Thomas Sammet, Andrew Demko, and David Reid. My special thanks are also extended to Brandon Rotavera and Christopher Aul as well for their support with software, software literature, and assistance in understanding various thermofluid principles.

Finally, it would be in poor taste to not acknowledge the incredible contributions of my parents, Anthony and Valerie Frazier. Their support over the past 10 years of higher learning is a small representation of how much they have invested in me over the past 30 years with their time, patience, support, and love. No matter how financially affluent I become, no matter the amount on the check, I will always be at least $0.01 shy of paying you back for all you've done.

NOMENCLATURE

a	Temperature Coefficient
A	Area
A_{AP}	Reaction rate of Monopropellant Flame combustion
A_{binder}	Reaction rate of the binder pyrolysis
A_{fh}	Ratio of (1) the peak diffusion distance of the pyrolysis products into the oxidizer stream to (2) the maximum heat transfer distance of the Primary Flame
AMPAC	Advanced Materials Processing and Analysis Center
A_{ox}	Reaction rate of AP gas phase decomposition
AP	Ammonium Perchlorate (NH_4ClO_4)
A_s	Reaction rate of AP condensed phase decomposition
BDP	Beckstead-Derr-Price
CEA	Chemical Equilibrium Analysis
CeO_2	Cerium Oxide; “Ceria”
C_g	AP gas phase specific heat
C_p	Specific heat (at constant pressure)
C_s	AP condensed phase specific heat
C_v	Specific heat (at constant volume)
D, D_{ox}	Oxidizer crystal diameter
DAQ	Data Acquisition

DOA	Dioctyl Adepate
E_{AP}	Activation energy of Monopropellant Flame combustion
E_{binder}	Activation energy of the binder pyrolysis
E_{ox}	Activation energy of AP gas phase decomposition
E_s	Activation energy of AP condensed phase decomposition
Fe_2O_3	Iron oxide or Ferric oxide; rust
g	Gravity (for internal energy considerations)
h, H	Enthalpy
h	Height of AP crystal above or below the propellant surface
h	Convection heat transfer coefficient
HTPB	Hydroxyl-Terminated Polybutadiene ($C_{667}H_{999}O_5$)
IPDI	Isophorone Diisocyanate
k	Thermal conductivity (for heat transfer in strand burner model)
k_{PF}	Pressure-dependent reaction rate in the Primary Flame
m	Mass flux of oxidizer, binder, entire propellant, Primary Flame, or Monopropellant Flame
M_i	Molecular weight of individual gas species
M_{mix}	Molecular weight of strand burner gas mixture
M_c	Binder-to-oxidizer mass flux ratio factor
Micron	Shortened form of “micrometer”
n	Combustion Index or pressure exponent
n	Number of moles of a gas species or gas mixture

P	Pressure
PEP	Propellant Evaluation Program
PF	Primary Flame
Q_{AP}	Heat release of the Monopropellant Flame
Q_{binder}	Heat of pyrolysis of binder (endothermic)
q_{cv}	Heat energy on a per unit mass basis
Q_F	Adiabatic heat content of the AP crystal ($Q_L + Q_{AP}$)
Q_{FF}	Heat release of the Final Flame
Q_L	Heat of vaporization of AP
Q_{PF}	Heat release of the Primary Flame
r	Burning rate
R	Universal Gas Constant
S	Surface area (or AP or binder) or surface area ratio (divided by the total surface area)
SEM	Scanning Electron Microscope
TiO_2	"Titania" or "Titanium Dioxide"
T	Temperature
t	Time
T_{AF}	Adiabatic flame temperature
T_o	Initial Temperature
T_{ref}	Reference Temperature (for enthalpy calculations)
V	Volume

V	Velocity (for internal energy calculations)
x	Length, distance
x_i	mass fraction of individual gas species
X^*_D	Diffusion distance of pyrolysis products above AP surface
X^*_{FF}	Standoff distance of Final Flame above AP surface
X^*_{PDF}	Standoff distance of Primary Diffusion Flame (standoff distance of Primary Flame and diffusion distance above AP surface, $X^*_D + X^*_{PF}$)
X^*_{PF}	Standoff distance of Primary Flame above AP surface
X^*_{ox}	Standoff distance of Monopropellant Flame above AP surface
y_i	mole fraction of individual gas species
z	Distance potential (for internal energy)
α	Thermal diffusivity
α_{ox}	mass loading of AP (by percent)
α_{binder}	mass loading of binder (by percent)
β_F	Percentage of gasified AP participating in Primary Flame reactions
β_p	Percentage of AP decomposition occurring in the gas phase
B_{ox}	Percentage of energy from AP decomposition products used to heat oxidizer crystal (determines Primary Flame energy used to heat oxidizer versus that of crystal)
ΔH_s	Endothermic heating requirements of AP solid

ΔH_{ev}	AP heat of vaporization at 298K
ΔH_g	Endothermic heating requirements of AP decomposition products
δ_{PF}	Primary Flame reaction order (influences pressure dependence on Primary Flame reaction rates)
γ	Specific heat ratio
λ	Thermal conductivity of AP gas (combustion model)
Ω_c	AP condensed phase reaction rate factor
ϕ	Air-to-fuel ratio
ρ	Density
ζ^*_{PF}	Dimensionless standoff distance of Primary Flame above AP surface
ζ^*_{ox}	Dimensionless standoff distance of Monopropellant Flame above AP surface

TABLE OF CONTENTS

Page

Page

LIST OF FIGURES

Page

Page

Page

Page

LIST OF TABLES

1. INTRODUCTION

Solid propellants are solid-phase combinations of energetic materials consisting of a fuel and an oxidizer. Their application spans multiple industries: space transportation via the production of thrust directed through a nozzle; the filling of expanding membranes such as automotive airbags; defense applications such as ammunition cartridges and long-range armaments; and the extraction of geological resources by perforating rock to release or expose deposits.

The performance of a solid propellant is typically determined by its experimentally measured burning rate as a function of pressure. Traditional solid propellant performance shows a direct, linear relationship between burning rate and pressure when plotted on a log-log scale. Nanoparticle additives are of interest due to their potentially high reactivity, high catalytic activity, and high surface-area-to-mass ratio which are suspected to influence propellant burning rates through catalytic reactions – resulting in significantly increased burning rates (Kreitz, 2010; Kreitz et al., 2011; Reid et al., 2011). These catalysts are often metal oxides such as TiO_2, CeO_2, or Fe_2O_3 and can be "doped," or impregnated, with another element such as aluminum or gadolinium to influence performance. Additives also allow departure from a P^n burning trend and can provide the propellant with "anomalous burning behaviors" (such as plateau burning, a damped burning rate response to increasing pressure, and mesa

---

This dissertation follows the style of the *Combustion Science and Technology Journal.*

behavior, a negative dependence on pressure) that are non-linear relationships between burning rate and pressure often desired in modern propellants (Reid et al., 2007; Stephens et al., 2008).

Previous combustion models have focused on the burning of propellants without the presence of additives (Beckstead et al., 1970; Cohen and Strand, 1982; and Cai et al., 2008). To support laboratory tests, a propellant burning model that captures the effect of nanoparticle additives on performance is desired. To the author's knowledge, no integrated model exists for composite propellants, specifically ammonium perchlorate (AP) and hydroxyl-terminated polybutadiene (HTPB), with nanoparticle additives that describes the complete burning of the propellant – including burning rate, chemical kinetics, and thermodynamic interactions within the strand burner. Such a model would support parametric studies on propellant performance and lend insight into trends seen in the experiments and eventually leading to more robust additives.

The overall goal of this research was to better understand how nanocatalytic additives influence the burning rate of solid propellants, develop an applicable theory, and accurately model burning rate enhancements. In support of this goal, it was necessary to develop a model that completely complements burning rate experiments being conducted at Texas A&M University. The model (based on thermodynamics, heat transfer, and combustion principles) needed to predict the burning rate of basic composite propellant formulations and those with additive enhancements. The resulting model is to support parametric studies on propellant performance and lend insight into the trends seen in strand burner experiments. Moreover, the model should completely

describe the propellant burning experiment. This requirement means that the model needed to mimic the pressure rise during the burn and any heat loss during and after the burn. This capability created a complete pressure trace similar to that seen in experiments. The model needed to also be capable of inferring burning rate from an actual set of pressure trace data.

The objectives served the purpose of determining how to incorporate the effects of nanoparticle additives into the overall model. The effects were utilized to develop correlations for replicating burning rate enhancements seen in laboratory experiments, and these parameters provided insight into the physical reasoning for the burning rate enhancements. Finally, the completed model was used to conduct anomalous burning rate parametric studies which provides the first step toward the development of an anomalous burning rate theory to be validated in future experiments and refined in further studies.

Section two provides an overview of solid propellants and a brief review of basic thermodynamic principles used in this study to model experiments. Section three discusses the modeling method and discusses how parameters in the model interact to predict burning rates. Section four provides model-predicted results for baseline propellant formulations. Section five contains the parametric study performed to ascertain what aspects of the model are influenced by nanoparticles and then section six provides the modeling and results for mimicking experimental burning rate enhancements. Section seven details model prediction of anomalous burning trends. Finally, section eight summarizes the results and conclusions identified from this thesis.

2. BACKGROUND

2.1 Overview of Solid Propellants

Solid propellants are composite chemical formulations used to create a mechanical force resulting from the expulsion of pressurized combustion products at a high rate. They contain an oxidizer and a fuel (which may be one in the same for a given component) and as such undergo self-sustaining combustion regardless of environment. A composite solid propellant generally consists of a fuel, an oxidizer, and a binder (which may also act as the fuel) to suspend the solid fuel and oxidizer. In certain situations, a propellant may consist of only one substance capable of self-deflagration, called a "monopropellant." In regards to this particular study, the fuel and binder is hydroxyl-terminated polybutadiene, or HTPB, a viscous polymer prior to mixing into the propellant, and the oxidizer is ammonium perchlorate (AP), a salt-like crystal which is also a monopropellant. According to Sutton and Biblarz (2001), the composite propellant is cured into a solid strand sample (Figure 1) for use in testing by curatives or plasticizers such as isophorone diisocyanate (IPDI), dioctyl adepate (DOA), and HX-752 bonding agent which are included in the formulation but are usually negligible participants in the combustion process due to low concentration and reactivity. Additives, such as TiO_2, may also be used to modify the performance of the formulation when burned. An illustration of a typical solid propellant cross section can be seen in Figure 2.

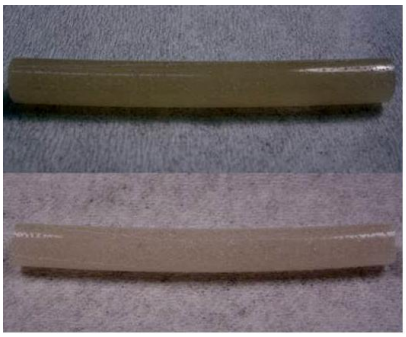

Figure 1: Cured, one-inch solid composite propellant strands prior to processing for burning rate experiments.

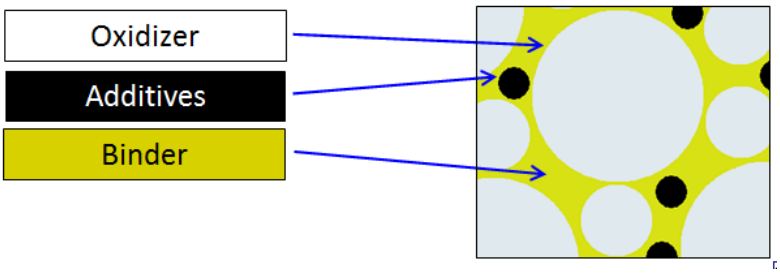

Figure 2: Illustration of a solid composite propellant cross section. The oxidizer crystals (white) and additives (black) are represented by colored regions suspended in the binder (yellow).

2.2 Evaluation of Solid Propellant Burning Rates

Propellant burning rates are the metric commonly chosen to quantify the performance of a propellant formulation. In relation to the aerospace industry, solid propellants are burned in a laboratory setting at given pressures reminiscent of those seen in solid rocket motors, and the resulting burning rates are plotted as a function of simulated pressure. According to Sutton and Biblarz, pressure and burning rate are

related by a power function, or "power law," which is also known as "St. Robert's Law" or "Vielle's Law" (Equation 1).

$$r = aP^n \tag{1}$$

In Equation 1, r is the burning rate, a is an experimentally determined constant known as the temperature coefficient, P is the test pressure, and n is the burning rate exponent or pressure index. When burning rate is plotted as a function of pressure on a log-log scale, a typical propellant formulation displays a linear relationship fitted to Equation 1 (illustrated in Figure 3).

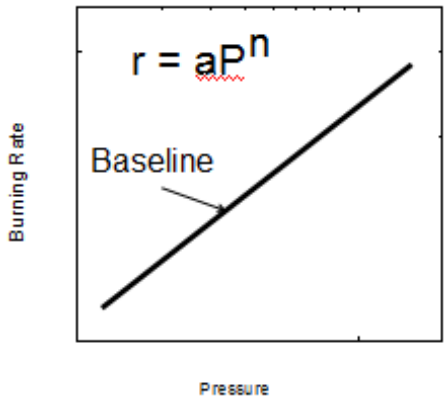

Figure 3: Illustration of the linear relationship between burning rate and pressure when plotted on a log-log scale. The line of fit is defined by the power law (Equation 1).

The oxidizer of a solid composite propellant plays a pivotal role in influencing the burning rate due to its concentration (or mass "loading"), particle size, and

combinations of particle sizes utilized (or "modes"). The loading of AP by percent mass, also known as α_{ox}, influences oxidizer-fuel ratios which drive adiabatic flame temperature. Figure 4 contains a series of flame temperatures obtained from Cohen and Strand (1982). It shows that as α_{ox} increases for a composite propellant of AP/HTPB formulation, the adiabatic flame temperature increases, until ~88% AP mass loading, at which point the propellant burns stoichiometrically with all the AP being consumed, reaching an adiabatic flame temperature of ~3000K at $\alpha_{ox} = 0.88$. The chemical reaction for AP and HTPB, based on mass fraction, is

$$0.12C_{667}H_{999}O_5 + 0.88NH_4ClO_4 \rightarrow 0.284H_2O + 0.257HCl + 0.205CO_2 + 0.116CO + 0.104N_2 + 0.004H_2 + 0.009OH + 0.016Cl + 0.003O_2 + 0.002NO$$

where the mass fractions of the products may change with pressure. Some products exist with a mass fraction less than 0.1%: H, O, Cl_2, HClO, CClO, ClO, HCO, NH_3, HNO, N, NO_2, NClO, NH_2, HO_2, and N_2O. Due to the vast array of HTPB variants, the R45M variant is used in the reaction as this HTPB-type is utilized in laboratory experiments. The products of HTPB pyrolysis include, but are not limited to, C, CH_2, CH_3, CH_4, C_2H_3, C_4H_6, and H_2.

When $\alpha_{ox} = 1$, the solid propellant burns as an AP monopropellant with an adiabatic flame temperature of ~1400K. The chemical reaction for AP monopropellant burning, based on mass fraction, is

$$AP_{decomp} \rightarrow 0.242H_2O + 0.329O_2 + 0.259HCl + 0.119N_2 + 0.049Cl_2$$

where "AP_{decomp}" is a collective term for all of the AP thermal decomposition products prior to reacting in the flame. It should be noted that the mass fractions of the various constituents changes with pressure and that some products exist with a mass fraction less than 0.1%: Cl, NO, HClO, ClO, OH, NO_2, NClO, HO_2, and HNO_2. The thermal decomposition of 1 mole of AP produces products in the following mole concentrations

$$NH_4ClO_4 \rightarrow NH_3 + HClO_4 \rightarrow 1.62H_2O + 1.105O_2 + 0.265N_2 + 0.12N_2O + 0.23NO + 0.76HCl + 0.12Cl_2$$

from Guirao and Williams (1971). While a specified amount of AP crystal produces the decomposition products in the aforementioned concentrations, the thermal decomposition of AP actually follows multiple mechanisms which are detailed later in this study.

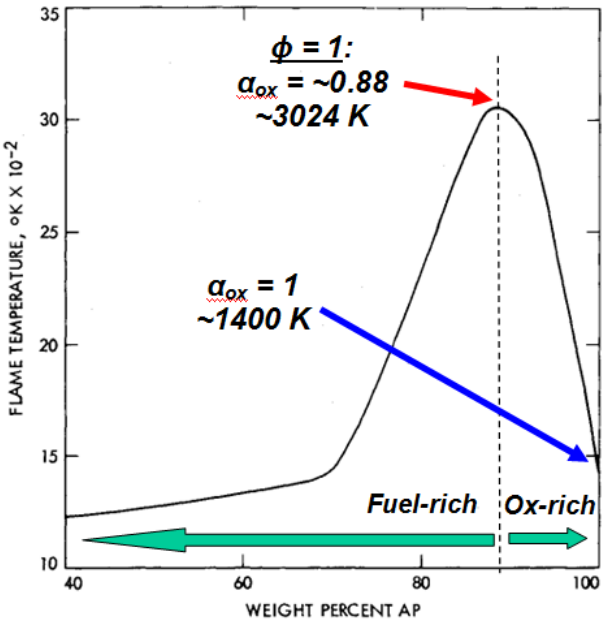

Figure 4: The effect of AP% mass loading on adiabatic flame temperature for an AP/HTPB solid composite propellant (modified from Cohen and Strand, 1982). The stoichiometric condition is at approximately 88% AP / 12% HTPB.

AP particle size reduction allows for better dispersion throughout the propellant and an increased reactivity with the binder. This reduction in AP particle size causes combustion behavior between the AP and HTPB reactants to resemble a premixed regime in which the reaction takes place faster and the flame burns hotter resulting in an increased burning rate. Jeppson et al. (1998), provided an illustration of the effect of AP particle size on burning rate showing that decreasing particle size changes the combustion regimes (Figure 5). Conversely, larger AP particle sizes tend to burn as an AP monopropellant flame (Figure 5).

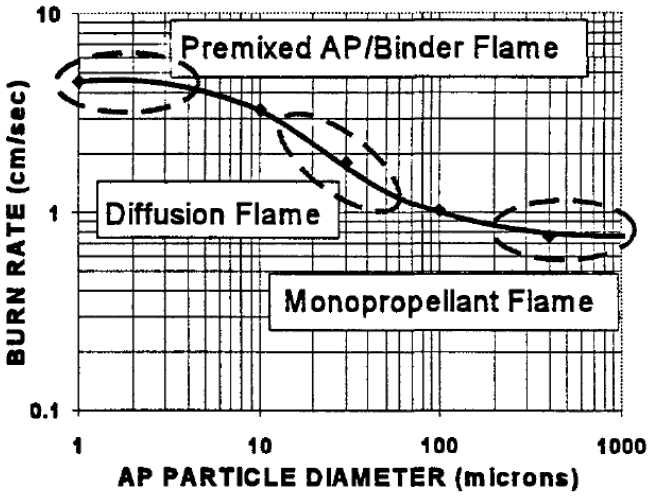

Figure 5: Effect of particle size on the burning rate of an AP/HTPB propellant and the flame behavior exhibited (taken from Jeppson et al., 1998).

The final impact on burning rate caused by the oxidizer is based on the "mode" of the propellant formulation. A "monomodal" propellant consists of one oxidizer particle size ("size" referring to the particle's diameter). Likewise, a "bimodal" propellant has oxidizer crystals of two sizes. By extension, a "multimodal" propellant contains at least two oxidizer crystal sizes, but it is more likely to refer to formulations of three or more crystal sizes. Increasing the modality of the formulation allows for additional oxidizer particles to be dispersed in the propellant in areas between larger particle sizes that would otherwise be empty (Figure 6), thus increasing the oxidizer particle packing efficiency of the composite propellant. The increased surface area contact between the AP and HTPB allows for greater reactivity and burning rate due to the increase in reaction sites.

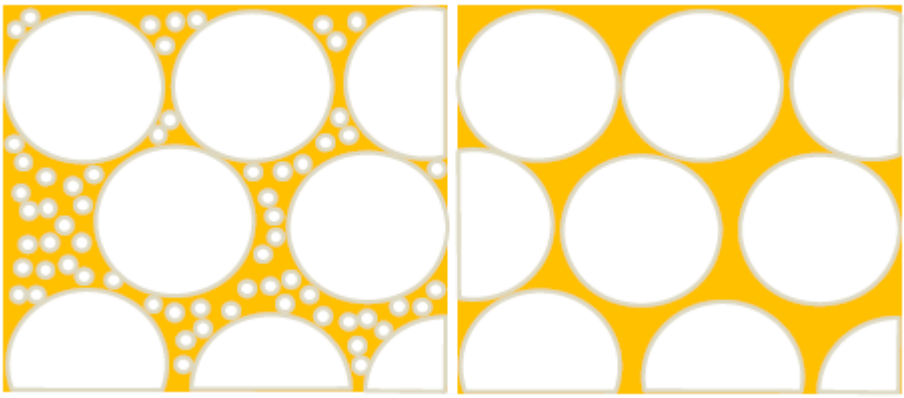

Figure 6: Illustration showing the increase in reaction sites between a bimodal composite (AP/HTPB) propellant (left) and monomodal propellant (right). The HTPB is represented by the orange region, and the white areas are the AP crystals of varying sizes. (Kreitz et al., 2011)

Tailoring the burning rate of the propellant is of interest because users of solid propellants want to control performance, reliability, and safety. Tailoring involves altering the oxidizer particle sizes, binder ingredients, or additives to change the burning rate behavior in response to pressure to meet a certain mission objective. In Figure 7, the baseline burning rate is tailored to become more and less pressure sensitive (red and blue), and this tailoring corresponds to changing the value of n in Equation 1; altering the magnitude of the burning rate while retaining the same pressure sensitivity (gray) corresponds to changing the value of a.

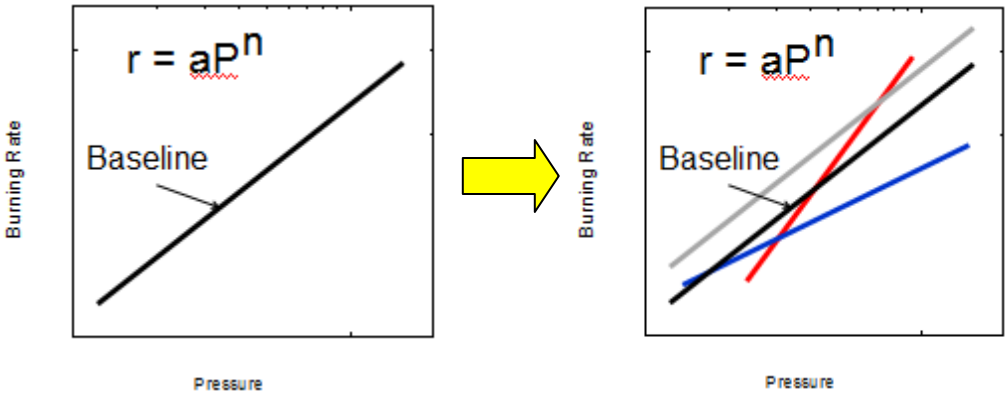

Figure 7: Illustration of tailored burning rates. The baseline burning rate can be altered to be more pressure sensitive (red), less pressure sensitive (blue), or retain the same pressure sensitivity but with increased temperature sensitivity (gray).

2.3 Role of Nanocatalysts in Solid Propellants

Nanoparticles applicable to this study are synthesized by the AMPAC (Advanced Materials Processing and Analysis Center) researchers at the University of Central Florida to a fundamental size of 5 to 7 nm in diameter. The additives are processed into a powder for mixing into various propellant formulations in the laboratory at Texas A&M University. According to Kreitz et al. (2011), the agglomerations in this powder can grow to be as large as 20 microns before being mixed into the propellant (Figure 8).

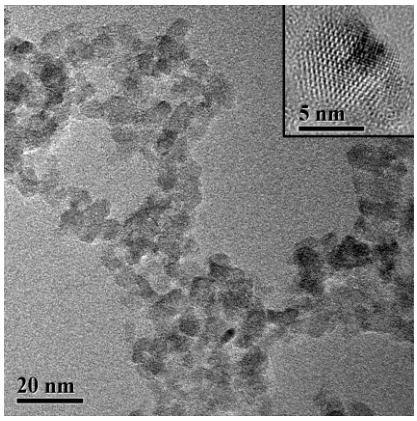

Figure 8: Image of individual TiO_2 nanoparticles at 5 nm in size (insert) and image of agglomerations 20 nm or less in size (taken from Kreitz et al., 2011).

Additive synthesis methods used in the formulations of interest to the present study are spray-dried/heat-treated, spray-dried, and premixed. A summary of the synthesis methods is provided herein; however, more detailed explanation of the specific methods and procedure can be found in Reid et al. (2011), and Kreitz et al. (2011), in their analysis on the methods of additive synthesis and the scale-up effects on burning rate.

Additive synthesis for spray-dried and spray-dried/heat-treated methods is performed by the well-known sol-gel method, which allows for detailed control of nanoparticle characteristics. Using the sol-gel method, titanium isopropoxide, $Ti\{OCH(CH_3)_2\}_4$, is hydrolyzed in an ethanol/water mixture to isolate TiO_2 via the reaction: $Ti\{OCH(CH_3)_2\}_4 + 2H_2O \rightarrow TiO_2 + 4(CH_3)_2CHOH$. The wet particles are spray dried to produce the additive in a powder form for future mixing with oxidizer and curative. The dried nanocrystals in the powder have an average size of 5 nm.

Spray drying the additive produces spherical agglomerates with a narrow size distribution (Figure 9). The smooth, spherical shape of the agglomerates provides several improvements in making the additive easier and safer to utilize in mixing processes. First, additive production is faster and more uniform because the particles do not need to be ground with a mortar and pestle. Also, spray-dried particles have excellent flow properties (helpful in extruding the wet propellant mixture through mechanical means) and create minimal dust (for safe and efficient hand-mixing and handling). The spherical agglomerates are loosely packed and break up easily when mixing into the propellant.

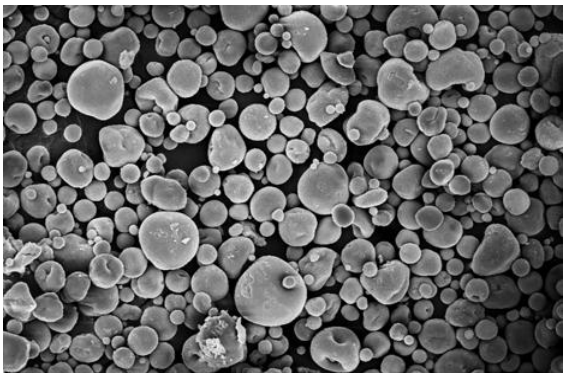

Figure 9: SEM image of non-heat-treated, spray-dried titania that shows the consistent spherical geometry of the agglomerates (Kreitz, 2010).

In the case of the spray-dried/heat-treated additive, the spray-dried powders are then heat-treated at 400°C for 3 hours to ensure full crystallization to anatase is achieved, as it is common for a trace amount of amorphous material to remain after spray-drying. During this process, the nanocrystallite size grows to 7 nm. The nanocrystallites may begin to adhere to each other during heating, or “sinter.” This

process results in agglomerations of approximately 20 nm, a loss of spherical shape, and a reduction in additive dispersion throughout the propellant (Figure 10).

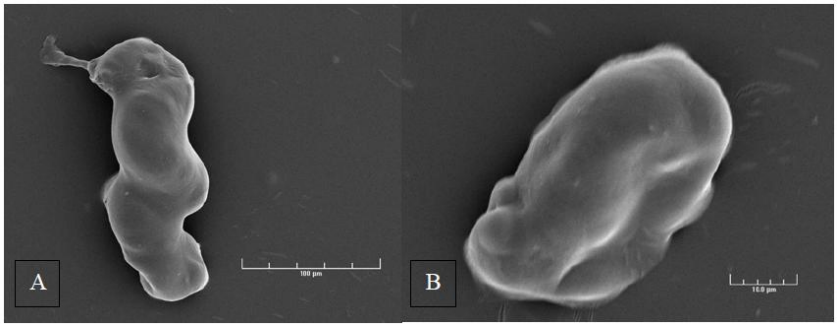

Figure 10: SEM images of spray-dried and heat-treated additive agglomerates that have sintered as a result of heat-treating. Sintered agglomerates are difficult to break up and disperse when mixing the propellant (Kreitz, 2010).

Premixed, or "ultra-fine suspension," additives are nanoparticles that are well-dispersed into the binder prior to mixing with AP and other constituents to form the propellant. The additive is produced via sol-gel reaction in suspension of a liquid solvent, then mixed with HTPB while still wet. Once the solvent is removed, the HTPB, containing ultra-fine suspensions of nanoadditive, remains behind to be added to the propellant formulation. This method completely bypasses the additive being dried into a powder and thus reduces agglomeration activity and enhances the dispersion of the additive, which retains its basic, nano-sized form, as in Fig. 11.

Shown in Figure 11, nanoparticle additives can be used to influence the burning rate over baseline composite propellant formulations by altering the reactivity of the

propellant during combustion. Stephens and Petersen (2007) identify four main reasons why nanometer-sized additive particles increase chemical reactions during combustion over those of micrometer-sized additive formulations and baseline composite propellants. The first is that there is a shorter heat transfer time for particles on the nanoscale as the smaller size and reduced mass allow the particles to increase in temperature quickly. Second, an increased surface-area-to-volume ratio allows for greater amounts of reactant molecules on the surface of the particles to be expulsed to the surroundings, placing them in more immediate contact with each other and resulting in higher reactivity. Third, nano-sized particles allow better dispersion of additives throughout the propellant, which allows for more particles to be in closer proximity to various reaction sites available during combustion (illustrated in Figure 12). The final reason is that nanoscale particles may have a completely different surface chemistry than micron-scale particles of seemingly the same composition such that they interact with and chemically influence adjacent molecules and particles in often unanticipated ways.

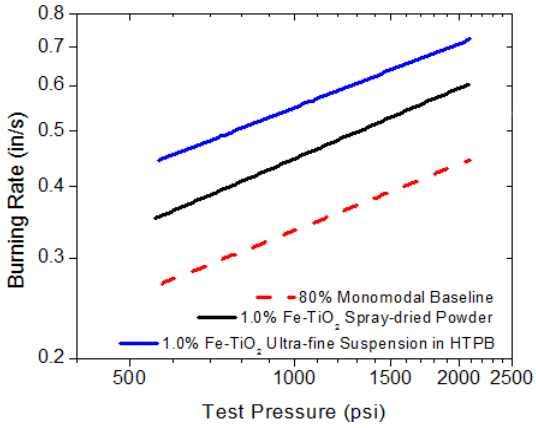

Figure 11: Experimental burning rates of monomodal (μm) 80/20% AP/HTPB with and without TiO_2 additive from author's laboratory. These additive mixtures were made using the suspension method described in the text.

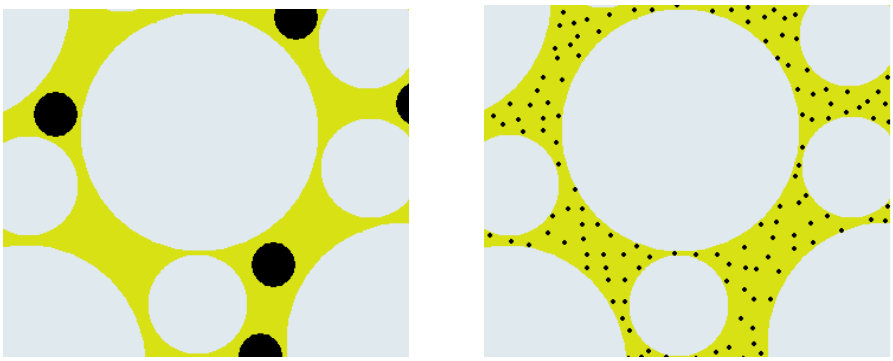

Figure 12: Illustration of a propellant cross-section showing increased dispersion of the additive particles between micrometer (left) and nanometer sizes (right). The oxidizer crystals (white), binder (yellow), and additives (black) are represented by colored regions. (Stephens and Petersen, 2007)

Research from Kreitz et al. (2011) shows that nanoparticles can significantly influence burning rates for monomodal and bimodal formulations (Figures 13 and 14). For monomodal formulations, the increase in burning rate is more pronounced than that of bimodal formulations. This finding is because of the phenomenon mentioned earlier regarding the increased surface area contact and reactivity between the AP and HTPB, resulting in higher burning rates. While the nanoadditives are well-dispersed and increase reaction rates due to catalytic activity, a bimodal formulation has many more reaction sites for the additive to influence, thus a similar mass weighting of an additive will yield smaller enhancements for multimodal formulations. This result means that the addition of nanoadditives represents a diminishing return for multimodal formulations, but an increase in the burning rate still exists. Presented earlier in Fig. 11 are burning rate results for propellants manufactured with nanoparticles that are synthesized directly in the binder, using a special premixing method. Note that the burning rate increases are even higher than those seen in Figures 13 and 14, approaching 100% over the baseline formulation.

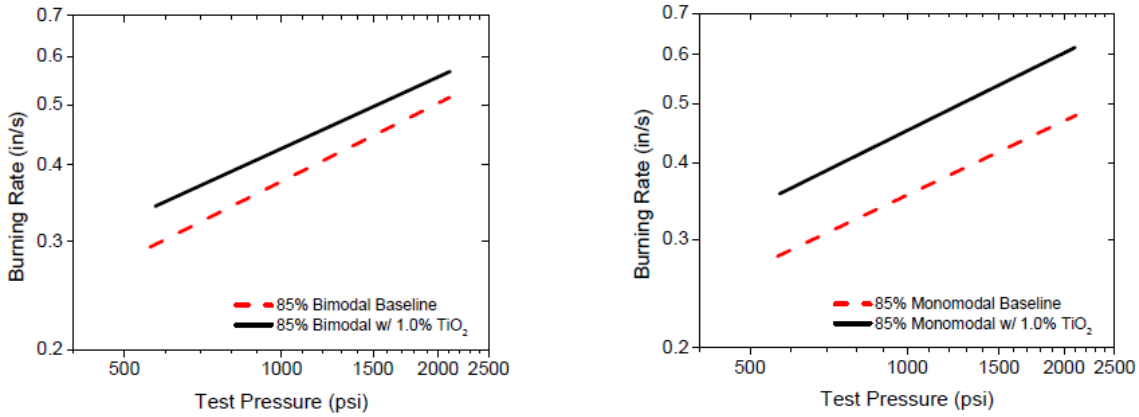

Figure 13: Experimental burning rate plots of an 85/15% AP/HTPB formulation with (solid black line) and without (red, dashed line) TiO_2 additive. Monomodal (200-µm AP crystal size) burning rate enhancements are greater than those experienced for bimodal (200- and 20-µm AP crystal sizes) formulations (Kreitz et al., 2011)

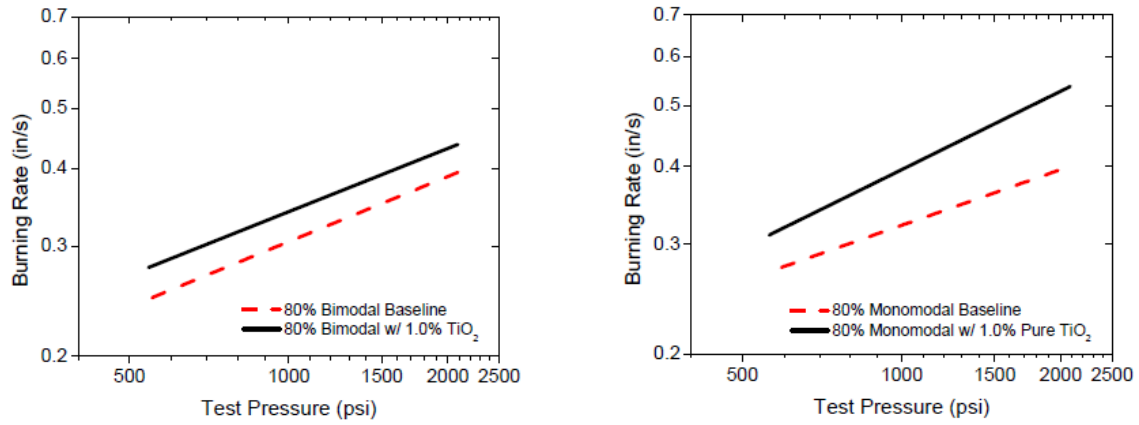

Figure 14: Experimental burning rate plots of an 80/20% AP/HTPB formulation with (solid black line) and without (red, dashed line) TiO_2 additive. Monomodal (200-µm AP crystal size) burning rate enhancements are greater than those experienced for bimodal (200- and 20-µm AP crystal sizes) formulations (Kreitz et al., 2011).

Based on Figures 11, 13 and 14, nanoparticle-based additives can significantly enhance the burning rate of composite propellants. However, the exact mechanisms underlying such behavior are not known and many theories exist. Chakravarthy et al. (1997), provide an extensive list of the supposed avenues for catalytic impacts, several of which are discussed in later sections in this thesis: accumulated additive heating the propellant surface and increasing regression via direct, thermal contact; binder melt layer behavior being influenced physically or chemically; catalysis of the binder and/or AP condensed phase; catalysis of gas phase reactions; and formation of new molecules (metal perchlorates) by the additive interaction with the AP and HTPB decomposition products. Singh et al. (2009), provided an explanation for the role of nanocatalysts in their nanoferrite research stating that during exothermic AP decomposition, nanocrystals can absorb the gaseous reactive molecules on their surface and catalyze the gas-phase reactions. Based on the variety of theorized mechanisms, a model of the composite propellant combustion process capable of predicting the burning rate results with and without catalytic additives would be extremely useful when interpreting the experimental results, ultimately leading to a better understanding of the propellant burning process in the presence of catalytic nanoparticle additives.

To the author's knowledge, there are no models that attempt to predict the burning behavior that results from the addition of catalytic nanoparticles. Beckstead (1977), briefly attempted to model catalytic effects of Fe_2O_3 additive. In that study, Beckstead developed relations to be integrated into the BDP model that predicted the burning rate influence of the additive. To calculate the burning rate of the entire

propellant, it was assumed that the burning rate was the sum of the catalytic burning rate and the burning rate of the heterogeneous propellant. The set of relations in his study assumed that the catalytic additive only affected the reactions occurring within the primary flame. Additionally, the focus of that research was micrometer-sized metal oxides whereas the current study is to model the effects of nanometer-sized metal oxides. Finally, while the relations in Beckstead's study assumed a monomodal formulation, the research herein includes multimodal formulations. Beckstead's relations nonetheless provide insight into the additive characteristics that influence the catalytic burning rate.

2.4 Basic Equations

The following sections contain an overview of some basic thermodynamic principles utilized in the model calculations. The purpose of these sections is to familiarize the reader with how the principles are incorporated and any assumptions that needed to be made to define model constraints. The model often incorporates these well-known formulations with complex representations and a quick overview is intended to help facilitate understanding and recognition of these types of calculations in the equations and literature sourced.

2.4.1 First Law of Thermodynamics

The combustion and strand burner models in this study employ the First Law of Thermodynamics to determine temperature changes between states via steady-state or

transient processes. Steady-state calculations are utilized in the combustion model to calculate the surface temperature of the ammonium perchlorate at an arbitrary state after the initial state. Steady-state calculations have the following assumptions:

1. The control volume does not move relative to the coordinate frame.
2. The state of the mass at each point in the control volume does not vary with time.
3. The state of the mass flux and the state of this mass at each discrete area of flow on the control surface do not vary with time. The rates at which heat and work cross the control surface remain constant.

The assumptions result in Equation 2, which is the basis for the energy balance calculations for the AP surface of the crystal in the combustion model. Neglecting work because none is performed by the crystal, assuming kinetic and potential energy to be negligible, and considering that the crystal only loses mass (due to decomposition), Equation 2 becomes Equation 3. Equation 3 is a simplified way of saying that the energy that the crystal receives is balanced by the energy lost to decomposition (which will result in higher burning rates for higher energy additions, q_{cv}).

$$\dot{Q}_{cv} + \sum \dot{m}_i \left(h_i + \frac{V_i^2}{2} + g z_i \right) = \sum \dot{m}_e \left(h_e + \frac{V_e^2}{2} + g z_e \right) + \dot{W}_{cv} \tag{2}$$

$$q_{cv} = h_e \tag{3}$$

The transient model, used in the strand burner model, has three assumptions according to Borgnakke and Sonntag (2007):

1. The control volume remains constant relative to the coordinate frame.
2. The state of the mass within the control volume may change with time, but at any instant of time the state is uniform throughout the entire control volume.
3. The state of the mass crossing each of the areas of flow on the control surface is constant with time, although the mass flow rates may vary with time.

The resulting expression from these assumptions is Equation 4. Considering that the strand burner is adiabatic, the heat and work terms become zero. Additionally, the vessel is assumed to be losing no mass, thus the mass exiting term also becomes zero. Potential and kinetic energy are assumed to be negligible. Equation 4 becomes Equation 5 as an initial approximation of the strand burner temperature change under adiabatic conditions (heat transfer is integrated later in the study).

$$\dot{Q}_{cv} + \sum \dot{m}_i \left(h_i + \frac{V_i^2}{2} + g z_i \right) = \frac{dE_{cv}}{dt} + \sum \dot{m}_e \left(h_e + \frac{V_e^2}{2} + g z_e \right) + \dot{W}_{cv} \tag{4}$$

$$\dot{m}_i h_i = \frac{dE_{cv}}{dt} \tag{5}$$

2.4.2 Ideal Gas Law

The classical thermodynamic ideal gas law is most accurate for monatomic gases at high temperatures and low pressures. According to Fox and McDonald (1998), and Borgnakke and Sonntag, fluids at temperatures two or more times greater than the critical temperature (150 K for Argon) can be assumed ideal gases for pressures as high as 4 or 5 times the critical pressure (760 psi for Argon). Since the strand burner gas mixture starts and remains more than twice the critical temperature of Argon throughout the test (the Argon is considered to be at room temperature initially) the ideal gas law will be applied to determine the pressure of the gas in the strand burner. This assumption is supported in research by Bates et al. (1998), which confirms that at the given pressures and temperatures, the predominantly Argon gas mixture will have a compressibility factor of unity. The thermodynamic properties of an ideal gas, specifically the pressure, can be described by the equation of state:

$$P = \frac{mRT}{V} \tag{6}$$

which relates the temperature of the gas mixture to the pressure.

2.4.3 Gas Mixture Relations

To accurately calculate the change in temperature and pressure of the strand burner gas mixture, gas mixture relations are employed to determine the minute changes

in chamber gas composition despite the fact that the overall gas mixture remains predominantly Argon by the end of the strand burning test.

The problem in the model considers the Argon, propellant products, and the overall gas mixture of the two to be ideal gases. Thus the thermodynamic problem involves the mixture of two pure substances (Argon and "propellant gas" – although the model has the modularity to perform calculations based on individual propellant species). According to Borgnakke and Sonntag, the mass fraction is calculated from Equation 7, the mole fraction from Equation 8, and the molecular mass of the Argon-propellant gas mixture is determined from Equation 9.

$$x_i = \frac{m_i}{m_{tot}} = \frac{n_i M_i}{\sum n_j M_j} = \frac{n_i M_i / n_{tot}}{n_j M_j / n_{tot}} = \frac{y_i M_i}{\sum y_j M_j} \tag{7}$$

$$y_i = \frac{n_i}{n_{tot}} = \frac{m_i M_i}{\sum m_j M_j} = \frac{m_i / M_i m_{tot}}{\sum m_j / M_j m_{tot}} = \frac{x_i / M_i}{\sum x_j / M_j} \tag{8}$$

$$M_{mix} = \frac{m_{tot}}{n_{tot}} = \frac{\sum n_i M_i}{n_{tot}} = \frac{n_i M_i / n_{tot}}{n_j M_j / n_{tot}} = \sum y_i M_i \tag{9}$$

A mean specific heat value, C_p, will not be used due to mixing between the Argon and propellant combustion products causing changes in mixture specific heat, $C_{p,mix}$, that impact the calculated temperature. The specific heat of each component of the mixture is calculated based on its mass fraction (at a given point of the test time) and then those values are added together to obtain $C_{p,mix}$ (Equation 10). The specific heat for constant volume of the mixture, $C_{v,mix}$, is then calculated via Equation 11. In this fashion,

the C_p and C_v of the mixture are allowed to change with time, as they are calculated with changing mass faction as more propellant gas "enters" the control volume.

$$C_{p,mix} = C_{p,Ar} x_{Ar} + C_{p,propgases} x_{propgases} \tag{10}$$

$$C_{v,mix} = C_{p,mix} - \frac{R}{M_{mix}} \tag{11}$$

2.4.4 Dalton's Model

For the model in this study, the interactions between the molecules of the different components of the gas mixture at high pressure are ignored. In using Dalton's model of gas mixtures, two assumptions must be made:

1. The properties of each component of the mixture are considered as though each component exists separately and independently at the same temperature and volume of the mixture.
2. Both the gas mixture and the individual components behave like ideal gases.

Based on these assumptions, the ideal gas mixture can be analyzed on a mass basis or a mole basis. Equations 12–14 are used to determine the partial pressures, or contribution of each gas mixture component (Argon and collective propellant gases) to the overall pressure of the system.

$$n = n_1 + n_2 \tag{12}$$

$$P = P_1 + P_2 \tag{13}$$

$$P_i = y_i P \tag{14}$$

2.4.5 Heat Transfer Overview

This study will be concerned with the long-term effects of heat transfer on the pressurized gas temperature during and post-propellant burn. To study the heat transfer effects between the gas mixture and the strand burner wall, research from Frazier et al. (2011), is employed to model the heat transfer mechanisms. While Frazier utilized a shock-tube test region, post reflected shock, the geometry of the shock tube is similar to that of the strand burner in that both are cylindrical and, thus, is suitable for 1-D relations pertaining to the conduction heat transfer mechanism between the hot gas mixture and the cold walls of the strand burner (Figure 15). The research in that study indicated that heat transfer effects are dependent on the values of *k*, thermal conductivity, and the gas constant *R*, and includes effects of the geometry of the test apparatus. Heat transfer will be modeled with conduction and convection mechanisms. Radiation is ignored as initial calculations determined that radiation was responsible for an approximately 10^{-5} K temperature change.

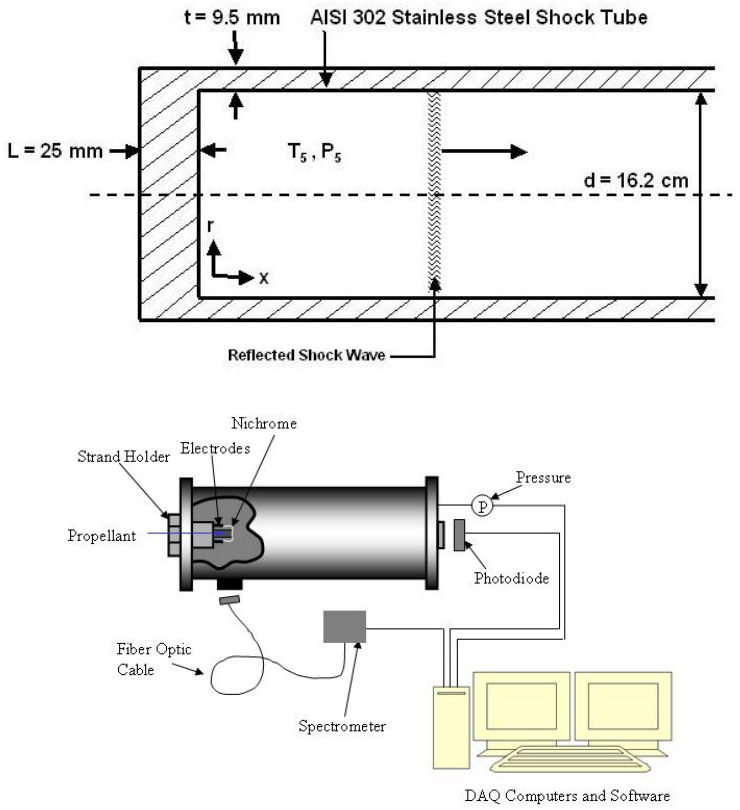

Figure 15: An illustration of the shock tube geometry used in Frazier et al. (2011) (upper), and a schematic of the strand burner apparatus and supporting equipment (lower). The two apparatuses share a similar geometry allowing the relations from previous research to be utilized.

2.4.6 Conduction Heat Transfer

The determination of heat transfer effects is both a heat conduction concern (Figure 16) and an ambient freestream convection one (convection being the major contributor). For conduction in isotropic, homogeneous solids, an analytic relationship

between heat flow and the temperature gradient can be expressed. This basic law is known as “Fourier’s Law” and is given as:

$$q(x,y,z,t) = -k\nabla T(x,y,z,t) \tag{15}$$

per Ozisik (1993) and DeWitt and Incropera (2001). The heat flux vector, *q*, is the heat flow per unit of time per unit of area of the isothermal surface moving in the direction of decreasing temperature (hence the negative temperature gradient). The components of the heat flux vector are described as:

$$q_x = -k\frac{\partial T}{\partial x}, \qquad q_y = -k\frac{\partial T}{\partial y}, \qquad q_z = -k\frac{\partial T}{\partial z} \tag{16a), (16b), (16c)}$$

Thus, the heat flow rate is directly proportional to the thermal conductivity, *k*, of the material. This makes the thermal conductivity an important parameter in the analysis of heat conduction, as it controls the heat flow in the conducting material.

Neglecting heat generation, the differential equation of heat conduction is derived as:

$$-\nabla \cdot q(x,y,z,t) = \rho C_p \frac{\partial T(x,y,z,t)}{\partial t} \tag{17}$$

And, assuming constant thermal conductivity, simplifies to:

$$\nabla^2 T(x,y,z,t) = \frac{1}{\alpha}\frac{\partial T(x,y,z,t)}{\partial t} \tag{18}$$

where α is the thermal diffusivity and is expressed as:

$$\alpha = \frac{k}{\rho C_p}. \tag{19}$$

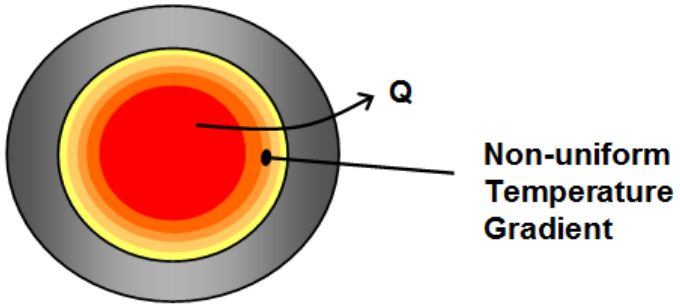

Figure 16: A radial illustration of the conduction heat transfer problem for the strand burner.

2.4.7 Convection Heat Transfer

The dominant heat transfer mechanism is free convection due to the constant rise and fall of hot and cold gases in the strand burner. The flow speed of the gas mixture as a result of the ejection of hot propellant gases is negligible as initial calculations

determined that movement in the vessel was approximately 10^{-5} m/s. Due to the slow flow in the vessel, free convection is used instead of forced convection.

To obtain the change in temperature as a result of the change in heat energy due to natural motion, a predictive equation for convective heat flux, also known as Newton's Law of Cooling, is utilized. From Burmeister (1993) and DeWitt and Incropera (2001), Newton's Law of Cooling is represented by Equation 20. The heat transfer coefficient obtained in this study is assumed to be constant and does not change over the test time. Experimentally, this is not exactly the case, as the coefficient is sensitive to flow conditions in the ambient fluid, but it is a sufficient approximation for the present study. Boundary layer thickness at the wall should decrease as fluid flows by more rapidly (Burmeister). If a constant temperature difference between wall and fluid is assumed then the heat flux should increase as the boundary layer thickness decreases. According to Equation 20, the heat transfer coefficient should increase to accommodate this realistically. The model assumes that natural fluid flow within the vessel is constant such that the boundary layer effects at the wall on heat transfer coefficient are negligible. Figure 17 provides an illustration of the convection problem.

$$q = \frac{Q}{A} = h\left(T_{wall} - T_{fluid}\right) \tag{20}$$

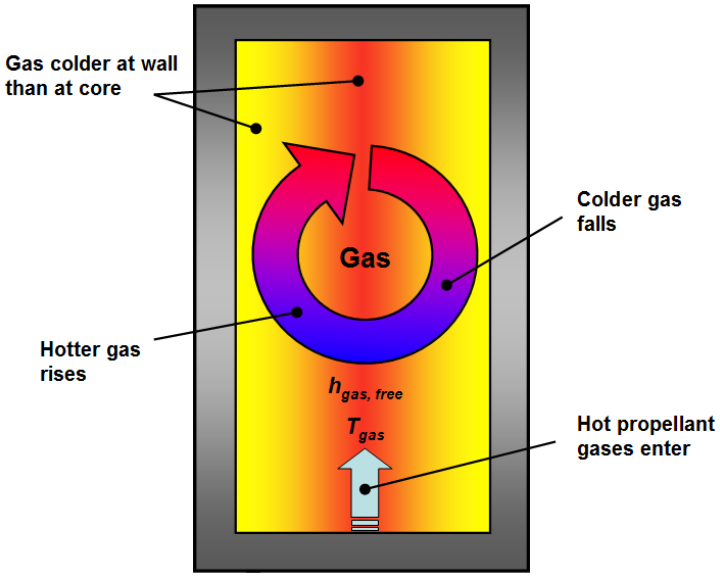

Figure 17: Illustration of free convection in the strand burner. Hot gas rises in the vessel while cooler gas falls. Along with the hot propellant gases this causes a rise and fall effect in the vessel.

2.4.8 Thermal Conductivity

Thermal conductivity varies with temperature. The highest values are given to pure metals, while the lowest correspond with gases and vapors. For most pure metals, thermal conductivity decreases with temperature, however, for gases, it increases with increasing temperature.

Since strand burning tests may not operate at standard temperature and pressure throughout the entire test time, a mean value for thermodynamic inputs cannot be used without noticeable losses in accuracy, even for basic models. The thermal conductivity of the gas mixture (predominantly Argon herein) at various temperatures is calculated from Sutherland's formula:

$$\frac{k}{k_o} = \left(\frac{T}{T_o}\right)^{\frac{3}{2}} \left(\frac{T_o + S}{T + S}\right). \tag{21}$$

Thermal properties and constants at reference values for T_o, k_o and S are obtained from viscous flow experiments in White (1991) and are summarized in Table 1.

Table 1: Thermal conductivity and constants of Argon at 273K.

Gas	T_o (K)	k_o (W/m-K)	S (K)
Ar	273	0.0163	170

2.5 Propellant Evaluation Program (ProPEP)

ProPEP is a thermo-chemical program that evaluates the theoretical performance of solid and liquid propellants, allowing the user to see the equilibrium conditions of the combustion process. Through knowledge of the equilibrium conditions, the user can alter the ratios of the propellant ingredients and combustion conditions to achieve desired equilibrium values. It is from ProPEP that the model is able to utilize speciation, species concentration, gas mixture molecular weight, and adiabatic flame temperature as inputs.

ProPEP determines chemical equilibrium by guessing at the equilibrium composition iteratively. The basis for this method of finding chemical equilibrium is a

combination of Villars' method and a method obtained from H. N. Browne. In this setup, Villars' method of a linearization and Taylor series expansions (Villars, 1959) are employed with improved computational methods to find the chemical composition, and Browne's method is used to optimize the baseline (the predetermined subset of molecular species formed by chemicals present in the reaction, according to Browne et al., 1960) and speed up convergence. The significance of Browne's method is that it introduces the concept of the "optimized" basis, in which the system components are present in the greatest possible molar amounts (Cruise, 1979).

Enthalpy balance iteration technique is used to find the final temperature of the products and thereby the remaining thermodynamic properties of the system at equilibrium. Newton's Method for interpolation and a Bisection Method (referred to in Cruise as "Interval-Halving") are employed to determine the adiabatic flame temperature via iterative processes that mimic the method for determining the adiabatic flame temperature (T_{AF}) via comparison of heats of the reactants to the heats of the products based on guessed temperatures reminiscent of combustion science problem solving (Annamalai and Puri, 2007 and Glassman, 1996). Since the heats are a function of temperature, the temperature that provides total product enthalpy equal to the total reactant enthalpy is the adiabatic flame temperature (Equation 22).

$$\sum H_{\mathrm{Re}actants@T=T_{initial}} = \sum H_{\mathrm{Pr}oducts@T=T_{AF}} \tag{22}$$

To calculate the necessary chamber conditions, ProPEP makes the following assumptions regarding the combustion process (Cruise):

1. Kinetics occur fast enough such that equilibrium is reached within the chamber prior to the combustion products leaving the chamber and entering the nozzle of the rocket motor (nozzle consideration is for exhaust flow calculations not applicable to this study).
2. No heat is transferred beyond system boundaries. The enthalpy of the reactants is conserved in the enthalpy of the products (Adiabatic combustion process).
3. All gas species in the products obey the Ideal Gas Law and also obey Dalton's law for partial pressure calculations.

Additional considerations include: constant pressure throughout the combustion process in the chamber and that the gram weights entered are correct.

To test the accuracy of ProPEP, two simple runs were conducted using 77% AP / 23% HTPB and 84% AP / 16% HTPB at nearly 1 psi with the adiabatic flame temperature from each being of particular interest. These constituents, their amounts, and the pressure were chosen to be in line with flame temperature analysis conducted using (1) a kinetics model for premixed combustion of fine AP/HTPB composite propellant and (2) a model used to determine flame structure and kinetics based on solving differential equations. The first model, which will be called the "Jeppson Model," is specifically geared toward premixed combustion of monomodal, fine

AP/HTPB propellants and takes into consideration combustion in three phases: solid phase, condensed phase region of mixed liquid and gas, and a premixed gas phase flame (Jeppson et al., 1998). The second model, which will be called the "Korobeinichev Model," solves a set of differential equations which describe flow of a reacting multi-component gas by taking thermal conductivity and diffusion into account, and also the kinetic mechanism containing 58 elementary stages and 35 components obtained from previous research between the authors that studied kinetics in AP and HTPB composites (Korobeinichev et al., 1992).

Table 2: The flame temperature results from the Korobeinichev, Jeppson, and ProPEP models/programs at approximately 1 psi. ProPEP flame temperatures are higher than predicted for the other two models. Korobeinichev and Jeppson flame temperature values are approximate.

Model	%AP (by weight)	Flame Temperature (K)
Korobeinichev	84	2000
	77	1850
Jeppson	84	2200
	77	1900
ProPEP	84	2429
	77	1972

As Table 2 shows, the data generated by the PEP model agrees with the data produced by two other models, but there are some potential discrepancies that should be clarified. The ProPEP data shows the flame temperature being hotter than the other two models. This is most likely because the ProPEP runs were made using the R45M, or military-grade variant, of HTPB, which would result in a slightly higher temperature due

to the increased amount of carbon and hydrogen in the chemical composition. Also, the flame temperatures in Table 2 do not match up with the plot in Figure 4 because of the extremely low pressure of the analysis (1 psi). Small changes in pressure for a propellant formulation tend to have little impact on the adiabatic flame temperature however extreme pressure regimes can significantly enhance or reduce the flame temperature approximated by the ProPEP program due to pressure influencing kinetics. At more common pressures seen in our laboratory, for example, 1000 psi, ProPEP calculates flame temperatures of 2731 K (for 84% AP) and 1998 K (for 77% AP). These values are in agreement with Figure 4. This is a rudimentary check, but it confirms that ProPEP is a sufficiently accurate application for the estimation of thermodynamics properties at equilibrium.

2.6 Chemical Equilibrium Analysis (CEA) Code ThermoBuild – Enthalpy & Specific Heat

ProPEP provides the total enthalpy, however what is needed is the sensible enthalpy corresponding to the energy being added to the system due to the difference in adiabatic flame temperature and the reference temperature of the combustion products and gas mixture. Additionally, for purposes of analysis and functionality, a species-specific evaluation of enthalpy and specific heat properties is preferred. To determine this evaluation, the ThermoBuild portion of a chemical equilibrium analysis (CEA) code is utilized to provide tables of thermodynamic properties for a user-supplied temperature schedule for each species. Using Equations 23–26, gas mixture approximations of the

enthalpy and specific heat can be found at all temperatures on a time-scale within the strand burner model. Currently, NASA Glenn Research Center CEA code is implemented into model predictions via an online tool located at: http://www.grc.nasa.gov/WWW/CEAWeb/ceaThermoBuild.htm. However, the equations utilized by this online tool are capable of being built into the base model structure if a thermochemical database of species is developed.

The specific heat value for each gas species of the burned propellant is found using a basic polynomial fit:

$$\frac{C_p^{\circ}(T)}{R} = a_1 T^{-2} + a_2 T^{-1} + a_3 + a_4 T + a_5 T^2 + a_6 T^3 + a_7 T^4 \tag{23}$$

where R is the universal gas constant and T is the temperature of the product species. Values for the coefficients, a_i, in Equation 23 are obtained from McBride et al. (2001). To determine an overall gas mixture C_p using Equation 10, the specific heat of Argon must be known. According to Kee et al. (1990), Argon is an exception such that the polynomial reduces to a constant, a_1, which has a value of 2.50 for all temperatures up to 5000 K (because Argon is a monatomic gas). The specific heat for Argon is effectively treated as:

$$\frac{C_p}{R} = \frac{\gamma}{\gamma - 1}, \tag{24}$$

with a specific heat ratio of 1.67. Enthalpy is obtained by integrating $C_p°(T)$ and $C_p°(T)/T$ with respect to T and provides Equations 25 and 26.

$$\frac{H^\circ(T)}{RT} = -a_1 T^{-2} + a_2 \frac{\ln T}{T} + a_3 + a_4 \frac{T}{2} + a_5 \frac{T^2}{3} + a_6 \frac{T^3}{4} + a_7 \frac{T^4}{5} + \frac{b_1}{T} \tag{25}$$

$$H^\circ(T) = \Delta_f H^\circ(298.15) + [H^\circ(T) - H^\circ(298.15)] \tag{26}$$

Where the term $[H°(T) – H°(298.15)]$ is the sensible enthalpy needed to be input into the model to assess how much energy the overall gas mixture is gaining due to the high temperature of the propellant combustion products.

According to McBride et al. (2002), most of the values of the coefficients used in Equations 23 and 25 were determined by a Least-Squares Fit. For gases, the temperature ranges for these fits are split into three fixed intervals: 200 to 1000 K (298.15 to 1000 K for ions), 1000 to 6000 K, and for some simple molecules, 6000 to 20,000 K. For condensed species, the temperature ranges are variable, with each phase having a set of coefficients. A list of the constraints utilized by the ThermoBuild to obtain the fits can be found in McBride et al.

3. MODELING METHOD

The propellant combustion model is based on First Law of Thermodynamics principles, chemistry, and statistics and is utilized to determine a steady-state burning rate. The present research on the propellant combustion model has two primary objectives:

1. Support parametric studies on propellant performance in response to pressure
2. Lend insight into trends seen in the experiments by providing a physical rationale for nanoadditive influence.

The following sections will review the original, well-known models from which the model described herein is based upon. This section will also specify how the model captures the propellant combustion process and the strand burner experiment; and how the model uses equations to predict a burning rate and pressure trace.

3.1 Beckstead-Derr-Price (BDP) Model

The combustion model is based on the famous Beckstead-Derr-Price (BDP) model, which is a three-flame, steady-state, non-interacting structure in an adiabatic system (Beckstead et al., 1970). Each three-tiered flame structure surrounds individual oxidizer crystals, which are themselves surrounded by binder (Figure 18).

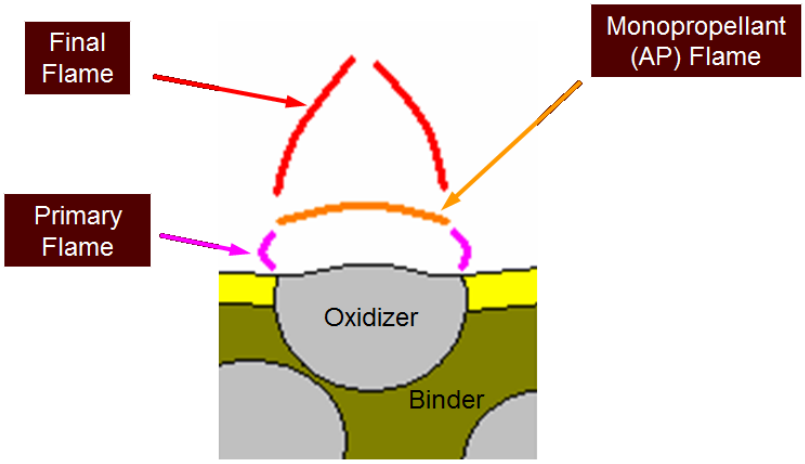

Figure 18: Simple illustration of the BDP model flame structure.

Beckstead et al., Cai et al. (2008), and several others refer to the BDP model as a diffusion flame sheet approximation of the propellant combustion problem. According to Williams (2010), this approximation means that the flames are viewed as sheets of finite thickness in which there is a fuel stream on one side, produced by finite-rate pyrolysis as the fuel is heated, and an oxidizer stream on the other. The flame sheet in this explanation is illustrated by the purple flame in Figure 18. Initially there are no oxidizer species in the fuel stream and no fuel species in the oxidizer stream. A certain amount of oxidizer flows towards, and perhaps penetrates, the flame sheet, but mostly it is the fuel species that are diffusing into the oxidizer stream due to convective effects. The transport of oxidizer and fuel species relates to parameters discussed later in this study that describe the fraction of oxidizer that participates in the diffusion flame.

The BDP model was an ideal starting point for the present combustion model as it is focused on modeling the combustion of composite propellants similar to those used

in the author's baseline test burns. Further details not covered in this thesis on the core model can be found in the original references. Various updates to the original 1970 BDP model have appeared in the literature through the years, and these improvements were incorporated (when appropriate) into the present model. These updates are summarized as follows.

3.2 Cohen-Strand Model

Multi-modal capabilities were added to the core BDP model via the Cohen-Strand model, which is also based on the BDP flame architecture but incorporates improved flame height calculations and separate oxidizer and fuel surface temperature calculations to achieve improved surface temperatures (Cohen and Strand, 1982). According to Cohen and Strand, the Final Flame parameters were removed from the energy calculations of the model as the Final Flame at the time of model development negligibly contributed to the overall surface temperature of the oxidizer crystal. This modification is a departure from the BDP model and was most likely facilitated by the improved energy calculations provided by Cohen and Strand as the calculations most likely reduced the impact of the Final Flame on the oxidizer surface temperature.

Additionally, the model employs pseudo-propellant methodology seen in the Petite-Ensemble Model in which every oxidizer particle size-type and apportioned binder behave like an individual propellant, and the burning rate for the entire propellant is the aggregate of the individual, or "pseudo," propellants (Cohen and Strand; Condon et al., 1977). The Price-Derr-Boggs model of AP self-deflagration is employed to allow

for monopropellant burning from their AP model specifying surface temperature from thermochemistry and iterating on the burning rate (Price et al., 1979). Their approach has been adapted to fit within the Cohen-Strand model framework.

3.3 Further Improvements and Modifications

Enhanced oxidizer, fuel, and flame energy release calculations were adapted from Shusser et al. (2002), to allow for more-accurate energy surface temperatures rather than relying on constants. Parameters for the model originate from previous work and across a variety of models (Beckstead et al., 1970; Cohen and Strand; Cai et al., 2008; Shusser et al., 2002; and Rasmussen and Frederick, 2002) which are based on the BDP flame architecture and characteristics.

3.4 Model Simulation of the Propellant Combustion Process

The inner-workings of the model and the corresponding physical processes that occur during combustion are complex systems that, even on a broad level, can appear disjointed and confusing. This section explains some of the model physics and mathematics and relate the model processes to the events that occur during propellant combustion. Figure 19 shows an overall picture of the system being modeled and the complexity and should be used as a reference in the following sections describing various physical processes.

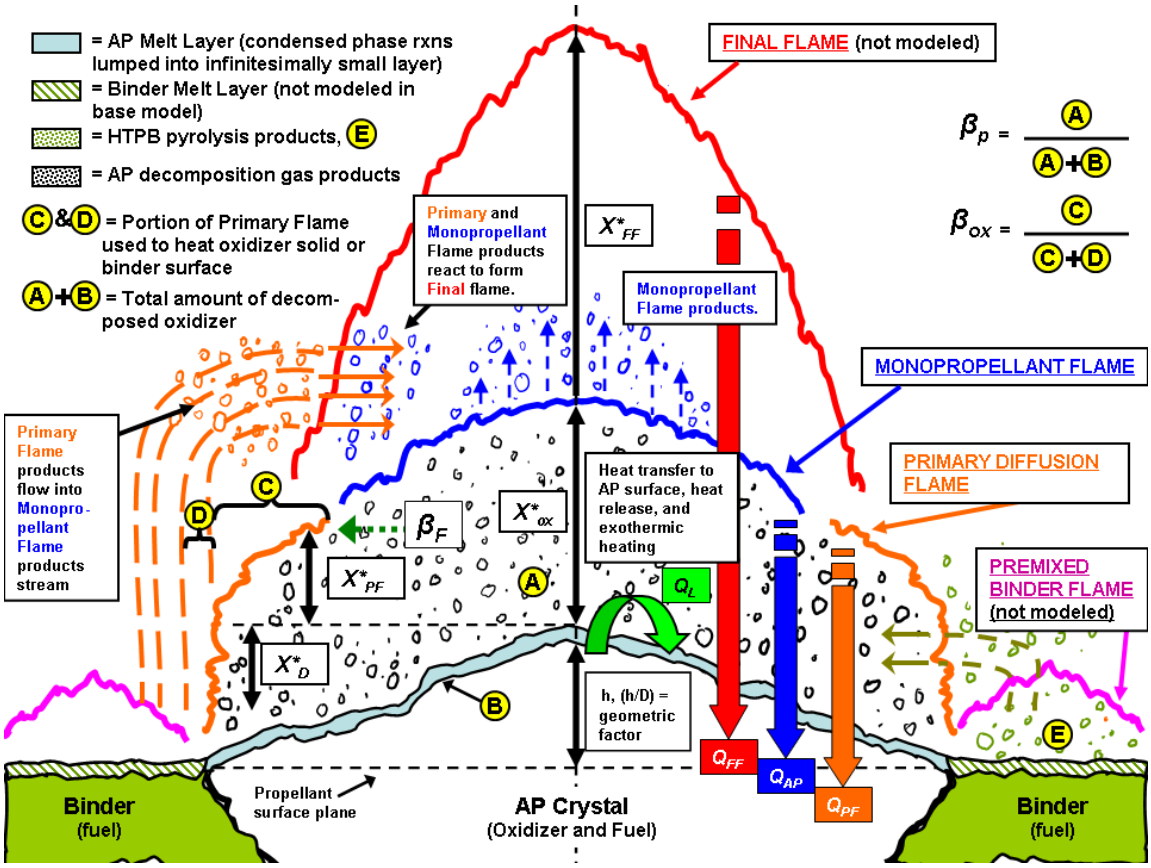

Figure 19: Overall picture of the model structure, including select parameters, and interaction during the self-sustaining process. The overall model is complex and nearly all processes impact several others.

3.5 Surface and Sub-Surface Processes

AP and HTPB are heated, kick-starting two processes: AP decomposition and HTPB pyrolysis. Models (Cai and Yang, Cohen and Strand, Beckstead et al., 1970) and analysis generally view the HTPB as pyrolysizing from the solid phase to gas products, however, other literature (Chakravarthy) indicates that a binder melt layer forms prior to pyrolysis. The model described in this thesis also assumes HTPB pyrolysis and neglects

melt layer dynamics. The model implements HTPB pyrolysis kinetics via an Arrhenius equation (Equation 27), a simplified method for capturing mass flux rate that is applied globally throughout the model for other kinetics activities as well.

$$m_{binder} = A_{binder} \exp\left(\frac{-E_{binder}}{RT_{binder}}\right) \tag{27}$$

According to Singh et al., AP (NH_4ClO_4), decomposes under low and high temperatures into $NH_4 + ClO_4$ in a gas phase. Simultaneously, another series of reactions form $NH_3 + HClO_4$ from the $NH_4 + ClO_4$ reaction. A condensed phase (melt layer) is also formed as the AP crystal experiences melting at ~473K from its crystalline state into an amorphous state that is thought to contain gas bubbles of AP decomposition products (Jeppson). According to Jung and Yoh (2010) the melt layer will form, grow, and propagate uniformly over the entire burn time according to $\exp(1/T_{oxidizer})$, where $T_{oxidizer}$ is the surface temperature of the AP crystal. Additionally, the melt layer will be thinned at increased test pressures. However, it should be noted that the model in this study is steady-state, and melt layer thickness and growth is not captured. Gas phase AP decomposition products result from continued heating of the condensed phase which gasifies or, at higher temperatures, from sublimation of the AP crystal into the gas phase, both of which result in the aforementioned decomposition mechanisms. Research from Beckstead (2007), presents several other mechanisms in which the condensed phase does

not gasify into $NH_3 + HClO_4$, but follows several other reactions mechanisms instead: $H_2O + O_2 + HCl + HNO$; $2H_2O + Cl + NO_2$; $ClO_3 + NH_3 + OH$.

In terms of the model, this activity, on the surface and in the condensed phase, is captured using Arrhenius equations (Equations 28 and 29) with empirically determined kinetics constants for the activation energy and reaction rate instead of by using a series of detailed kinetics steps to model the activity that would determine the mass flux of the AP. Equations 28 and 29 assume that the condensed phase, *s*, and surface reactions, *ox*, occur at the same temperature, $T_{oxidizer}$.

$$m_{ox} = A_{ox} \exp\left(\frac{-E_{ox}}{RT_{oxidizer}}\right) \tag{28}$$

$$m_{s} = A_{s} \exp\left(\frac{-E_{s}}{RT_{oxidizer}}\right) \tag{29}$$

3.6 Monopropellant Flame Processes

Once in the gas phase, the AP further decomposes in two steps and becomes more reactive. After the second decomposition, the species become so reactive that they may combust forming the Monopropellant Flame. The products of the first step are N_2O, O_2, Cl_2, H_2O, and trace amounts of NO. The second gaseous decomposition produces NO, O_2, Cl_2, and H_2O. At this point, these products result in the formation of the Monopropellant Flame as they react. Reaction kinetics in the Monopropellant Flame are also captured in a simple Arrhenius expression (Equation 30) to determine mass flux.

$$m_{AP} = A_{AP} \exp\left(\frac{-E_{AP}}{RT_{AP}}\right) \tag{30}$$

Characteristically, the Monopropellant Flame is flat compared to the Primary and Final Flames due to the premixed flame property of a localized flame front. Reaction rates are fast in the Monopropellant Flame and are not impeded by diffusion since the gaseous AP decomposition products are reactive components that are already in close proximity.

The flame standoff distance of the Monopropellant Flame is governed largely by pressure and is calculated by the model in Equation 31 and then expressed as a dimensionless parameter in Equation 32. The dimensionless parameter is used to weight the energy transference from the flame to the oxidizer surface. In Equation 31, the dependence of the standoff distance on pressure can be seen as higher pressures will result in a smaller distance. High pressures bring the flame closer to the propellant surface, as the increase in pressure influences reaction rates, and cause the propellant to burn more like an AP monopropellant and reduce diffusion by the HTPB pyrolysis products into the now quickly reacting oxidizer stream. Lower pressures increase flame standoff distances and allow HTPB pyrolysis products to diffuse into the oxidizer stream and react, thus forming the Primary Flame. In Equation 31, the reaction rate of the Monopropellant Flame, A_{AP}, has pressure dependent units of mass flux, $\frac{g}{cm^3 \cdot s \cdot atm^2}$; unlike A_s, A_{binder}, and A_{ox}, which have units in $\frac{g}{cm^2 \cdot s}$.

$$X^*_{ox} = \frac{m_{ox}}{A_{AP} \exp\left(\frac{-E_{AP}}{RT_{AP}}\right) P^2} \tag{31}$$

$$\zeta_{ox} = \frac{C_{p,oxidizergas}}{\lambda_{oxidizergas}} m_{ox} X^*_{ox} \tag{32}$$

3.7 Primary Flame Processes

At the interface between the AP crystal and HTPB, HTPB pyrolysis products diffuse into the region of gaseous AP decomposition products and react to form the Primary Flame (or Primary Diffusion Flame). The reaction in this flame is complex, considering all the possible reactions in a kinetics mechanism (for example, the kinetics model by Jeppson uses 72 reaction mechanisms, Appendix A). The level of complexity prevents the Primary Flame from utilizing the Arrhenius expression in the simplified fashion applied to the Monopropellant Flame; it would be difficult to apply an averaged A_{PF} or E_{PF} in the form of Equation 30 for the Primary Flame that accommodates most of the likely reactions. To reduce the complexity, in line with the rest of the global kinetics being used, a reaction rate, k_{PF}, is set at an empirically found constant with a reaction order, δ_{PF}, that is also an empirical value (Beckstead, 1970). The reaction order influences the reaction rate's sensitivity to pressure via the units of the reaction rate: $\frac{g}{cm^3 \cdot s \cdot atm^{\delta_{PF}}}$. Primary Flame reactions are mixing and kinetics dependent. However,

the AP decomposition gas mixes with the HTPB pyrolysis products via diffusion, so the flame speed is limited by mixing rates, resulting in a longer flame front.

In the model, the amount of oxidizer gas that participates in the Primary Flame reaction (instead of reacting in the Monopropellant Flame) is defined as a percentage, β_F. Equation 33 was provided by Cohen (1980), and shows β_F as a function of flame standoff distances and the average flame height factor above the AP crystal, A_{fh}. However, when using Equation 33, steeper burning rate slopes resulted when plotted versus pressure (Figure 20). Condon et al. in their paper provided another equation for β_F without the average flame height factor, A_{fh}, which is the ratio of the diffusion distance above the surface to the maximum heat transfer distance of the diffusion flame above the surface (a visual approximation would be X^*_D / X^*_{PF} in Figure 19). Utilizing this version of the equation provided the expected pressure sensitivity for the burning rate. However, to maintain more realistic β_F values, A_{fh} was re-inserted into the β_F equation and any β_F term in the First Law equation (Equation 38) used to determine the calculated surface temperature of the oxidizer was divided by A_{fh} to improve the pressure sensitivity and avoid post-processing of the β_F parameter.

$$\beta_F = \frac{X^*_{ox} - X^*_{PF}}{X^*_{PDF}} A_{fh} \tag{33}$$

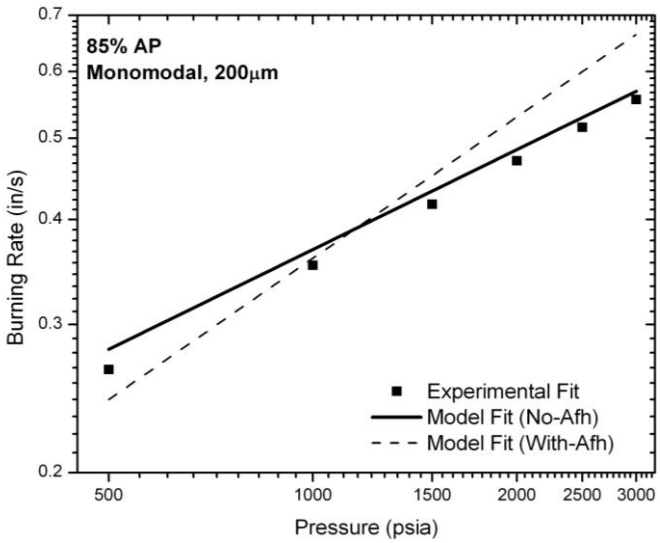

Figure 20: Plot of 85/15 AP/HTPB utilizing A_{fh} in the β_F calculation and with A_{fh} removed. It can be seen that the non-A_{fh} model prediction achieves a similar slope as the experimental results, whereas the A_{fh}-implemented prediction is more pressure sensitive.

When A_{fh} is removed, the proper pressure sensitivity is achieved. The correlations for the experimental data and the model predictions with A_{fh} removed were very similar, $0.0204P^{0.41}$ and $0.0241P^{0.39}$, respectively, compared to that of the A_{fh}-integrated model prediction which was $0.0076P^{0.56}$.

It is important to understand why the removal of A_{fh} provides the expected burning rate trend. For A_{fh}, the diffusion distance of the HTPB products is considered to be much smaller than the effective heat transfer distance of the Primary Flame, leading to A_{fh} of 0.3 used in the model. It should be noted that changing the value of A_{fh} did not produce a favorable slope of the burning rate response to pressure for all propellant formulations. In Equation 33, A_{fh} causes β_F to decrease (as $A_{fh} < 1$) and the contribution

of the energy release of the Monopropellant Flame to the AP surface temperature to increase, as seen in Equation 38. Conversely, removing A_{fh} from Equation 33 increases β_F and decreases the surface temperature contribution of the Monopropellant Flame. The contribution of the Primary Flame to the AP surface temperature is opposite that of the Monopropellant Flame with increasing or decreasing β_F. Increasing β_F reduces the amount of AP gas available to react in the Monopropellant Flame because β_F is the percentage of the AP gas that participates in the Primary Flame reactions. If the AP reactants are engaged in the Primary Flame instead, a smaller portion of the energy from these reactants is used to heat the AP crystal as some of the energy will heat the binder; the Monopropellant Flame more directly transfers its energy to the crystal instead of the binder because of its position situated over the crystal. This portion of energy transferred to the AP crystal from the Primary and Monopropellant Flames is governed by β_{ox} (Equation 37). Since removing A_{fh} increases β_F, then removing A_{fh} means less energy from the Monopropellant Flame heats the oxidizer, but more energy from the Primary Flame heats the oxidizer due to the increase in oxidizer participation in the reactions. Thus, removing A_{fh} brings the AP surface temperature down at higher pressures where Monopropellant Flame heating becomes more significant because flame closeness to the propellant surface is greatly enhanced by the square of the pressure (Equation 31). The reduction in Monopropellant Flame contribution to AP surface temperature reduces the burning rate at very high pressures. The increase in Primary Flame contribution to AP surface temperature increases the burning rate at lower pressures, where Primary Flame interactions dominate the burning rate. Thus, removing A_{fh} brings high pressure burning

rates down and brings low pressure burning rates up. While the energy release of the Primary Flame is greater than the Monopropellant Flame, a smaller portion of the Primary Flame heat is transferred to the crystal than the Monopropellant Flame due to the terms β_F/A_{fh} and $(1 - \beta_F/A_{fh})$ in Equation 38. The relationship between β_F and pressure can be seen in Figure 21. As the pressure increases, β_F decreases, which causes the Monopropellant Flame to have an increased contribution to the oxidizer surface temperature (in Equation 38) and the Primary Flame to have a reduced contribution to oxidizer surface temperature.

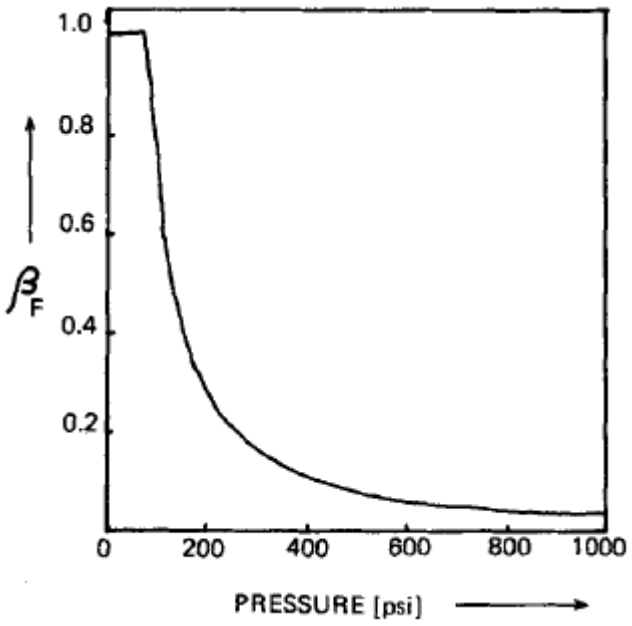

Figure 21: A plot of β_F versus pressure from Swaminathan and Soosaimarian (1981) that shows higher pressures lead to low β_F values. This behavior signifies the Monopropellant Flame coming closer to the oxidizer surface at a faster rate than the Primary Flame with increasing pressure.

Similar to the Monopropellant Flame, pressure governs the closeness of the Primary Flame to the propellant surface and is expressed as dimensionless parameters for the same reason as the Monopropellant Flame (Equations 34–36). The difference with the Primary Flame is that it has two dimensionless standoff distances, one for the portion of the flame situated over the AP crystal and the other is for the portion situated over the binder.

$$X^*_{PF} = \frac{m_{prop}}{k_{PF} P^{\delta_{PF}}} \tag{34}$$

$$\zeta_{PF,binder} = \frac{C_{p,oxidizersolid}}{\lambda_{oxidizergas}} m_{prop}\left(X^*_{PF} + X_{D,binder}\right) \tag{35}$$

$$\zeta_{PF,ox} = \frac{C_{p,oxidizersolid}}{\lambda_{oxidizergas}} m_{prop}\left(X^*_{ox} + X_{D,binder}\right) \tag{36}$$

3.8 Final Flame and Premixed Binder Flame Processes

As noted before, the Final Flame is not included in the energy calculations due to Cohen and Strand claiming that the flame had a negligible energy contribution to the temperature increase of the oxidizer compared to the Monopropellant and Primary Flames. However, from a structural standpoint, the Final Flame plays the role of diffusion flame with the products of the Monopropellant Flame reacting with the Primary Flame products. Above the Monopropellant Flame, O_2 (a product of the Monopropellant Flame) at 1400 K, reacts with the Primary Flame products as they diffuse into the Monopropellant Flame oxidizer stream. The reactions occur as quickly as fuel diffuses into the Final Flame because the O_2, being at the monopropellant flame

temperature, is highly reactive. The diffusion characteristics of the Final Flame result in the overall conical shape of the flame, as the flame speed is slower than the flow speed due to the rate of diffusion controlling the mixing.

The premixed binder flame is a newer development that was modeled in recent work by Gross and Beckstead (2009 and 2011), but is not modeled in this study. Gross used vorticity-velocity calculations and a detailed gas-phase kinetics mechanism to model diffusion flame behavior. The resulting flame structure was similar to the original BDP structure, but added a fourth structure: the premixed binder flame. The premixed flame is the result of fine particles of AP in the binder being homogenized with the binder causing the binder decomposition products to react in the premixed flame situated over the binder surface. This reasoning has been loosely applied to nanoparticle additive impact on the burning rate as well. The premixed binder flame is included in the model to aid in explanations in later sections and for general understanding. It should be noted that Gross' model also showed that the Final Flame was too far from the propellant surface to affect the burning rate, so its removal from the energy balance herein has been verified in more than one source.

3.9 Energy Balance – Determining the Oxidizer Surface Temperature

Once the self-sustaining combustion process begins, the energy releases from the Primary and Monopropellant Flames, the latent heat of vaporization of the AP, and the enthalpy requirements of the AP solid and gas contribute to the overall, steady-state surface temperature of the AP crystal. The AP crystal and the HTPB undergo

endothermic reactions via heat conduction from the flames. The increase in temperature causes exothermic decomposition of the AP and pyrolysis of the HTPB (Figure 19).

For model calculations, the energy releases of the different flames are weighted by their dimensionless flame standoff distances in the First Law equation, which is used to determine the energy of the AP crystal surface. However, prior to calculation of the energy balance, binder properties (surface temperature, mass flux, surface area, and heat required for the binder to undergo pyrolysis) are used to calculate the percentage of the Primary Flame that resides over the AP crystal, β_{ox} (Equation 37) which is key to determining how much energy from the Primary Flame heats the AP crystal. Note the division of β_F by A_{fh}. As previously discussed, this methodology is a departure from the original equation presented in Cohen and Strand to improve the model's burning rate sensitivity to pressure.

$$\beta_{ox} = 1 - \frac{m_{binder} S_{binder} \left[C_{p,condensed} \left(T_{binder} - T_o \right) + Q_{binder} \right]}{\left(m_{ox} S_{ox} + m_{binder} S_{binder} \right) Q_{PF} \exp\left(-\zeta_{PF,binder} \right)} \tag{37}$$

$$T_{oxidizer,calc} = T_o + \frac{\beta_{ox} \frac{\beta_F}{A_{fh}} \left(m_{ox} S_{ox} + m_{binder} S_{binder} \right) Q_{PF} \exp\left(-\zeta_{PF,ox} \right)}{C_{p,condensed} m_{ox} S_{ox}} + \frac{\beta_{ox} \left(1 - \frac{\beta_F}{A_{fh}} \right) \left(m_{ox} S_{ox} \right) Q_{AP} \exp\left(-\zeta_{ox} \right)}{C_{p,condensed} m_{ox} S_{ox}} - \frac{\Delta H_s + Q_L}{C_{p,condensed}} \tag{38}$$

Equation 38 is used to determine the surface temperature of the oxidizer crystal and acts as a convergence check against the initial guess at temperature given to the model algorithm. From a fundamental standpoint, the calculation of the surface temperature of the oxidizer can be viewed as:

$$\begin{aligned} T_{oxidizer,calc} = & \textit{ Initial temperature of the AP crystal} \\ & + \textit{Increase in temperature due to primary flame heating} \\ & + \textit{Increase in temperature due to monopropellant flame heating} \\ & - \textit{Change in temperature due to endothermic heat requirements of AP solid} \\ & \quad \textit{and exothermic heat release and crystal heating upon vaporization} \end{aligned}$$

Equation 39 is the overall burning rate calculated from the mass flux of the propellant as a result of the guessed oxidizer surface temperature and the propellant density.

$$r_{propellant} = \frac{m_{propellant}}{\rho_{propellant}} \tag{39}$$

3.10 Strand Burner Model

A model describing the complete propellant burning experiment is desired. To satisfy this requirement, the strand burner needs to be physically represented within the model to predict the thermodynamic changes that occur within the pressure vessel during testing. The strand burner model has two main objectives:

1. Mimic pressure rise during the burning of the propellant strand and any pressure decrease due to heat loss.
2. Infer time-averaged and time-changing burning rates from a measured pressure trace.

A strand burner model has been developed to approximate the pressure, temperature, and gas mixture changes using the ideal gas law and the First Law of Thermodynamics. The pressure trace prediction model is based on a model originally designed by Arvanetes in his work on a spectrometer diagnostic for the pressure vessel in the author's laboratory (Arvanetes, 2006). Strand burner dimensions and material properties were obtained from Carro's thesis that described the development of an improved strand burner facility (Carro, 2007). In the strand burner, it is assumed that the pressuring gas and propellant products mix perfectly to form an ideal gas mixture free of compressibility impacts. The strand burning experiment involves placing a stick or "strand" of propellant in a vessel pressurized to a specific pressure with an inert gas (like Argon) and igniting the strand to measure propellant burning rate at that given pressure (Figure 22).

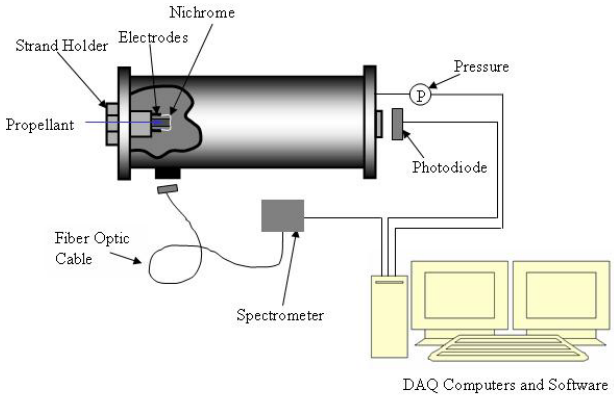

Figure 22: A schematic of the strand burner apparatus and supporting equipment (Stephens et al., 2007).

The model is conceptualized as a closed, fixed volume receiving incoming propellant gas products. As Figure 23 shows, the transient process of the First Law of Thermodynamics is used to determine thermodynamics changes between states. This simplified approach is a good candidate for the transient process as it is capable of "reasonably representing a first approximation of the thermodynamic changes of a closed tank filling with a gas or liquid" (Borgnakke and Sonntag). This hybrid "open-closed system" approach leads to mass accumulation in the volume and a resulting increase in system temperature and pressure. Using the ideal gas law and gas mixture relations, the pressure increase during the strand burn can be predicted.

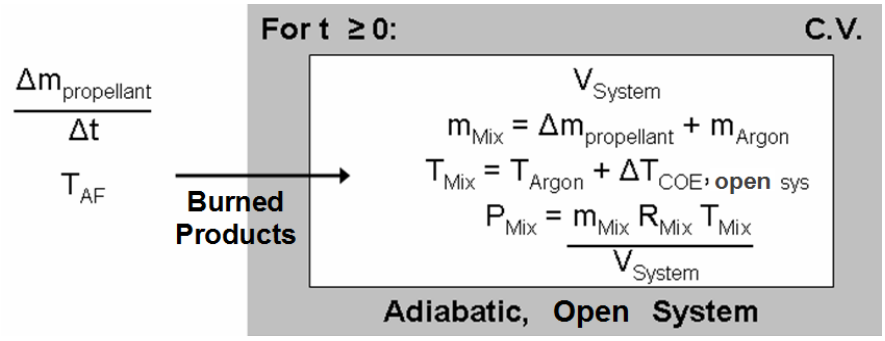

Figure 23: Illustration of the strand burner modeling concept showing how the model determines changes in system temperature and pressure.

In a strand burning experiment, the test time is measured and propellant performance is observed via a pressure trace provided by the diagnostic equipment (Figure 24). It is a key functionality of the present model to utilize an existing burning rate to accurately predict the complete pressure and to conversely infer a burning rate from a measured pressure output. The test time, or "burn time," is determined to be the time between the ignition of the propellant (marked by the initial increase in pressure) and the point at which the pressure peaks and begins to decay (propellant burn out), as seen in Figure 24. Light emission diagnostic data confirm this method to be the time of propellant combustion as light emission occurs at the initial pressure rise and disappears at maximum pressure (at the moment of propellant burn out).

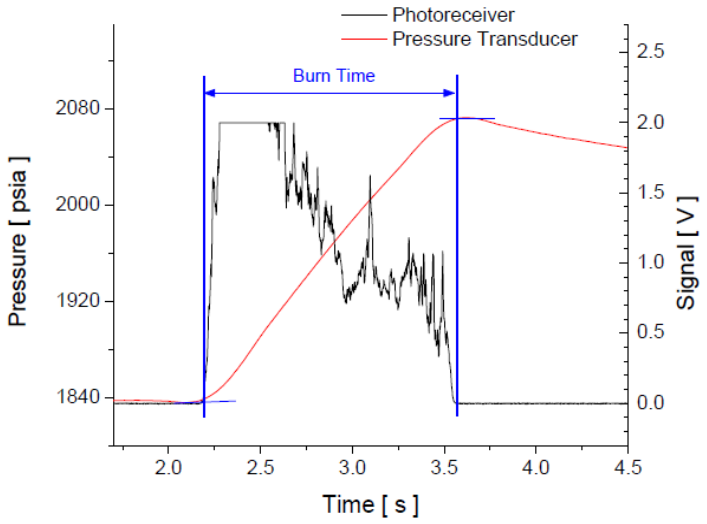

Figure 24: Measured pressure and light emission for a typical strand burning experiment (Kreitz, 2010).

Equation 40 shows how the experimentally determined burning rate is calculated from the pressure data. In Equation 40, r is the burning rate, Δx is the change in the propellant strand length, and Δt is the test time over which combustion occurs.

$$r = \frac{\Delta x}{\Delta t} \tag{40}$$

To accurately predict the pressure trace, the model needs to also account for heat transfer effects during and post-test. While conservation of energy and ideal gas mixture relations determined the pressure increase, the pressure loss the strand burner experiences post-test was modeled as a change in temperature as a result of heat transfer described in previous strand burner-modeling studies (Yilmaz et al., 2008; Glick and

Haun, 1990). Equation 41 is Newton's Law of Cooling with an exponential fit and is utilized in the model to predict post-test decay via free convection. The heat transfer coefficient utilized for the decay, and then applied during the test to estimate temperature and pressure loss, was calculated to be 14 W/m-K from an exponential fit of actual strand burner post-test decay data. The calculated value of *h* is within the range of free convection heat transfer (2.0–25.0 W/m-K according to Incropera and Dewitt). Flow within the chamber (from the ejection of hot propellant gases from the burning strand) is on the order of 10^{-5} m/s, which can be considered negligible velocity and eliminates forced convection from consideration. As previously stated, it is assumed that the heat transfer coefficient estimated is fairly constant and does not vary with different propellant formulations or test pressures. Since the chamber gas is predominantly Argon (~98% by mass), it is also assumed that changes in propellant formulation or test pressure produce insignificant changes in heat transfer coefficient for the gas mixture in the strand burner.

$$\frac{T - T_{Final}}{T_{Maximum} - T_{Final}} = e^{-\frac{hA}{nC_v}t} \tag{41}$$

To address condensation concerns expressed by Yilmaz et al., cursory analysis due to condensing H_2O was implemented into the model. Using Dalton's Law for gas mixtures from Borgnakke and Sonntag, and removing the energy and mass contribution of the water from the pressurized gas mixture within the strand burner, the model is able

to provide a better prediction of the pressure loss post-test. These relations were then used to predict a complete pressure trace (Figure 25).

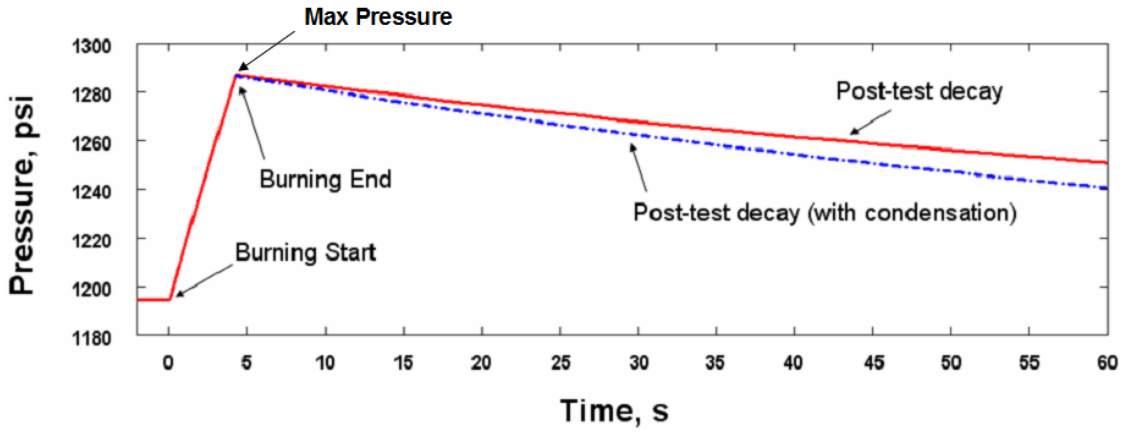

Figure 25: The complete pressure trace for a 70/30% AP/HTPB monomodal (200 μm) composite propellant with (dash-dot) and without (solid) condensation effects. The pressure increase is due to the burning propellant adding energy and mass to the system, and the post-test decay in pressure is due to heat loss and condensation effects.

4. BASELINE RESULTS

To verify the baseline model's predictive capabilities, initial calculations were performed comparing monopropellant burning rates and monomodal and bimodal AP/HTPB composite propellant burning rates to published literature and recent experimental data from the author's laboratory. This section provides results for the model's prediction of burning rates for AP monopropellant burning and baseline (non-nanoadditive) propellant formulations with 80% and 85% AP mass loading. Also, strand burner pressure trace predictions and estimated burning rates (transient and time-averaged) will be compared to experimental data. A table of typical model input values and tables of selected calculated results for 80/20 AP/HTPB can be found in Appendices E and F, respectively.

4.1 Monopropellant Burning Rate Results

Figure 26 shows the results of the model's predictions for a monopropellant. The model's predicted burning rates for a monopropellant formulation are plotted alongside another model prediction produced by Shusser et al. to study the combustion response of AP. The error between the present model and the Shusser model is 10% at a 316-psi test pressure and decreases to nearly zero at 3100 psi – a pressure range more than representative of the test range of interest.

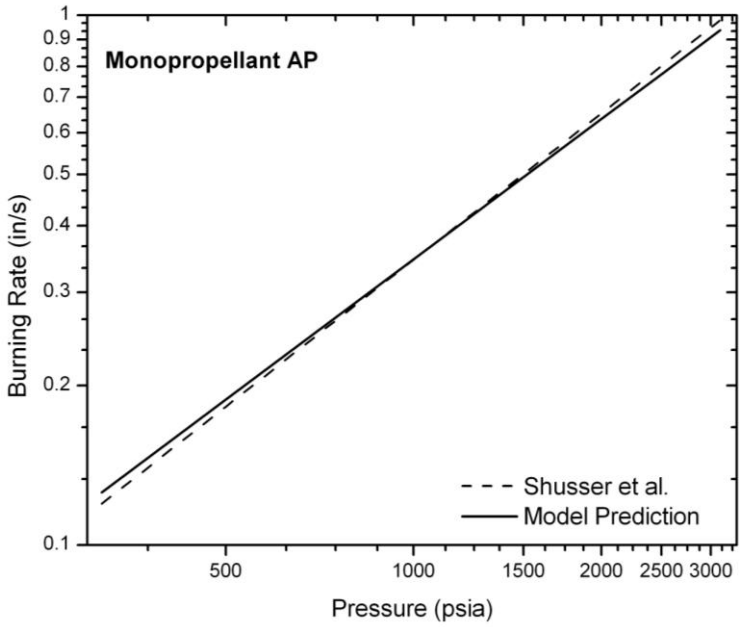

Figure 26: Burning rates for 20-μm AP monopropellant at various pressures. Model prediction is within 10% of previous research (worst case).

4.2 Baseline Propellant Burning Rate Results

Monomodal and bimodal AP/HTPB burning rate predictions also show promise. Monomodal formulations use a coarse (200-μm diameter) AP particle size, and bimodal formulations use a mix of the same coarse and fine (20-μm diameter) particle sizes. Smaller particle sizes facilitate an increased burning rate due to an increase in burning surface area. Monomodal and bimodal AP/HTPB formulations in Figure 27 show that model-predicted burning rates closely approximate experimental values and that the model determines an increased burning rate based on smaller particle sizes.

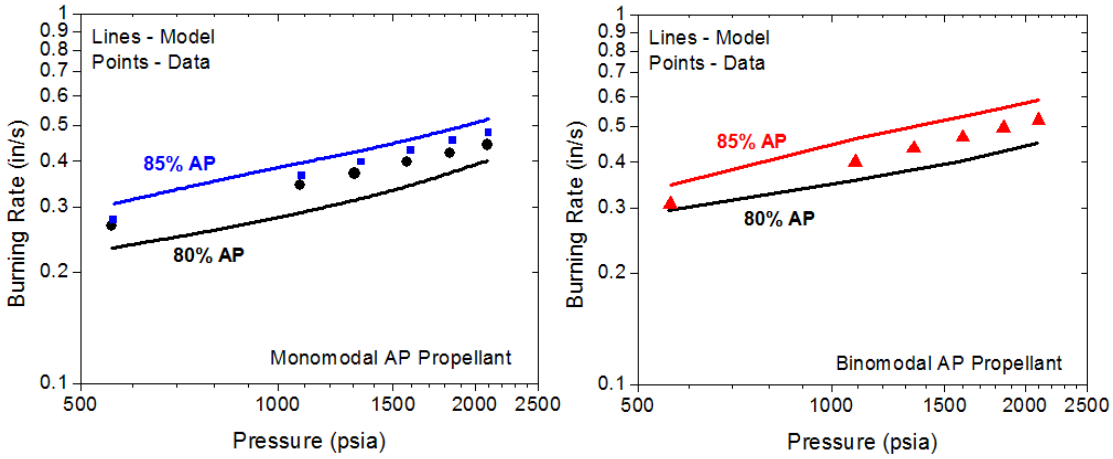

Figure 27: Experimental and predicted burning rates for monomodal and bimodal AP/HTPB propellant formulations at various pressures. Model prediction is within 15% of experiments. Measurements are from the author's laboratory at TAMU.

It is notable that the model is able to predict the burning rate exponent accurately for the cases shown in Figure 27. Table 3 shows the respective power law fits for the model and experimental data shown in Figure 27. Although the model predicts the relative effect of increasing AP mass percentage on burning rate, it overpredicts the effect relative to the measured behavior for the 85% formulation and underpredicts the effect for the 80% formulation.

Table 3: Power law equations for the model and experiment from Figure 27 for (a) monomodal and (b) bimodal formulations. Note how the model is most accurate when predicting the burning rate exponent, n. *P* is in psi and the burning rate is in in/s.

(a)

80/20 AP/HTPB	
Model	Experiment
$0.0174P^{0.41}$	$0.0239P^{0.38}$
85/15 AP/HTPB	
Model	Experiment
$0.0251P^{0.40}$	$0.0204P^{0.41}$

(b)

80/20 AP/HTPB	
Model	Experiment
$0.0413P^{0.31}$	--
85/15 AP/HTPB	
Model	Experiment
$0.0288P^{0.40}$	$0.0248P^{0.40}$

Figure 28 shows that the particle size of the AP greatly influences the burning rate and pressure sensitivity; and that there is a major difference in performance between coarse (200 μm) and fine (20 μm) AP. For this reason, many of the studies in this paper will be performed at 200 μm to ensure that parametric trends can be identified, as the high burning rate of smaller, finer particle sizes may overpower certain behaviors. It can also be seen that finer particle sizes will produce a diminishing increase in burning rate compared to coarser sizes; this may indicate a maximum burning rate, and such mixtures would be less sensitive to the affect of additives designed to increase the burning rate.

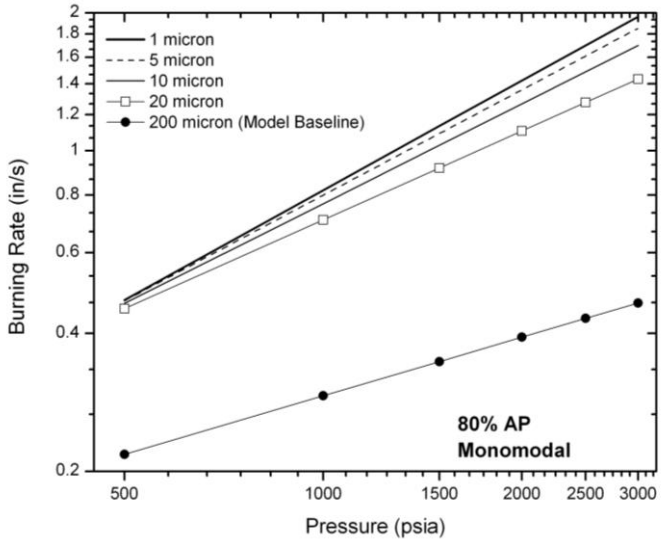

Figure 28: Model-predicted effect of particle size on the burning rate of an 80/20 AP/HTPB monomodal propellant. Finer particle sizes provide increased burning rates over coarser sizes, but the magnitude of the burning rate enhancement decreases suggesting a maximum burning rate.

4.3 Strand Burner Results

Figure 29 shows the complete model pressure trace plotted against an experimental pressure trace for a monomodal 80/20 AP/HTPB formulation run. The model assumes a constant burning rate provided by the burning experiment and models the heat loss during and post-test. The heat loss during the burn time is small, but noticeable, approximately a 14% temperature loss. The model estimates the post-test pressure decay within 10% of the measured pressure.

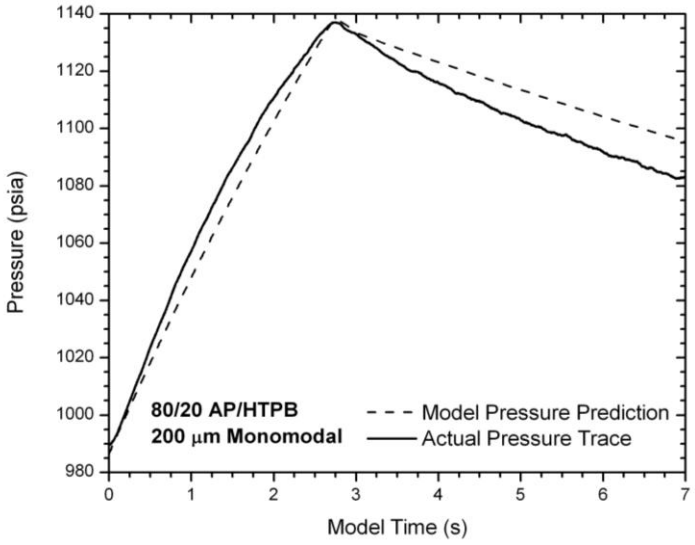

Figure 29: Complete predicted and actual pressure traces for an 80/20 AP/HTPB formulation run with heat transfer and condensation.

Figure 30 shows the maximum pressure predicted by the model (for the adiabatic situation) and recorded during experiments. The predicted maximum pressure is within 10 percent of the actual maximum pressure. Since the model over-estimated the maximum pressure for the adiabatic condition, adding in heat transfer during the test will make the calculations even more accurate.

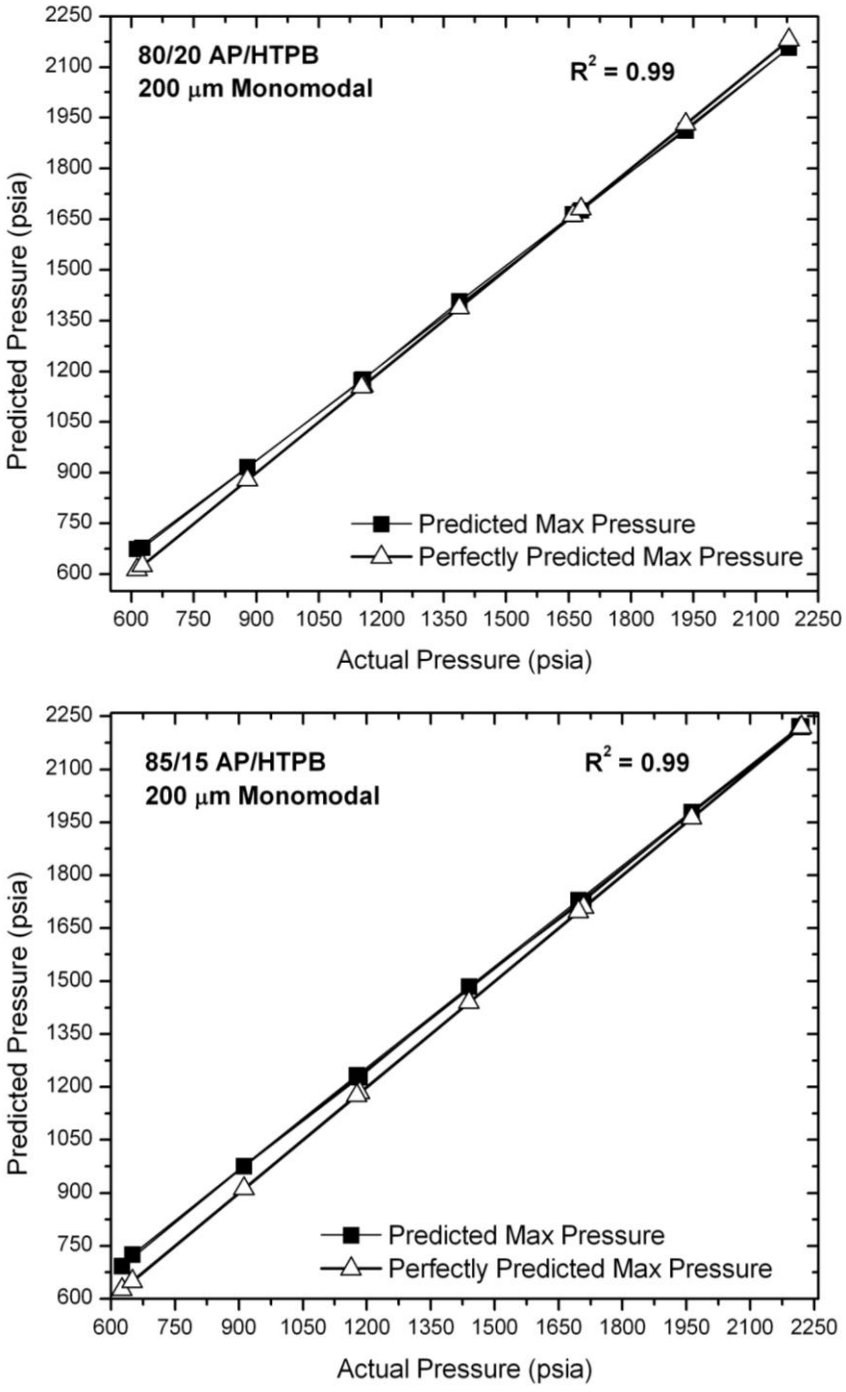

Figure 30: Maximum pressure achieved for 80/20 and 85/15 AP/HTPB formulation runs (adiabatic).

The model also uses measured pressure traces to determine burning rate changes over time. This model capability is useful in situations in which an error occurs in burning experiments and the model either has to extrapolate the burning rate of a given run based on data collected before the burning test failed or if the model has to estimate a burning rate following propellant re-ignition after a failed attempt to burn a complete strand. It is commonly assumed that the burning rate is relatively constant during the burn (varying by no more than 5 or 10 percent). Using the strand burner model, our laboratory is capable of determining the burning rate variation for individual runs and can determine if the experimentally determined burning rate is similar to the model-determined average burning rate. Figure 31 shows a model prediction of the change in burning rate over the test time. In this particular example the model determined that the burning rate actually varied by as much as 13% over the course of the burn (while only the average burning rate is typically reported from the experiment). Figure 31 also shows that the average burning rate determined by the model and the experimentally determined burning rate (via Equation 40) are similar, but if needed the model can be used to back out the actual variation in burning rate over the course of the entire burn.

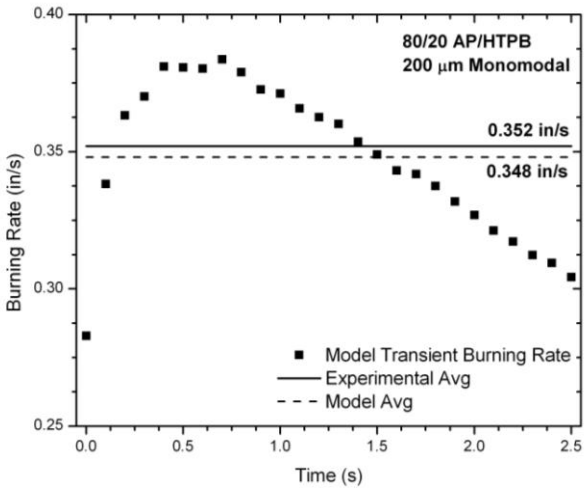

Figure 31: Estimated burning rate over test time for the 80/20 AP/HTPB formulation run featured in Figure 29.

Finally, the model's ability to predict average burning rates using an actual pressure trace is within 10% of the experimental burning rates over a range of pressures (Figure 32).

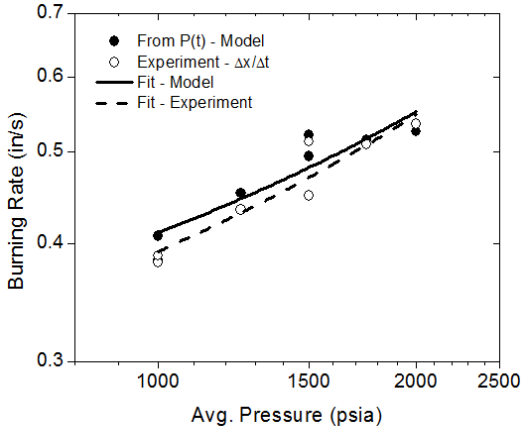

Figure 32: Estimated average burning rates for a group of 80/20 AP/HTPB formulation runs with 1% TiO_2 additive.

5. ADDITIVE PARAMETRIC STUDY

The incorporation of nanocatalytic effects can be investigated once the baseline composite propellants were modeled accurately. The application of nanoparticles to the overall model represents the new research performed herein and was the central motivation of this thesis. As part of the objective for modeling the effect of the nanoparticles, the combustion model was used to determine the aspects that impact the burning rate in which the nanoparticles could be playing a role. Additionally, this study provides insight as to which aspects of the model are impacted by nanocatalysts. The particular aspects of the model that could be affecting the burning rate are, but not limited to, surface and condensed-phase AP kinetics, HTPB kinetics, and Primary Flame gas-phase kinetics. The goal of this study was to approximate experimental nanocatalytic burning rates (Figures 11, 13, and 14) with parametric changes to the combustion model.

The next section contains a parametric study of the Primary Flame kinetics where the reaction rate and reaction order of the flame are manipulated. HTPB kinetics and regression rate are changed to attempt mimicking additive enhancements in the next section. Then the following section details the parametric study for AP condensed-phase kinetics. The final section contains the parametric study for AP surface kinetics.

5.1 Primary Flame Kinetics Study

Primary Flame kinetics were identified for the parametric study as Jones and Strahle (1973), suggested that catalysis occurs in the gas phase of the “O/F flame,”

which corresponds solely to the Primary Flame in the model. To model catalysis of the Primary Flame, the Primary Flame reaction rate, k_{PF}, and reaction order, δ_{PF}, were changed to study their effect on burning rate. Figure 33 shows that altering the reaction order and reaction rate cause the reactions within the flame to become or less pressure sensitive. The term k_{PF} is in units of $\frac{g}{cm^3 \cdot s \cdot atm^{\delta_{PF}}}$ which explains the similar look of the model data in Figure 33 since the reaction order directly influences the pressure sensitivity of the Primary Flame reaction rate.

For this analysis, k_{PF} was reduced by a factor of 8 to produce higher burning rates above the baseline, but as close to nanoadditive experiments as possible. δ_{PF} was reduced from 1.5 (baseline value) to 0.9 to achieve the same criterion of matching experimental burning rates with nanoparticle additives. The burning rates were increased as desired, but the overall slope of the burning rate as a function of pressure was drastically altered due to the fact that the reaction kinetics are influenced by pressure. This drastic slope change results in severe decreases in burning rate and surface temperature at lower pressures, even below that of the baseline model prediction. It should be noted that increasing the values of reaction order and the reaction rate reduces the sensitivity of the burning rate to pressure and results in burning rates much lower than those of nanoadditives at higher pressures. Additionally, the burning rate becomes less sensitive to pressure when δ_{PF} and k_{PF} are increased. For example, δ_{PF} = 3.0 yields burning rates of 0.234 in/s at 500 psi and 0.404 in/s at 2500 psi. When compared to the baseline values predicted by the model, 0.218 and 0.419 in/s at 500 psi and 2500 psi, respectively, this signifies a flattening of the burning rate slope compared to pressure.

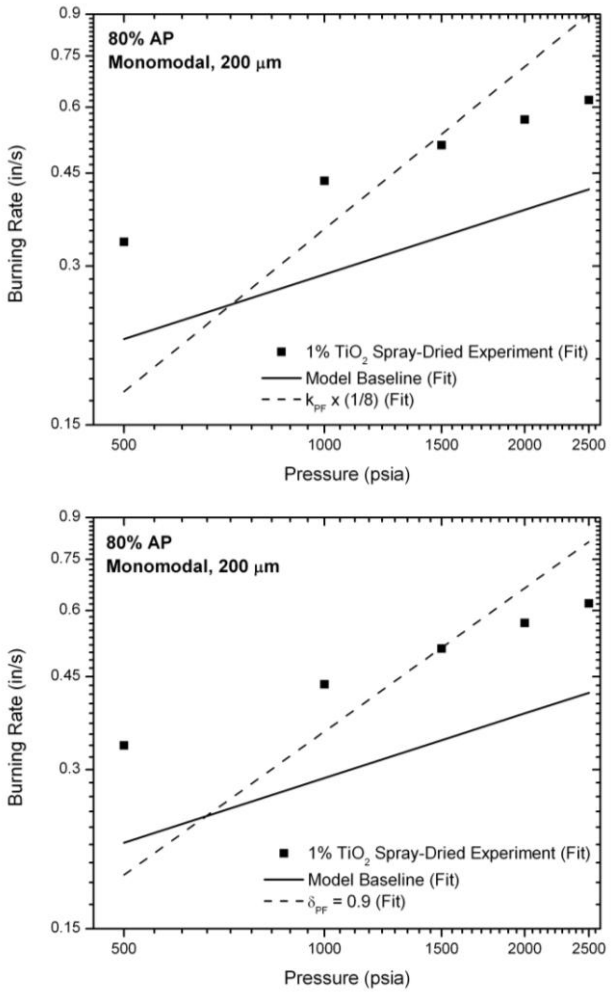

Figure 33: Burning rate plots showing the effect of changing Primary Flame reaction rate (k_{PF}) (top) and reaction order (δ_{PF}) (bottom) on burning rate. Changing the Primary Flame kinetics drastically changes the pressure sensitivity of the burning rate which is different from laboratory experiments with nanoadditives.

While the focus of this section is the Primary Flame, it is critical to the explanation of Primary Flame modeling to include discussion of why the

Monopropellant Flame reaction order was neglected. There is no "δ_{AP}" constant (reaction order of the Monopropellant Flame), as a possible flame parameter to be studied as there is no "k_{AP}" constant (reaction rate within the Monopropellant Flame). δ_{AP} is used in the classic BDP model, but in the Cohen-Strand model, k_{AP} is calculated by an Arrhenius expression (Equation 42) instead of using a constant influenced by a reaction order value similar to the calculation of k_{PF}.

$$k_{AP} = A_{AP} \exp\left(\frac{-E_{AP}}{RT_{AP}}\right) \tag{42}$$

In Equation 42, subscript "AP" means "Monopropellant Flame" and the temperature at which the rate is determined is the flame temperature of the Monopropellant Flame, which is 1400-1405K. Equation 42 is multiplied by P^2 to relate the Monopropellant Flame's sensitivity to pressure to flame standoff distance (Equation 31). Equation 42 uses A and E gas kinetics values for decomposed AP gas products reacting in the Monopropellant Flame.

Based on the analysis above, the flame parameters drastically alter the slope of the burning rate curve, which is not similar to the burning rate enhancements seen in laboratory experiments. However, the significance of pressure to the flame constants and the slope of the burning rate curve are now better understood. Additionally, this does represent another potential avenue for a dedicated kinetics model – to obtain the actual

reaction order and rate of the Primary Flame reactions to be integrated into the combustion model.

5.2 Binder Kinetics and Enhanced Burning Rate Study

The next phase of this study was to determine if it is possible to perturb the HTPB decomposition kinetics to match effects seen in experimental burning rate data with additives. Catalysis of binder thermal degradation has been proposed in previous studies by Fong and Hamshere (1986) among others and is currently one of the more widely accepted mechanisms for catalytic influence on the burning rate. In the model, HTPB decomposition (expressed in terms of a mass flux rate) is represented by Equation 27. In Equation 27, A is a kinetics prefactor in units of mass flux rate, E is the activation energy of the HTPB, R is the universal gas constant, and T is the surface temperature of the HTPB. To assess the relative impact of HTPB decomposition kinetics on burning rate, A_{binder} and E_{binder} were changed to check their relative impact on burning rate.

Figure 34 shows the effect of changing HTPB kinetics on burning rate. For this analysis, the kinetics prefactor was increased by a factor of 10 and the activation energy was lowered to zero. These are two extremes that should show a significant increase in the burning rate and be a clear determinant of nanocatalytic effects on HTPB kinetics, if any. For a propellant formulation of 200-µm, 80% AP with 20% HTPB, major binder kinetics changes have little effect. At higher pressures, the nanocatalyzed-HTPB may have an effect on burning rate, but overall the dramatic changes to HTPB kinetics do not produce burning rate increases reminiscent of those seen in laboratory experiments.

Figure 35 shows that for smaller AP particle sizes, the changes in HTPB kinetics have an even smaller effect on burning rate than they did in Fig. 34.

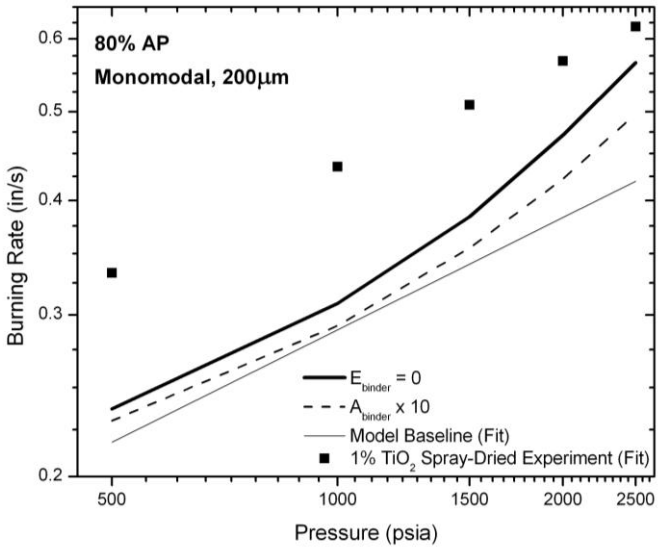

Figure 34: Effect of changing HTPB kinetics on burning rate over a range of pressures. Major changes in HTPB kinetics have little effect on burning rate.

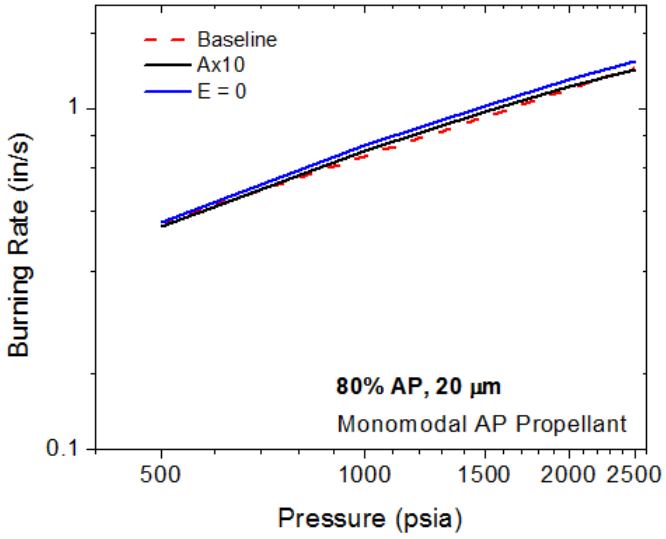

Figure 35: Effect of changing HTPB kinetics on burning rate over a range of pressures. Major changes in HTPB kinetics have an even smaller effect on burning rate for smaller AP particle sizes.

The negligible effect on burning rate of enhanced binder was also proposed, but not shown, by Chakravarthy et al. (1997), when they suspected that the surface of the ingredient that pyrolyzes faster will only become more recessed without considerably affecting the burning rate. Figure 36 further confirms that an increased binder burning rate (leading to a recessed binder surface) does not yield an increased propellant burning rate similar to additive experiments seen in the author's laboratory. In Figure 36, the binder burning rate is forcibly increased by factors of 2 and 10. Equation 43 is the calculation of the geometric factor, ζ, and shows how increasing the binder burning rate, r_{binder}, directly contributes to a recessed binder surface. A positive geometric factor

means that the binder surface is recessed below the AP crystal while a negative geometric factor corresponds to a binder surface above a recessed AP crystal.

$$\zeta_{P,N} = \frac{1}{2}\left(1 \pm \frac{1}{\sqrt{3}}\right)\left(1 - \frac{r_{ox}}{r_{binder}}\right) + r_{ox}\frac{t_{ign}}{D_{ox}} \tag{43}$$

The small impact of binder regression is significant because another theory regarding the impact of catalytic additives is that they enhance burning rates by catalyzing the binder and increasing binder regression. Then, there is a corresponding geometric impact that exposes more of the AP crystal and allows the propellant to burn more like a monopropellant, which yields a higher burning rate for the propellant. However, as Figures 34–36 show, this result is not the case.

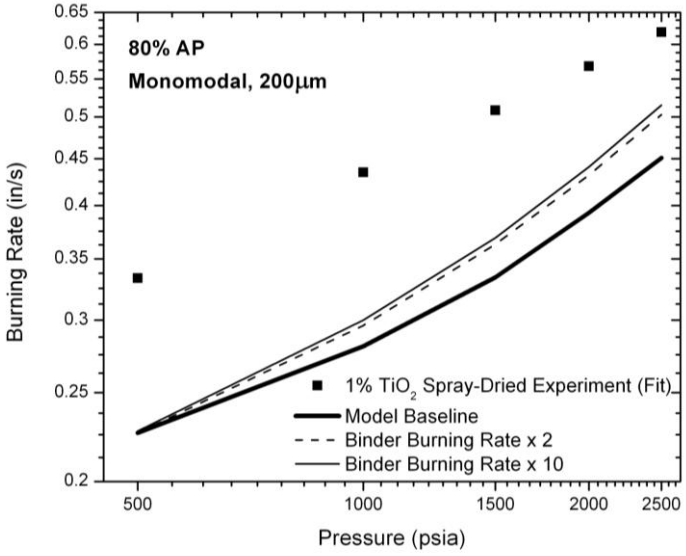

Figure 36: Burning rates for 80/20 AP/HTPB under normal conditions and with the binder burning rate directly modified by factors of 2 and 10. Increasing the binder burning rate by a factor of 2 increases the propellant burning rate by only 0.1 in/s, which is far less than experimental burning rates seen with additives. A factor of 10 shows little change in burning rate over a factor of 2.

5.3 AP Condensed Phase Kinetics Study

According to Chakravarthy et al. catalytic action in the condensed phase might lead to increased burning rate as exothermicity in the condensed phase is effective in transferring heat back to the propellant surface to accelerate decomposition and thus burning rate. For this reason it is worth investigating the impact of modifying the kinetics of the AP condensed phase on burning rate. Similar to the HTPB kinetics study, there are two parameters to be manipulated for parametric study: E_s, the activation energy of the AP condensed phase, and A_s, the reaction rate of the AP condensed phase.

For the activation energy, E_s was lowered to 120 kJ/mol and increased to 130 kJ/mol (normal value in the model is 125.6 kJ/mol) to evaluate the resulting effect on burning rate. The value 120 kJ/mol was utilized as the lower boundary because any value of E_s approaching 100 kJ/mol caused model failure. Figure 37 shows the burning rate change in response to changing E_s. As expected, increasing E_s resulted in a reduced burning rate, as the oxidizer would require more energy to react/decompose. However, it appears that decreasing the condensed-phase activation energy by as little as 5 kJ/mol results in a maximum burning rate behavior across all pressures. This implies that the activation energy of the condensed phase is negligibly altered by the presence of nanocatalysts as the parameter, at least within the constraints of the present model, is too sensitive to be changed in a manner that increases burning rate.

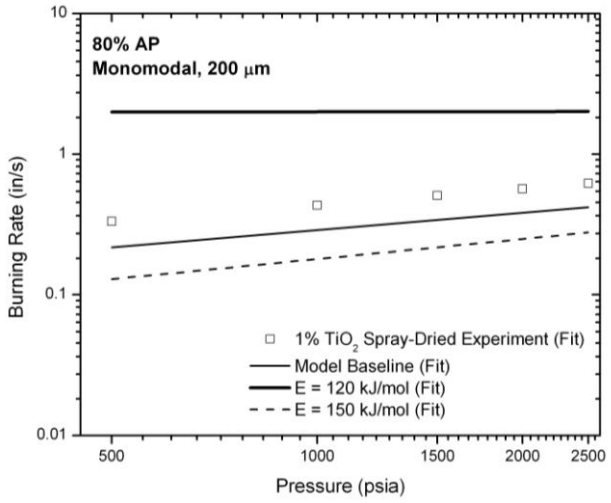

Figure 37: Model prediction of an 80/20 AP/HTPB propellant with modified condensed phase AP activation energies. The baseline E_s is 125.6 kJ/mol. A small decrease in E_s leads to a maximum burning rate over the entire pressure range.

The reaction rate of the condensed phase, A_s, was increased by as much as a factor of 2 in an attempt to replicate additive burning rates. A factor of 1.5 reproduced a burning rate increase seen experimentally for 1% TiO_2 spray-dried additive for an 80/20 AP/HTPB propellant (Figure 38). A 50% increase in the reaction rate also seems reasonable, in light of potential catalytic activity inducing such an increase.

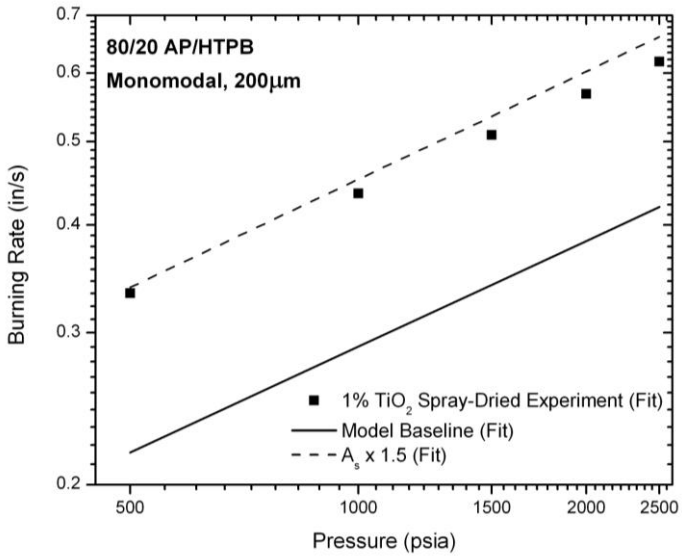

Figure 38: An increased AP condensed-phase reaction rate (by a factor of 1.5) accurately predicts the burning rate trend of an 80/20 AP/HTPB propellant with 1% spray-dried TiO_2 additive. The burning rate enhancement maintains the same pressure sensitivity which is also seen in burning rate experiments.

While catalysis of AP condensed phase is counter to the common theory of how additives influence burning rates (catalysis of the binder has been a more widely accepted theory) it has not gone without proposal. Previous research has suggested that

catalysis of AP deflagration (Jones and Strahle, 1973; Boggs et al., 1988) or decomposition is caused by additives influencing proton transfer (Pearson, 1971) or electron transfer (Kishore and Sunitha, 1978). Additional research with particular emphasis on chemical action in the condensed phase suggests that additive influence could be occurring at the AP/binder interfacial surfaces (Krishnan and Jeenu, 1990; Krishnan and Jeenu, 1992; Krishnan and Periasamy, 1986); or that additives could be altering the decomposition products of AP and binder (Pearson, 1971); or by catalyzing $HClO_4$ decomposition, the products of which eventually enhance binder degradation (Korobeinichev et al., 1975) or by catalyzing polymer degradation via $HClO_4$ oxidation (Korobeinichev et al., 1978).

According to Brill and Budenz (2000), the relative proportion of condensed-phase chemistry is higher when an additive such as TiO_2 is present corresponding to increased condensed-phase presence following oxidizer mass loss. The value of β_p for the baseline formulation for an 80/20 AP/HTPB monomodal propellant was compared to that of a similar formulation with 1% TiO_2 (using model approximations) to provide a physical reasoning behind model trends. The term β_p in the model is the percent of oxidizer mass that is reacting in the gas phase (and $1-\beta_p$ is how much mass-fluxed oxidizer remains in the condensed phase undergoing reactions). If the enhanced burning rate is the result of increased condensed phase reactions identified in Brill and Budenz, which results in increased exothermic heat releases, then the model should see a reduced β_p for model-simulated additive runs compared to that of the baseline (indicating less gas-phase chemical activity upon decomposition and more condensed-phase activity).

Figure 39 shows that the model predicts the same behavior that was predicted by Brill and Budenz.

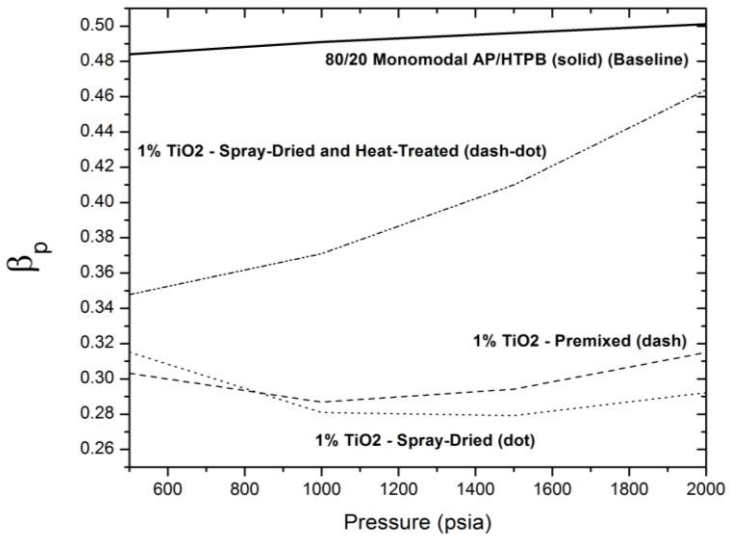

Figure 39: Model-determined β_p over a range of pressures for a monomodal 80/20 AP/HTPB propellant with and without additives. The plot shows that when additives are present in the propellant that AP exists more in the condensed phase than in the gas phase upon oxidizer mass loss (shown by a reduction in β_p) when additives are present. β_p for the premixed and spray-dried additives is lower than the spray-dried and heat-treated additive corresponding to the enhancements in burning rate seen in those two additive types over spray-dried and heat-treated formulations.

A major goal of this research was to use the model to help understand the possible mechanisms behind nanoparticle additives producing increased burning rates. Based on the results discussed above, modifying the condensed-phase reaction rate

seems to be one of the only ways the model can be modified to mimic the increased burning rates due to catalytic nanoparticles. Now the model can be used to determine why having faster condensed phase reactions during AP decomposition increases the burning rate; and why increasing the AP condensed-phase reaction rate increases the AP condensed-phase percentage when the oxidizer loses mass. In the model, the equation for β_p is given by Equation 44.

$$\beta_p = 1 - \frac{A_s \exp\left(\frac{-E_s}{RT_{oxidizer}}\right)}{m_{ox}} \tag{44}$$

A_s is the parameter that was modified by the factor introduced in this thesis, Ω_c, to replicate nanoparticle behavior. A_s is in terms of g/cm^2-s, which is a mass flux rate so the numerator in the β_p equation is the mass flux rate of the condensed phase AP. This equation means that β_p = 1 – "percentage of oxidizer lost *to* the AP condensed phase" since the mass flux of the oxidizer, m_{ox}, is due solely to thermal decomposition. Alternatively, this relation also means that β_p is the "percentage of oxidizer lost *to* the AP gas phase," the common definition for β_p. In other words, β_p represents the fraction of AP reacting in the gas phase of the Monopropellant Flame. Thus, there is more condensed phase present when A_s is increased because Equation 44 is modeling more AP mass lost to the condensed phase than the gas phase due to thermal decomposition when A_s is larger.

Since an increased condensed-phase mass flux (or reaction rate) correlates to an increased burning rate that replicates what happens in the presence of the additives, it is important to investigate the physical reasoning behind this phenomenon for improved model development and further experiments. Equations 45–48 are used to calculate the energy content and heat releases of the flame structure in the model.

$$Q_F = C_{p,APgas}\left(T_{AP} - T_{ref}\right) - C_{p,APcondensed}\left(T_o - T_{ref}\right) + \Delta H_g \tag{45}$$

$$Q_L = \beta_p\left(\Delta H_{ev} - \Delta H_g\right) - Q_F\left(1 - \beta_p\right) \tag{46}$$

$$Q_{AP} = Q_F - Q_L \tag{47}$$

$$Q_{PF} = C_{p,APgas}\left(T_{AF} - T_o\right) + \alpha_{ox} Q_L + Q_{binder}\left(1 - \alpha_{ox}\right) \tag{48}$$

Q_F is the total heat content of the AP Monopropellant Flame. The total heat energy of the Monopropellant Flame should not change unless initial temperatures or oxidizer thermophysical properties are altered. Q_L is the heat release of the AP as it decomposes into a gas. This energy release takes away energy that would be used as an input to the gas-phase combustion reactions of the Monopropellant and Primary Flames via the reactants of which decomposed AP are a portion. The energy released during gasification is transferred to the oxidizer crystal, increasing its surface temperature. Q_{AP} is the heat release associated with gas-phase reactions occurring in the Monopropellant Flame. Q_{PF} is the heat release associated with the combustion reactions occurring in the Primary Flame.

Table 4: Model-calculated energy data for a monomodal 80/20 AP/HTPB propellant burned at 500 psi. Energy data are provided for a formulation with and without a simulated 1% TiO_2 spray-dried additive (A_s multiplied by a factor of 1.5).

	80/20 AP/HTPB @ 500 psi	80/20 AP/HTPB @ 500 psi Simulated 1% spray-dried TiO_2
β_p	0.483	0.315
Q_F	483.55 cal/g	483.55 cal/g
Q_L	-64.82 cal/g	-210.15 cal/g
Q_{AP}	418.72 cal/g	273.39 cal/g
Q_{PF}	605.55 cal/g	489.29 cal/g

According to Table 4, more heat is released by the AP when it vaporizes under nanoadditive modeling conditions (Q_L) due to more chemical reactions occurring in the condensed phase which allows the AP to break down further and release more energy upon vaporization. This increase in heat release between the baseline and additive simulation reflects the same exothermic enhancement suggested by Chakravarthy and coworkers and seen in Brill and Budenz. Q_{AP} and Q_{PF} are the energy releases of the Monopropellant and Primary Flames, respectively, during the combustion process. Recalling that combustion reactions within the overall model control volume are adiabatic, less energy is released from the combustion steps in the Monopropellant and Primary Flames (in the additive simulation, Table 4) because less energy is input to the combustion reaction as a result of the AP releasing more energy when it becomes a gas. This process may indicate that the AP could also be decomposing along different pathways from the condensed phase than the main AP decomposition mechanism under baseline conditions. Beckstead (2007) presented several other mechanisms than the $AP_{(l)}$

→ $NH_3 + HClO_4$ pathway which is typically the path taken. Table 5 shows the known condensed-phase AP decomposition reactions and their associated kinetics.

Table 5: Condensed phase reaction mechanisms and kinetics parameters for AP decomposition from Beckstead (2007).

No.	Reaction Mechanism	A[a]	E[a]
1	$AP_{(l)} \rightarrow NH_3 + HClO_4$	8.0×10^{12}	28,000
2	$AP_{(l)} \rightarrow H_2O + O_2 + HCl + HNO$	1.0×10^{8}	22,000
3	$AP_{(l)} \rightarrow 2H_2O + Cl + NO_2$	5.0×10^{7}	22,000
4	$AP_{(l)} \rightarrow ClO_3 + NH_3 + OH$	1.0×10^{9}	22,000

[a]Units are in mol, cm, s, K, and cal

Based on the above discussion, it is proposed herein that nanoadditives are catalyzing processes within the AP melt layer (either through direct catalysis of the melt layer or through catalysis of decomposition products contained in gas bubbles suspended in the layer) allowing for further breakdown of species within the melt layer. This catalyzation process causes an increase in AP condensed-phase reactions and a concurrent decrease in gas-phase reactions such that condensed-phase reactions 1-4 occur in an increased frequency. Reactions 2-4 have slower reaction rates than reaction 1; the lower activation energy requirement for these reaction mechanisms could also allow for more heat release during gasification, making the transition from liquid to gas phase more exothermic.

The extra energy release from gasification during decomposition further heats the AP crystal, increasing the surface temperature and enhancing the burning rate, more than the baseline situation. The increased oxidizer heating resulting from an enhanced exothermic energy release upon vaporization is why increasing the AP condensed phase reaction rate contributes to an increased propellant burning rate. In Figure 40, an illustration of the change in the impact of exothermic heating, and how the flames contain less energy to transfer, is shown.

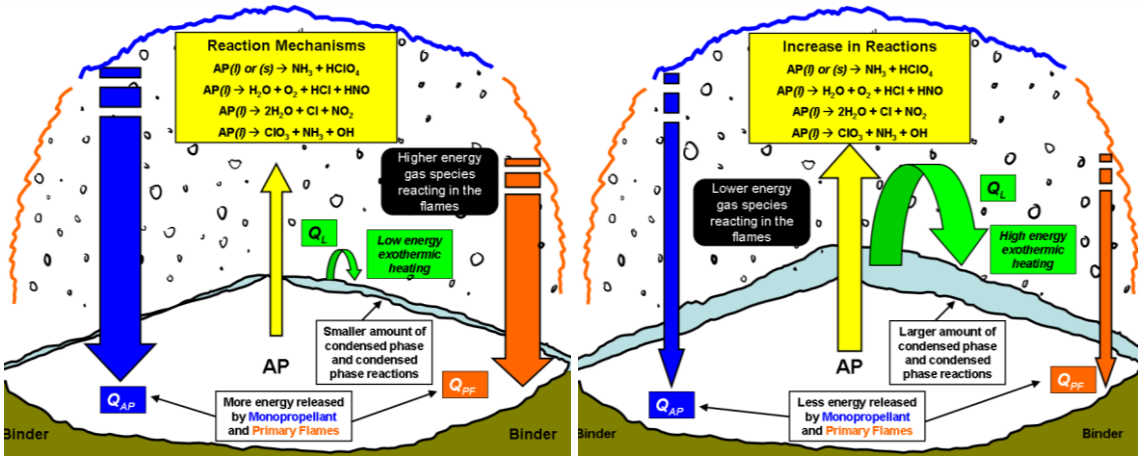

Figure 40: Illustration of the theory of how increased condensed phase presence increases exothermic heating by following different AP decomposition paths.

An addition to this theory by the current model configuration (which will require further validation in future research) is that if some or all of reactions 1-4 are occurring in higher amounts with nanoparticle additives, then more species are also becoming available to react with HTPB pyrolysis products in the Primary Flame (in one of the 72 reactions outlined by Jeppson) due to condensed phase breakdown of AP products. This

increased frequency of reactions from further broken down reactants (AP decomposition products and HTPB pyrolysis products) could trend toward a more premixed behavior in the Primary Flame rather than a diffusion flame; similar to how small-sized AP crystal suspensions react with HTPB pyrolysis products more easily to form the Premixed Binder Flame studied by Gross and Beckstead (2009 and 2011). The premixed situation would result in sped up burning rates as the Primary Flame would be less limited by the diffusion rate of the HTPB pyrolysis products. Nanoparticles may possibly enhance burning rates not only by allowing the AP to break down further in the condensed phase and limiting sublimation, but also through providing more reactants, or more easily reactive components (perhaps, as mentioned before, by catalyzing $HClO_4$ decomposition and the products enhancing binder degradation), to participate in Primary Flame reactions and increase the amount of available reactions taking place, thus causing the Primary Flame to trend more towards premixed behavior. Figure 41 shows an illustration of the theory.

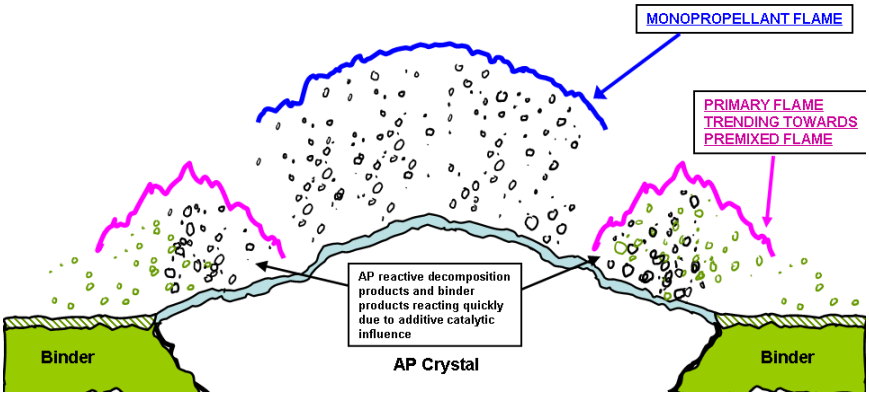

Figure 41: Illustration of the theory that the AP decomposition products are decomposed further than normal and react with the HTPB pyrolysis products and cause the Primary Flame to trend towards a premixed flame behavior.

5.4 AP Surface Kinetics Study

AP surface kinetics were part of the parametric study because, according to Chakravarthy, burning rates could be enhanced through activity in the gas phase by catalysis of $HClO_4$ decomposition (Pittman, 1969) with heterogeneous surface reactions playing a role (Pearson, 1971).

Figure 42 shows that changing the AP surface kinetics results in a reduced or negligibly changed burning rate. In Figure 42, changes in activation energy, E_{ox}, range between 120 kJ/mol and 150 kJ/mol (the baseline is 134 kJ/mol) and the reaction rate, A_{ox}, is changed by factors of 0.5 and 10. For increases in reaction rate and decrease in activation energy it is expected to see an increase in burning rate, not a decrease. The surface temperatures for a 500 to 2500 psi range of pressures is 748K to 790K for those situations, much lower than the baseline surface temperatures which are 850K to 900K

for the same pressure range. For increases to activation energy and decreases to reaction rate, a negligible burning rate results with unrealistic energy releases and low surface temperatures ~600K (Table 6).

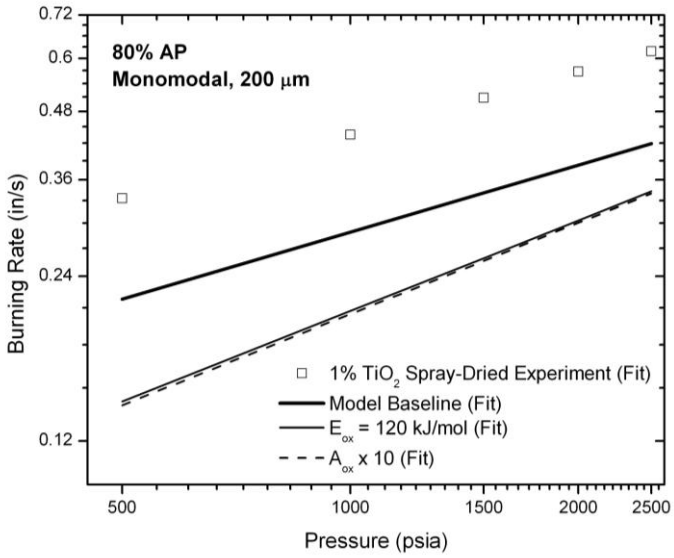

Figure 42: Model prediction of an 80/20 AP/HTPB propellant with modified AP surface kinetics (E_{ox} = 120 kJ/mol and A_{ox} x 10). The baseline activation energy is 134 kJ/mol. Lowering E_{ox} and increasing A_{ox} results in a decrease in the burning rate.

In the model, E_{ox} and A_{ox} directly influence the mass flux of the oxidizer, m_{ox}, via the Arrhenius expression in Equation 28, and thus, indirectly affect the mass flux of the binder, oxidizer/binder burning rates, geometric properties of the propellant surface, overall mass flux of propellant, and flame standoff distance calculations. Since the AP crystal surface sublimates into a gas under the conditions in Figure 42, the AP decomposition process becomes significantly endothermic, as Q_L becomes a positive

value. The lost opportunity to heat the crystal further through exothermic heat release results in lower oxidizer surface temperatures and increased flame energy releases shown in Table 6.

Table 6: Model-calculated energy data for a monomodal 80/20 AP/HTPB propellant burned at 500 psi. Energy data is provided for a formulation with and without a change to surface kinetics parameters, A_{ox} and E_{ox}.

	80/20 AP/HTPB (Baseline)	A_{ox} x 0.5 E_{ox} = baseline	A_{ox} x 10 E_{ox} = baseline	A_{ox} x baseline E_{ox} = 120 kJ/mol	A_{ox} x baseline E_{ox} = 140 kJ/mol
β_p	0.483	Unrealistic (negative)	0.938	0.935	Unrealistic (negative)
Q_L	-64.82 cal/g	Unrealistic (extremely exothermic)	330.52 cal/g	327.52 cal/g	Unrealistic (extremely exothermic)
Q_{AP}	418.72 cal/g	Unrealistic (negative)	814.06 cal/g	811.07 cal/g	Unrealistic (negative)
Q_{PF}	605.55 cal/g	Unrealistic (negative)	921.83 cal/g	919.43 cal/g	Unrealistic (negative)

*A_{ox} baseline = 1.5665 x 10^8 g/cm^2-s, E_{ox} baseline = 134 kJ/mol

The increase in endothermic behavior can be seen when evaluating β_p. In these influenced situations when the surface kinetics have an increased reaction rate and decreased activation energy, β_p is greater than 90%, whereas β_p is ~50% in the baseline situation. An increased β_p (especially to this extent) signifies a significant increase in sublimation, which means that the condensed phase plays a smaller role in AP decomposition, and the heat of gasification of the AP becomes endothermic instead of exothermic. As mentioned in the AP condensed phase kinetics parametric study, sublimation follows a reaction mechanism that requires more energy than the other mechanisms in Table 5. Such a substantial increase in sublimation could turn the AP decomposition process from an exothermic one into an endothermic one, as the more endothermic reaction mechanism would dominate and more energy is required to undergo sublimation rather than melting then vaporization.

Due to a reduction in AP surface temperature and thus burning rate, modification of the AP surface kinetics, representing an influence on AP gas-phase reactions, is not responsible for the increase in burning rate seen by nanoparticle additives.

6. ADDITIVE MODELING

The results of the parametric study show that the additives are most likely influencing the AP condensed phase reaction rate, A_s, by a constant factor through increased heating of the AP surface from a greater heat release when the condensed phase gasifies. To provide the model with the capability of modeling additive enhancements on the burning rate, a constant term, dubbed Ω_c, was developed that would be modified to replicate the experimental burning rate of an additive propellant at a given pressure. From this constant, a correlation was attempted as a function of pressure (from 500 to 3000 psi, a range that encompasses testing ranges in the laboratory). In actuality, Ω_c is a function of test pressure, AP loading, additive diameter, additive thermophysical properties, additive concentration, additive dispersiveness (f_c), and, in the case of doped additives, dopant concentration and dopant thermophysical properties as well (Equation 49).

$$\Omega_c = const = f\left(P, \alpha_{ox}, D_{additive}, C_{p,additive}, \lambda_{additive}, \alpha_{additve}, C_{p,dopant}, \lambda_{dopant}, \alpha_{dopant}, f_c\right) \quad (49)$$

Due to limited experimental data to develop the correlations as a function of the complete parameter list in Equation 49, correlations were developed for spray-dried/heat-treated additives, spray-dried additive, and a premixed additive for a 1% TiO_2 concentration for monomodal and bimodal formulations and 80% and 85% AP

concentration. The commonality in additive characteristics between the various cases transforms Equation 49 into Equation 50.

$$\Omega_c = const = f(P) \tag{50}$$

To determine the value of Ω_c, the guessed surface temperature of the AP was changed until a burning rate was reached that was approximately the same as the experimental burning rate for a given pressure. Then Ω_c was changed until the conservation of energy equation in the model returned a surface temperature equivalent to the guessed surface temperature.

6.1 Spray-Dried/Heat-Treated Additive Modeling

The Spray-Dried/Heat-Treated case was correlated with pressure ($R^2 = 0.76$) which is represented by Equation 51.

$$\Omega_{c,spray-dried,heat-treated} = const = \frac{42.54}{P^{0.228}} \tag{51}$$

In Equation 51, P is in Pa. Since Ω_c is a dimensionless parameter, the constant in Equation 51, 42.54, is in Pa raised to a power of 0.228. A plot of the model-predicted burning rate for Spray-Dried/Heat-Treated TiO_2 additive is shown in Figure 43. The

model prediction is within 3% error of the experimental correlation over a range of pressures that encapsulates the test pressures used in the laboratory.

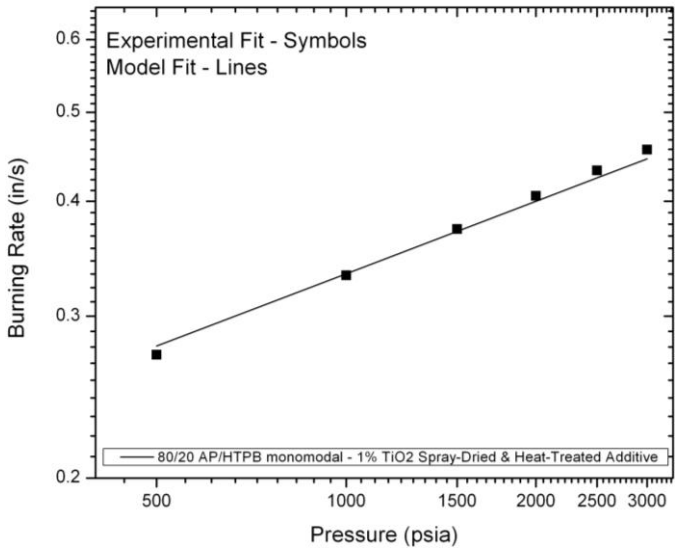

Figure 43: Plot of monomodal 80/20 AP/HTPB with 1% Spray-Dried and Heat-Treated TiO_2 nanoadditive. The model prediction is within 3% of the experimental correlation.

6.2 Spray-Dried Additive Modeling

The spray-dried (non-heat-treated) case was correlated with pressure however the correlation was weak ($R^2 = 0.13$) with Ω_c values. The additive influence on burning rate being pressure insensitive is different from the conclusion reached by Beckstead (1977) but it is in line with what was observed experimentally in Kreitz et al. (2011). In Figure 11, from Kreitz et al. (2011), it can be seen that experimentally there was a burning rate increase between the baseline and spray-dried additive formulations without a change in pressure sensitivity. This similar pressure sensitivity between the two formulations

explains why there was a weak correlation with pressure for the spray-dried additive case.

For this case, an average Ω_c can be calculated from the individual Ω_c values determined by the model at each pressure between 500 and 3000 psi. The average Ω_c can then be applied across the entire pressure range for spray-dried formulations (Equation 52).

$$\Omega_{c,spray-dried} = const = 1.41 \tag{52}$$

Figure 44 shows the plot of the model-predicted burning rate for spray-dried TiO_2 additive. Like the spray-dried and heat treated case, the model prediction agrees well with the experimental correlation with the error less than 8% across the entire pressure range.

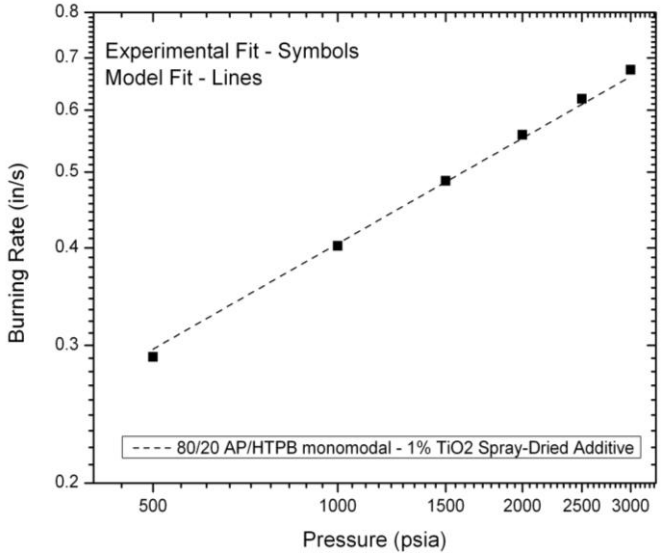

Figure 44: Plot of monomodal 80/20 AP/HTPB with 1% spray-dried (non-heat-treated) TiO_2 nanoadditive. The model prediction of the burning rate is within 8% of the experimental correlation.

6.3 Premixed Additive Modeling

Similar to the spray-dried (non-heat-treated) case, the premixed monomodal and bimodal cases also displayed only a weak correlation with pressure ($R^2 \approx 0.3$) for Ω_c values. Figures 13 and 14, also from Kreitz (2010), show the same consistency in pressure sensitivity between the baseline and premixed additive formulations in experiments, coinciding with the reaction rate enhancement factor being pressure insensitive and a weak correlation.

An average Ω_c was also calculated from the individual Ω_c values determined by the model at each pressure between 500 and 3000 psi for bimodal and monomodal premixed formulations of 80 and 85% AP (Equations 53 and 54). Also corresponding to

research by Kreitz, the reaction rate enhancement factor is greater for monomodal than bimodal formulations (for a similar concentration of nanoadditive for both modalities). This behavior occurs because the constant additive concentration is unable to catalyze the increased amount of reaction sites available for bimodal formulations, so the burning rate enhancement is smaller for bimodal than monomodal formulations as there is too little additive. Equation 54b is less than 1.0 because the model overestimates burning rates for 85% AP bimodal formulations to an extent that is slightly greater than the experimental nanoadditive burning rate.

$$\Omega_{c,\ premixed,\ mono,\ 80\%} = const = 1.38 \tag{53a}$$

$$\Omega_{c,\ premixed,\ mono,\ 85\%} = const = 1.23 \tag{53b}$$

$$\Omega_{c,\ premixed,\ bi,\ 80\%} = const = 1.02 \tag{54a}$$

$$\Omega_{c,\ premixed,\ bi,\ 85\%} = const = 0.93 \tag{54b}$$

Figures 45 and 46 show model-predicted burning rate for premixed TiO_2 additive and experimentally correlated burning rate. The model prediction agrees well with the experimental correlation with the error being 10% or less across the entire pressure range.

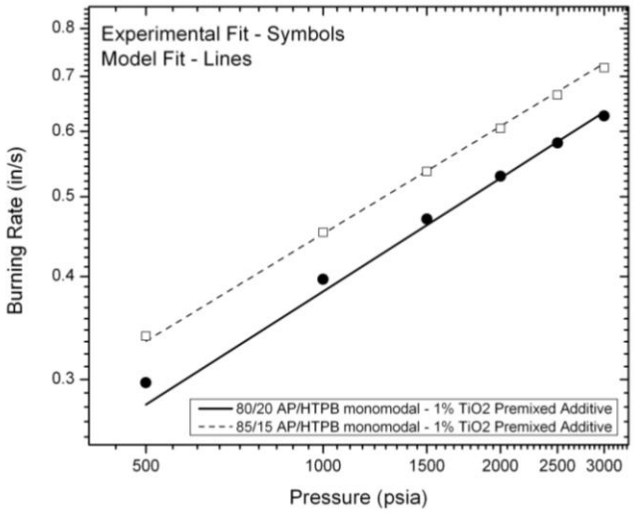

Figure 45: Plot of monomodal 80/20 and 85/15 AP/HTPB with 1% premixed TiO_2 nanoadditive. The model prediction of the burning rate is within 10% of the experimental correlation for both formulations.

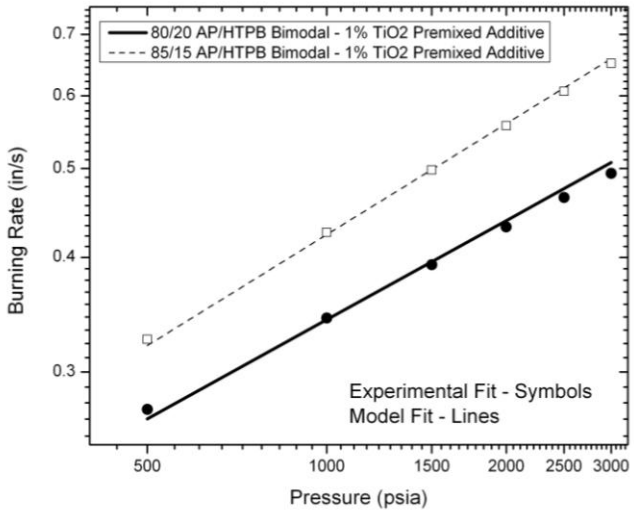

Figure 46: Plot of bimodal 80/20 and 85/15 AP/HTPB with 1% premixed TiO_2 nanoadditive. The model prediction of the burning rate is within 8% of the experimental correlation for both formulations.

7. ANOMALOUS BURNING MODELING AND DISCUSSION

In previous sections on HTPB regression, research was cited that suggests that the HTPB is being regressed at much higher rate than normal due to the nanoadditive influence, thus increasing the propellant burning rate. As part of the previous parametric study, a constant was utilized to allow for a specific increase in binder regression rate throughout the model beyond simply modifying r_{binder} in Equation 43 such that flame calculations would also be directly affected. Utilizing such a term created the anomalous burning behaviors seen in Figure 47. The anomalous burning predictions in Figure 47 resemble anomalous burning observed experimentally in our laboratory. Figure 48 shows illustrations of three types of off-nominal burning behaviors: plateau burning, mesa burning, and intermittent extinction. According to Williams (2010), anomalous effects are usually caused by the addition of certain burning-rate catalysts to the propellant formulation. The catalysts are thought to modify the interactions that occur in the condensed phase reaction zones of the propellant.

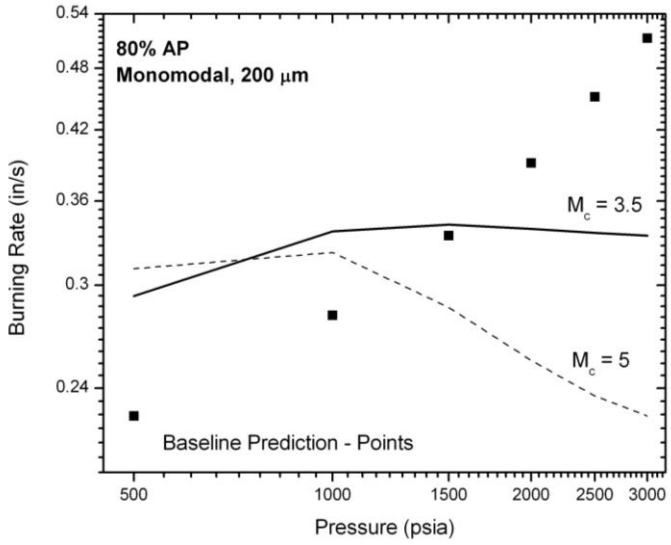

Figure 47: Anomalous burning rates for a monomodal 200 μm 80/20 AP/HTPB propellant with M_c = 3.5 and 5. M_c = 3.5 displays plateau characteristics and mesa burning is mimicked in M_c = 5.

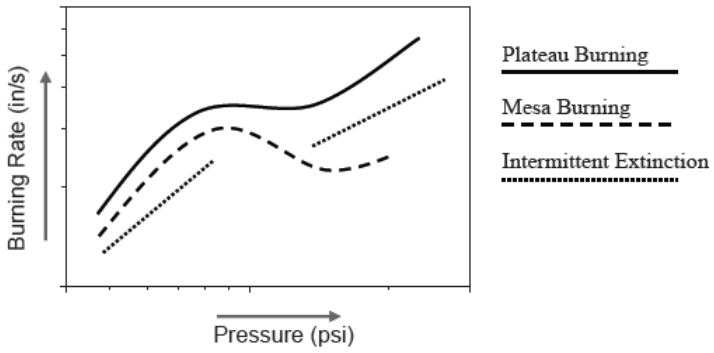

Figure 48: Illustration of various anomalous burning behavior types observed in research (Stephens et al., 2008). The model predictions in Figure 48 resemble the behaviors illustrated above.

The term, M_c, was applied to Equation 55, which governs the mass flux rate of the binder, and resulted in Equation 56. In Equations 55 and 56, m_{ox} is the mass flux rate of the oxidizer, and S is the surface area, such that S_{ox}/S_{binder} is a constant based on oxidizer and binder regression rates, AP particle size, mass loading, and modality. The term α is the percent mass loading of the AP and HTPB.

$$m_{binder} = m_{ox} \frac{S_{ox}}{S_{binder}} \frac{\alpha_{binder}}{\alpha_{ox}} \tag{55}$$

$$m_{binder} = m_{ox} \frac{S_{ox}}{S_{binder}} \frac{\alpha_{binder}}{\alpha_{ox}} M_c \tag{56}$$

Given that M_c, $\alpha_{binder}/\alpha_{ox}$, and S_{ox}/S_{binder} are constants, it can be seen that the binder mass flux is really the oxidizer mass flux multiplied by a single factor of some value.
To better understand the influence of M_c and what it possibly means physically, we can group $\alpha_{binder}/\alpha_{ox}$ and S_{ox}/S_{binder} as the constant, C. Equation 56 can then be rearranged to express the value of CM_c as the ratio of binder mass flux to oxidizer mass flux.

$$\frac{m_{binder}}{m_{ox}} = CM_c \tag{57}$$

Equation 57 implies that increasing M_c may not be representing binder mass flux increases, but may be mimicking an AP mass flux reduction, or a combination of both. This result is interesting because the change in perspective reflects a leading theory

regarding anomalous burning discussed in Stephens et al. (2008), and Handley and Strahle (1975), that additives can have a physical and/or chemical effect on the binder melt layer behavior. Anomalous trends are theorized to result from the binder melt layer underneath the surface flowing while the hot binder surface undergoes pyrolysis leading to smothering the AP crystal (Figure 49). If this occurs, the surface temperature of the AP would be negatively impacted by reduced heat transfer from the heat releases of the flames and vaporization back to the AP crystal surface. Consequently, the mass flux of the AP would be reduced and that would cause the quantity CM_c in Equation 57 to increase, which is similarly achieved by increasing the value of M_c, as seen in Figure 47, to obtain anomalous behavior.

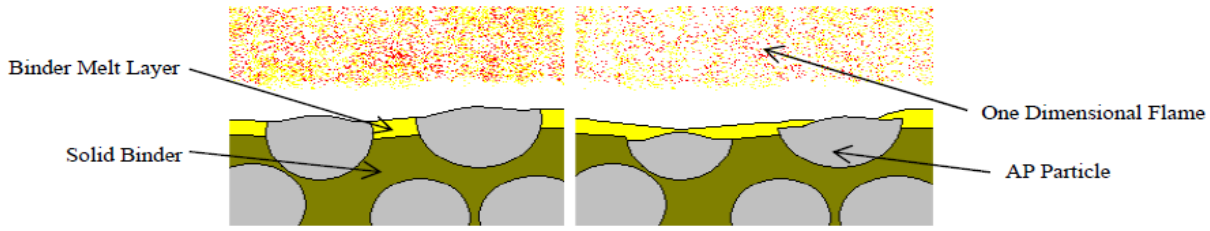

Figure 49: Illustration of the binder melt layer smothering an AP crystal (Stephens et al., 2008).

If M_c represents binder melt layer interaction slowing down AP mass flux, then it is most likely a constant defined by parameters that describe fluid flow such as temperature, pressure, geometry of the propellant surface (e.g. AP crystal height below or above the plane of the propellant surface), amount of binder mass flux that is lost to flow, and

various thermophysical properties that may change with pressure such as viscosity (Equation 58).

$$M_c = f\left(T_{binder}, P, \zeta, m_{binder,flow}, ..., \upsilon\right) \tag{58}$$

Finally, if M_c is related to binder melt layer dynamics, then Figure 47 indicates that, at lower pressures, melt layer dynamics have little to no effect on the burning rate as the burning rates at these increased binder-to-oxidizer mass flux ratios exhibit an increased burning rate compared to the baseline. This burning rate enhancement reinforces that pressure plays a role in M_c producing an anomalous effect because of pressure increases making a substance behave more like a fluid, such as the case with the binder melt layer theory.

Figure 50 shows the model's capability in mimicking a negative burning trend seen in the author's laboratory in recent experiments across the range of test pressures (500-2000 psi). M_c factor enhancements were combined with changing AP condensed phase kinetics to reflect an inhibited AP reaction rate due to possible binder melt flow and additive interference which results in desired similarities to experimental data. Factors of $M_c = 5$ and $\Omega_c = 0.1$ were used across the entire pressure range to achieve the negative trend. It should be re-emphasized that M_c is most likely a function of pressure, and Ω_c could change with pressure as well such that the two factors would vary in value to produce other behaviors that change slope (plateau/mesa) or result in no burning rate obtained (intermittent) at certain pressures as seen in Figure 48. The results in Figure 50

show that increased binder regression due to nanocatalytic activity does not yield the performance gains seen in laboratory experiments. However, it does indicate that changes to the mass flux ratio of binder to oxidizer (whether through slowed down AP mass flux, increased HTPB mass flux, or both) in tandem with changes to the AP condensed phase reaction rate may be responsible for certain anomalous behaviors. The changes to the model are in keeping with the analysis provided by Williams (2010) and binder melt layer theory as modifications made to the model are representative of changes to condensed-phase interactions.

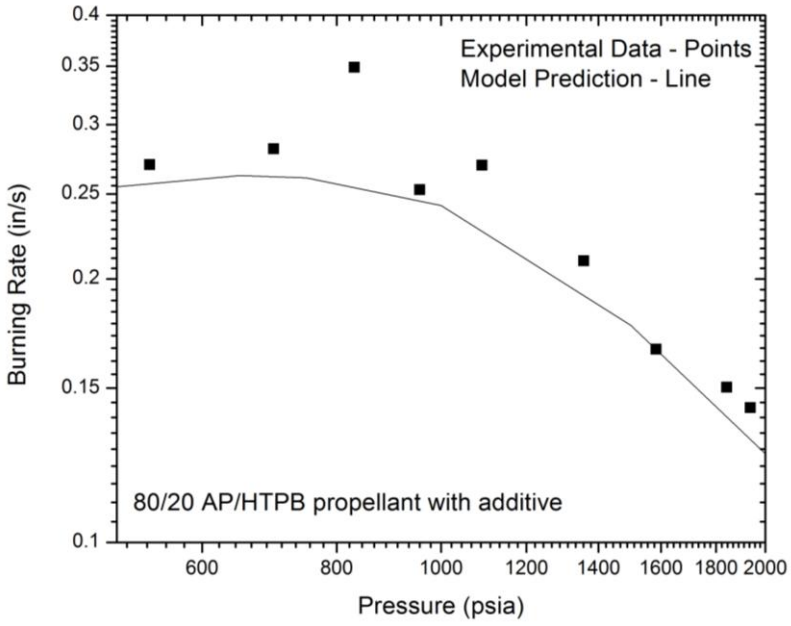

Figure 50: Model-predicted anomalous burning rates plotted with anomalous burning experiments from the author's laboratory. The model is shown to be capable of replicating anomalous burning behaviors. In this situation, the model used $M_c = 5$ and $\Omega_c = 0.1$ in tandem across the entire pressure range to replicate the anomalous behavior.

8. SUMMARY AND CONCLUSIONS

The model presented in this paper is capable of predicting a burning rate for a given baseline propellant formulation without additives within 15% of the experimental value. It has demonstrated the ability to accurately predict the correct burning rate exponent for a given propellant formulation as well. Also, a model that describes thermodynamic and ideal gas behaviors within the strand burner during an experiment has shown the ability to replicate a complete pressure trace to within 10% of the experiment. It also accurately predicts maximum pressure for a wide range of propellant mixtures across a wide range of pressures. The model is able to take an actual pressure trace and calculate an average burn rate and estimate the change in burning rate over time for an individual run.

An extensive parametric study has shown that nanoadditive experiments are reproduced by changes to the AP condensed phase kinetics, implying that nanoparticles are influencing the AP melt layer kinetics; particularly, they are enabling the AP to decompose with different reaction mechanisms that promote increased exothermicity, further heating the AP crystal, and increasing the burning rate. While it can not be confirmed by the model in its current state, it is suspected that an increase in the other decomposition mechanisms creates more species immediately available to react with HTPB pyrolysis products and possibly creates a premixed burning situation in the Primary Flame. The parametric study also produced correlations that were applied to the model to predict burning rates of nanoadditives in the author's laboratory.

There are further improvements to make and work to be done that would substantiate model findings and increase the model's capabilities. Accuracy of the strand burner and combustion models needs to be improved. A chemical kinetics model should be constructed and tested to support detailed chemical reactions in the Monopropellant and Primary Flames and to investigate the role of nanoparticles in gas-phase reactions, if any. The author suggests using CHEMKIN tools and set the foundation for the model by using the detailed reactions specified in Jeppson (1998) and Beckstead (2007). Finally, a chemical equilibrium analysis code will be integrated to make thermochemistry calculations inclusive within the model according to information published by McBride, et al. (2002).

To support future experiments, the model needs to predict the burning rates of aluminized propellants. Research by Swaminathan and Soosaimarian (1981), using a simplified BDP model would be a suitable first-approach, as their method for adding aluminized propellants is simple and follows the method already used in the BDP model to weight the contributions of oxidizer and binder mass flux to the overall burning rate by weighting the aluminum mass flux.

The model presented in this study is nearly all thermodynamics based so fluids relations are currently not captured in the model's calculations. However, knowing that the fluid mechanics of the binder and oxidizer melt layers can bring changes in surface interaction (melt layer dynamics) during propellant combustion, this aspect cannot be neglected for long. This component would be crucial to the estimation and determination of anomalous burning behavior, especially if melt layer dynamics play a significant role.

REFERENCES

Annamalai, K., and Puri, I. K. (2007) *Combustion Science and Engineering*. CRC Press, Boca Raton, FL.

Arvanetes, J. (2006) Design and Implementation of an Emission Spectroscopy Diagnostic in a High-Pressure Strand Burner for the Study of Solid Propellant Combustion. *MS Thesis, University of Central Florida*.

Bates, R., Davidson, D. F., Hanson, R. K., Petersen, E. L. (1998) Shock Tube Measurements of the Equation of State of Argon. *International Journal of Thermophysics,* **19**, 1585-1594.

Beckstead, M. W. (1977) A Model for Solid Propellant Combustion. *Hercules Incoporated,* 1977-0843U.

Beckstead, M. W., Derr, R. L., Price, C. F., (1970) A Model of Composite Solid Propellant Combustion Based on Multiple Flames. *AIAA Journal,* **8**, 2200-2207.

Beckstead, M. W., Puduppakkama, K., Thakreb, P., Yang, V. (2007) Modeling of Combustion and Ignition of Solid-propellant Ingredients. *Progress in Energy and Combustion Science*, **33**, 497–551.

Boggs, T. L., Zurn, D. E., Cordes, H. F., and Covino, J. (1988) Combustion of Ammonium Perchlorate with Various Inorganic Additives. *Journal of Propulsion and Power*, **4**, 27-40.

Borgnakke, T., Sonntag, R. (2007) *Fundamentals of Thermodynamics*. Wiley, New York.

Brill, T. B., Budenz, B. T. (2000) Flash Pyrolysis of Ammonium Perchlorate – Hydroxyl-Terminated-Polybutadiene Mixtures Including Selected Additives. *Progress in Astronautics and Aeronautics,* **185**, 3-30.

Browne, H. N., Jr., Williams, M. W., Cruise, D. R. (1960) The Theoretical Computation of Equilibrium Compositions, Thermodynamic Properties and Performance Characteristics of Propellant Systems. *NOTS-TP-2434, NAVWEPS Report 7043*.

Burmeister, Louis C. (1993) *Convective Heat Transfer*, Wiley, New York.

Cai, W., Thakre, P., Yang, V. (2008) A Model of AP/HTPB Composite Propellant Combustion in Rocket-Motor Environments. *Combust. Sci. and Tech.,* **180**, 2143-2169.

Carro, R. (2007) High Pressure Testing of Composite Solid Rocket Propellant Mixtures: Burner Facility Characterization. *MS Thesis, University of Central Florida*.

Chakravarthy, S. R., Price, E. W., and Sigman, R. K. (1997) Mechanism of Burning Rate Enhancement of Composite Solid Propellants by Ferric Oxide. *Journal of Propulsion and Power*, **13**, 471-480.

Cohen, Norman S. (1980) Review of Composite Propellant Burn Rate Modeling. *AIAA Journal*, **18**, 277-293.

Cohen, N., Strand, L. (1982) An Improved Model for the Combustion of AP Composite Propellants. *AIAA Journal,* **20**, 1739-1746.

Cruise, D. R., (1979) Theoretical Computations of Equilibrium Composition, Thermodynamic Properties, and Performance Characteristics of Propellant Systems. *Naval Weapons Center, NWC-TP-6037*.

Condon, J. A., Renie, J. P., Osborn, J. R. (1977) Temperature Sensitivity of Propellant Burning Rates. *Combustion and Flame,* **30**, 267-276.

DeWitt, J. and Incropera, F. (2001) *Fundamentals of Heat and Mass Transfer*. Wiley, New York.

Fox, R. W. and McDonald, A. T. (1998) *Introduction to Fluid Mechanics*. Wiley, New York.

Fong, C. W., and Hamshere, B. L. (1986) The Mechanism of Burning Rate Catalysis in Composite HTPB—AP Propellant Combustion. *Combustion and Flame*, **65**, 61-69.

Fong, C. W., and Hamshere, B. L. (1986) The Mechanism of Burning Rate Catalysis in Composite Propellants by Transition Metal Complexes. *Combustion and Flame*, **65**, 71-78.

Frazier, C. A., Lamnaouer, M., Petersen, E. L., Divo, E., Kassab, A. (2011) Effect of Wall Heat Transfer on Shock-Tube Test Temperature at Long Times. *International Journal on Shock Waves, Detonations, and Explosions,* **21**, 1-17.

Glassman, Irvin (1996) *Combustion,* Academic Press, San Diego.

Glick, R., Haun, D. (1990) An Improved Closed Burner Method. *26th Joint Propulsion Conference, AIAA*, 90-1870.

Gross, M. L., Beckstead, M. W. (2009) Diffusion Flame Calculations for Composite Propellants Using a Vorticity-Velocity Formulation. *Journal of Propulsion and Power,* **25**, 74-82.

Gross, M. L., Beckstead, M. W. (2011) Steady-State Combustion Mechanisms of Ammonium Perchlorate Composite Propellants. *Journal of Propulsion and Power*, **27**, 1064-1078.

Guirao, C., Williams, F.A. (1971) A Model for Aluminum Perchlorate Deflagration Between 20 and 100 atm. *AIAA Journal*, **9**, 1345-1356.

Handley, J. C., and Strahle, W. C. (1975) Behavior of Several Catalysts in the Combustion of Solid Propellant Sandwiches. *AIAA Journal,* **13**(1), 5-6.

Jeppson, M.B., Beckstead, M. W., Jing, Q. (1998) A Kinetic Model for the Premixed Combustion of a Fine AP/HTPB Composite Propellant. *AIAA Journal*, **44**(7), 1-12.

Jones, H. E., and Strahle, W. C. (1973) Effects of Copper Chromite and Iron Oxide Catalysts on AP/CTPB Sandwiches. *Proceedings of the 14th Symposium (International) on Combustion, The Combustion Inst.,* 1287-1295.

Jung, T. Y. and Yoh, J. J. (2010) Model for Melt-Layer Front in Ammonium Perchlorate Propellant Combustion. *Journal of Propulsion and Power,* **26**(5), 993-997.

Kee, R. J., Miller, J. A., Rupley, F. M. (1990) The Chemkin Thermodynamic Database. *Sandia Report, SAND87-8215B.*

Kishore, K., and Sunitha, M. R. (1978) Mechanism of Catalytic Activity of Transition Metal Oxides on Solid Propellant Burning Rate. *Combustion and Flame,* **33**, 311-314.

Korobeinichev, O. P., Anisiforov, G. I., and Tereschenko, A. G. (1975) High-Temperature Decomposition of Ammonium Perchlorate-Polystyrene-Catalyst Mixtures. *AIAA Journal,* **13**(5), 628-633.

Korobeinichev, O. P., Kovalenko, K. K., and Lesnikovich, A. I. (1978) *Investigation of Effect of Oxide and Organometallic Catalysts on Thermal Decomposition and Combustion of a Model Ammonium Perchlorate-Polymer System*. Plenum, New York.

Korobeinichev, O. P., Ermolin, N. E., Chernov, A. A., and Emel'yanov, I. D. (1992) Flame Structure, Kinetics and Mechanisms of Chemical Reactions in Flames of Mixed Composition Based on Ammonium Perchlorate and Polybutadiene Rubber. *Combustion, Explosion, and Shock Waves*, **28**(4), 53-59.

Kreitz, K. R. (2010) Catalytic Nanoparticle Additives in the Combustion of AP/HTPB Composite Solid Propellant, *MS Thesis, Texas A&M University*.

Kreitz, K. R., Petersen, E. L., Reid, D. L., Seal, S. (2011) Relative Dispersion of Catalytic Nanoparticle Additives and AP Particles in Composite Solid Propellant and the Effect on Burning Rate. *49th AIAA Aerospace Sciences Meeting including the New Horizons Forum and Aerospace Exposition, AIAA*, 2011-418.

Kreitz, K., Reid, D., Seal, S., Petersen, E. (2011) Scale-up Effects of Nanoparticle Production on the Burning Rate of Composite Propellant. *Combustion Science and Technology (in press).*

Krishnan, S., and Jeenu, R. (1990) Subatmospheric Burning Characteristics of AP/CTPB Composite Propellants with Burning Rate Modifiers. *Combustion and Flame*, **80**, 1-6.

Krishnan, S., and Jeenu, R. (1992) Combustion Characteristics of AP/HTPB Propellants with Burning Rate Modifier. *Journal of Propulsion and Power*, **8**(4), 748-755.

Krishnan, S., and Periasamy, C. (1986) Low-Pressure Burning of Catalyzed Composite Propellants. *AIAA Journal*, **24**(10), 1670-1675.

Massa, L., Jackson, T. L., Buckmaster, J. (1998) A Kinetic Model for the Premtxed Combustion of a Fine AP/HTPB Composite Propellant. *Journal of Propulsion and Power*, **21**, 914-924.

McBride, B., Zehe, M., Gordon, S. (2002) NASA Glenn Coefficients for Calculating Thermodynamic Properties of Individual Species. *NASA, TP-2002-211556*.

Ozisik, M. N. (1993) *Heat Conduction*, Wiley, New York.

Pearson, G. S. (1971) The Role of Catalysts in the Ignition and Combustion of Solid Propellants. *Combustion Science and Technology*, **3**, 155-163.

Pittman, C. U., Jr. (1969) Location of Action of Burning-Rate Catalysts in Composite Propellant Combustion. *AIAA Journal*, **7**(2), 328-334.

Price, C.F., Boggs, T.L., and Derr, R.L. (1979) The Steady-State Combustion Behavior of Ammonium Perchlorate and HMX. *17th Aerospace Sciences Meeting, AIAA,* 79-0164.

Rasmussen, B., Frederick, R. A., Jr. (2002) Nonlinear Heterogeneous Model of Composite Solid-Propellant Combustion. *Journal of Propulsion and Power,* **18**, 1086-1092.

Reid, D. L., Russo, A. E., Carro, R. V., Stephens, M. A., LePage, A. R., Spalding, T. C., Petersen, E. L., Seal, S. (2007) Nanoscale Additives Tailor Energetic Materials. *Nano Letters,* **7**, 2157-2161.

Reid, D. L., Kreitz, K. R., Stephens, M. A., King, J. E. S., Nachimuthu, P., Petersen, E. L., Seal, S. (2011) Development of Highly Active Titania-Based Nanoparticles for Energetic Materials. *Journal of Physical Chemistry,* **115**, 10412-10418.

Shusser, M., Culick, F., Cohen, N. (2002) Combustion Response of Ammonium Perchlorate. *AIAA Journal,* **40**, 722-730.

Singh, G, Kapoor, I. P. S., Dubey, S. (2009) Kinetics of Thermal Decomposition of Ammonium Perchlorate with Nanocrystals of Binary Transition Metal Ferrites. *Propellants, Explosives, Pyrotechnics*, **34**, 72-77.

Stephens, M. A., Petersen, E. L. (2007) Addition Methods of Nanoscale Additives in Solid Composite Propellants. *AIAA Region II Student Conference, AIAA,* 90-1870.

Stephens, M. A., Sammet, T., Carro, R. V., LePage, A., Petersen, E. L. (2007) Comparison of Hand and Mechanically Mixed AP/HTPB Solid Composite Propellants. *43rd AIAA/ASME/SAE/ASEE Joint Propulsion Conference & Exhibit, AIAA,* 2007-5765.

Stephens, M. A., Petersen, E. L., Reid, D. L., Carro, R. V., Seal, S. (2008) Nano Additives and Plateau Burning Rates in Composite Solid Propellants. *44th AIAA/ASME/SAE/ASEE Joint Propulsion Conference & Exhibit, AIAA*, 2008-4790.

Sutton, G., Biblarz, O. (2001) *Rocket Propulsion Elements*, Wiley, New York.

Swaminathan, V., Soosaimarian, M. (1981) Burning Rate Evaluation of Composite Solid Propellants. A Simplified Approach. *Propellants and Explosives,* **6**, 37-41.

Villars, D. S. (1959) A Method of Successive Approximations for Computing Combustion Equilibria on a High Speed Digital Computer. *Journal of Physical Chemistry*, **63**(4), 521-525.

White, Frank M. (1991) *Viscous Fluid Flow*. McGraw-Hill, Boston.

Williams, Forman, A. (2010) *Combustion Theory*. Perseus Books, Reading.

Yilmaz, N., Donaldson, B., Gill, W., Erikson, W. (2008) Solid Propellant Burning Rate from Strand Burner Pressure Measurement. *Propellants, Explosives, Pyrotechnics,* **33**, 109-117.

APPENDIX A

AP/HTPB KINETICS MECHANISMS FROM JEPPSON ET AL. (1998)

Table 3. Semi-global mechanism for the two phase (condensed) region.

Reaction	A	b	E_A
1. HTPB1200(C)=>2HTPB580(C)+3C(S)+H2	1.00E+10	0.0	10000
2. HTPB580(C)=>10C4H6+C2H3+CH3	2.00E+11	0.0	10000
3. HTPB580(C)+15AP(C)=>20CO+10HCN+13CH4+32H2O+8CLO+7CL+5N	3.20E+11	0.0	10000
4. HTPB580(C)+20HCLO4=>8CO+24CO2+24H2O+20HCL+5C2H2+CH4+2H2	1.00E+12	0.0	10000
5. AP(C)=>NH3+HCLO4	8.00E+12	0.0	28000
6. AP(C)=>H2O+O2+HCL+HNO	1.00E+08	0.0	22000
7. AP(C)=>2H2O+CL+NO2	5.00E+07	0.0	22000
8. AP(C)=>CLO3+NH3+OH	1.00E+09	0.0	22000

Note. $k=AT^b\exp(-E_A/RT)$; units for A, b, E_A: cal, mole, sec, cm^3, K.

GAS PHASE KINETIC MECHANISM

Reaction	A	b	E_A
1. HCLO4=CLO3+OH	1.00E+14	0.00	39100.0
2. HCLO4+HNO=CLO3+NO+H2O	3.00E+13	0.00	6000.0
3. HCLO4+HCO=CLO3+CO+H2O	5.00E+13	0.00	0.0
4. HCLO4+HCO=CLO2+CO2+H2O	1.50E+12	0.00	0.0
5. CLO3=CLO+O2	1.70E+15	0.50	0.0
6. CL2+O2+M=CLO2+CL+M	6.00E+08	0.00	11200.0
7. CLO+NO=CL+NO2	6.80E+12	0.00	311.0
8. CLOH+CLO=CL2+HO2	1.00E+14	0.00	10000.0
9. CLOH+OH=CLO+H2O	1.80E+13	0.00	0.0
10. HCL+OH=CL+H2O	5.00E+11	0.00	750.0
11. CL2+H=HCL+CL	8.40E+13	0.00	1150.0
12. NH3+CLO=NH2+CLOH	4.24E+11	0.50	6400.0
13. NH3+CL=NH2+HCL	4.50E+11	0.50	100.0
14. NH3+OH=NH2+H2O	5.00E+07	1.60	955.0
15. NH2+O2=HNO+OH	6.00E+09	0.50	0.0
16. NH2+NO=N2+H2O	2.40E+11	0.00	0.0
17. NH2+NO=NNH+OH	6.00E+11	0.00	0.0
18. NNH+NO=HNO+N2	5.00E+13	0.00	0.0
19. HNO+OH=NO+H2O	1.30E+07	1.90	-950.0
20. HNO+O2=NO2+OH	1.00E+13	0.00	10000.0
21. HNO+H=H2+NO	4.50E+11	0.72	660.0
*22. NO+H+M=HNO+M	8.90E+19	-1.32	740.0
23. N2+HO2=HNO+NO	8.00E+10	0.50	41800.0
24. NO+HO2=NO2+OH	2.11E+12	0.00	480.0
25. NO2+H=NO+OH	5.00E+14	0.00	1740.0
26. H2+OH=H2O+H	2.16E+08	1.51	3430.0
27. CH2CO+OH=CH2O+HCO	2.82E+14	0.00	0.0
28. CH2CO+NO2=CH2O+CO+NO	1.00E+13	0.00	6000.0
29. C2H3+O2=CH2O+HCO	3.98E+12	0.00	-240.0
*30. C2H2+H(+M)=C2H3(+M)	5.60E+12	0.00	2400.0
31. C2H2+OH=CH3+CO	4.84E-04	4.00	-2000.0
*32. H2+CO(+M)<=>CH2O(+M)	4.30E+07	1.50	79600.0
33. CH4+CL=CH3+HCL	2.50E+13	0.00	3830.0
34. CH4+CLO=CH3+CLOH	6.00E+11	0.50	5700.0
35. CH4+H=CH3+H2	6.60E+08	1.62	10840.0
36. CH4+OH=CH3+H2O	1.00E+08	1.60	3120.0

Reaction	A	b	E_A
*37. CH3+H(+M)=CH4(+M)	1.27E+16	-0.63	383.0
*38. HCO+M=CO+H+M	1.87E+17	-1.00	17000.0
39. HCN+OH=NH2+CO	1.62E+02	2.56	9000.0
40. CO+OH=CO2+H	4.76E+07	1.23	70.0
41. CO+CLO=CO2+CL	3.00E+12	0.00	1000.0
42. CO+CLO2=CO2+CLO	1.00E+10	0.00	0.0
43. C2H4+OH=H2O+C2H3	3.60E+06	2.00	2500.0
44. C4H6+OH=2C2H2+H2O+H	5.00E+12	0.68	1100.0
45. C4H6+CLO=2C2H2+CLOH+H	5.00E+12	0.50	6400.0
46. C4H6+CL=2C2H2+HCL+H	6.75E+12	0.50	100.0
47. H+O2=O+OH	8.30E+13	0.00	14413.0
48. C2H2+O=CH2+CO	1.02E+07	2.00	1900.0
49. CH2+H2=CH3+H	5.00E+05	2.00	7230.0
*50. CH2+H(+M)=CH3(+M)	2.50E+16	-0.80	0.0
51. CH4+O=CH3+OH	1.02E+09	1.50	600.0
52. CH3+O=CH2O+H	8.43E+13	0.00	0.0
53. CH2+O=H+HCO	8.00E+13	0.00	0.0
54. CH3+O2=OH+CH2O	3.60E+10	0.00	8940.0
55. OH+CH3=CH2+H2O	5.60E+07	1.60	5420.0
56. OH+CH2=H+CH2O	2.00E+13	0.00	0.0
57. CH2+O2=OH+HCO	1.32E+13	0.00	1500.0
58. C2H4+O2=2CO+2H2	1.80E+14	0.00	35500.0
59. O2+HNO=NO+HO2	1.00E+13	0.00	13000.0
60. NH2+NO2=2HNO	2.00E+12	0.00	0.0
61. NH2+CLO=HNO+HCL	2.50E+12	0.00	0.0
*62. H+CL+M=HCL+M	5.30E+21	-2.00	-2000.0
*63. CL+HO2=CLO+OH	2.47E+13	0.00	894.0
64. CLO+O=CL+O2	9.70E+12	0.00	507.0
65. HCL+H=H2+CL	2.30E+13	0.00	3500.0
66. HCL+O=OH+CL	5.24E+12	0.00	6400.0
67. CL2+O=CL+CLO	2.51E+12	0.00	2720.0
*68. N2O(+M)=N2+O(+M)	6.20E+14	0.00	56100.0
69. N2O+OH=N2+HO2	2.00E+12	0.00	21060.0
70. N2O+O=NO+NO	2.90E+13	0.00	23150.0
71. N2O+O=N2+O2	1.40E+12	0.00	10810.0
72. N2O+H=N2+OH	4.40E+14	0.00	18880.0

Note. $k=AT^b\exp(-E_A/RT)$; units for A, b, E_A: cal, mole, sec, cm^3, K. *Reaction includes pressure dependence parameters.

APPENDIX B

SAMPLE MATHCAD SPREADSHEET OF STRAND BURNER PRESSURE TRACE MODEL

Burning Model V5.0 4/15/2010 Thermobuild Data PROPEP Data Manual Input Burn Log Data

$P_{initial} := 1194.3 \cdot \left(\frac{101300}{14.7}\right)$ $P_{final\_actual} := 1329.7$ //initial and final pressures within the strand bomb in psi, the initial is converted to Pa for calculations

$T_{initial} := 300$ //initial temperature within the strand bomb in K

$L_{SB} := 6.5$ $L_{plum} := 331$ //strand bomb length in in, length of plumbing in in

$d_{SB} := 3.7$ $d_{plum} := 0.25 - 0.065$ //strand bomb diameter in in, inner diameter of plumbing in in

$V_{SB} := \pi \cdot \frac{d_{SB}^2}{4} \cdot L_{SB} \cdot \left(\frac{1}{39.37^3}\right)$ //volume of strand bomb in in³ (from drawings), converted to m³, **assumes window endcaps and bolt are negligible. VSB_new** is volume of the plumbing, strand bomb (via water measurement), minus the strand volume

$V_{SB\_new} := \frac{1.35744}{1000} + \pi \cdot \frac{d_{plum}^2}{4} \cdot L_{plum} \cdot \left(\frac{1}{39.37^3}\right) - \pi \cdot \frac{d_{strand}^2}{4} \cdot L_{strand}$

Propellant Characteristics NTB02-05

$BR := 0.226 \cdot \left(\frac{1}{39.37}\right)$ //Propellant burn rate in in/s converted to m/s

$L_{strand} := 0.967 \cdot \left(\frac{1}{39.37}\right)$ //Propellant strand length in in converted to m

$d_{strand} := 0.1875 \cdot \left(\frac{1}{39.37}\right)$ //strand diameter in in, converted to m

$m_{strand} := 0.00065$ //strand mass in kg

$\rho_{strand} := \frac{m_{strand}}{\pi \cdot \frac{d_{strand}^2}{4} \cdot L_{strand}}$ $\pi \cdot \frac{d_{strand}^2}{4} \cdot L_{strand} = 0.00000044$ //strand density in kg/m³

$mdot\_in := BR \cdot \left(\pi \cdot \frac{d_{strand}^2}{4}\right) \cdot \rho_{strand}$ //mass flow rate of the products entering the system in kg/s

PROPEP / Periodic Table / Thermobuild (cea.grc.nasa.gov) Data:

$k := 0, 1 .. 11$ $m := 11$ //k and m are counters for the summation functions based on array/matrix size

$PROPEP\_moles := \begin{pmatrix} 0.01316 \\ 0.01259 \\ 0.00387 \\ 0.00201 \\ 0.00175 \\ 0.0007 \\ 0.000672 \\ 0 \\ 0 \\ 0 \\ 0 \end{pmatrix} \cdot 10^{-3}$ $MW := \begin{pmatrix} 2 \\ 28 \\ 36.453 \\ 28 \\ 18 \\ 44 \\ 16 \\ 17 \\ 27 \\ 30 \\ 28 \end{pmatrix}$ $Cp\_species := \begin{pmatrix} 32.104 \\ 35.081 \\ 33.917 \\ 34.698 \\ 46.825 \\ 58.120 \\ 89.627 \\ 0 \\ 0 \\ 0 \\ 0 \end{pmatrix}$ $H\_species := \begin{pmatrix} 34.806 \\ 37.229 \\ 35.958 \\ 36.805 \\ 46.041 \\ 59.03 \\ 76.035 \\ 0 \\ 0 \\ 0 \\ 0 \end{pmatrix}$

$MW_{PROPEP} := 18.699$ //MW prod in kg/kmol or g/mol

$T_{AF\_PROPEP} := 1454$ //TAF of products entering system in K, found from PROPEP calculations

$PROPEP\_moles_{tot} := 0.0348 \cdot 10^{-3}$ //total number of kmoles of prop gas from PROPEP

$mass_k := PROPEP\_moles_k \cdot MW_k$ //computed mass of each species

$mass_{prod} := MW_{PROPEP} \cdot PROPEP\_moles_{tot}$ //computed total mass of the propellant gas mixture

$X_k := \frac{mass_k}{mass_{prod}}$ $Y_k := \frac{PROPEP\_moles_k}{PROPEP\_moles_{tot}}$ //X is the mass fraction of each species, Y is the mole fraction

Adiabatic Pressure Calculations

Test time and Time Step Counters:

$t_{test} := \frac{L_{strand}}{BR}$ $n := 300$ $i := 0, 1 .. n$ $\Delta t := \frac{t_{test}}{n}$ $tt_i := (i) \cdot \Delta t$ //n is the number of time steps, i is a counter from 0 to n, Δt discretizes how much time changes per step, and tt tracks at what time step the calculation is performed, such that when i=n, tt = total test time

$T_{SB}(tt) := \frac{H\_PROP \cdot mdot\_in \cdot tt + (Cp\_Ar - R_{Argon}) \cdot m_{initial} \cdot T_{initial}}{m\_SB(tt) \cdot Cv\_mix(tt)}$ //total system adiabatic temperature at each time step via COE for transient process

$\Delta T(tt) := T_{SB}(tt) - T_{initial}$ //total change in adiabatic system temperature at each time step

$P_{SB}(tt) := \frac{m\_SB(tt)}{V_{SB}} \cdot \frac{Ru}{MW_{mix}(tt)} \cdot T_{SB}(tt)$ //adiabatic pressure at every time step via ideal gas law

$\Delta P(tt) := P_{SB}(tt) - P_{initial}$ //total change in system adiabatic pressure at each time step

Calculating the masses, mixture properties, temperature, and pressure of the system at each time step:

$m\_SB(tt) := m_{initial} + mdot\_in \cdot tt$ //COM: mass of system is the initial mass + the mass at every time step

$Moles_{Ar} := \frac{m_{Argon}}{MW_{Ar}}$ //find the number of moles of Argon present (constant)

$Moles_{prod}(tt) := \frac{PROPEP\_moles_{tot}}{t_{test}} \cdot tt$ //find the number of moles of the products present in the system at each time step

$Moles_{total}(tt) := Moles_{Ar} + Moles_{prod}(tt)$ //the total number of moles in the mixture (prop & Ar) at each time step

$Y_{Ar}(tt) := \frac{Moles_{Ar}}{Moles_{total}(tt)}$ $X_{Ar}(tt) := \frac{m_{initial}}{m\_SB(tt)}$ //calculate the mole and mass fraction of Argon in the mixture at each time step

$Y_{prod}(tt) := \frac{Moles_{prod}(tt)}{Moles_{total}(tt)}$ $X_{prod}(tt) := \frac{mdot\_in \cdot tt}{m\_SB(tt)}$ //calculate the mole and mass fraction of the products in the mixture at each time step

$MW_{mix}(tt) := Y_{Ar}(tt) \cdot MW_{Ar} + Y_{prod}(tt) \cdot MW_{PROPEP}$ //calculate the molecular weight of the mixture at each time step.

$Cp\_min(tt) := Cp\_Ar \cdot X_{Ar}(tt) + Cp\_PROP \cdot X_{prod}(tt)$ //Find Cp of mixture at each time step (cp in J/kg K * mass fraction)

Plot the Pressure Trace during the test time:

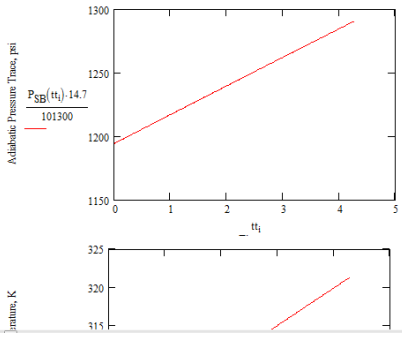

Heat Transfer Calculations

1. Solution for Conduction and Convection, During-Test:

$P_{end} := P_{SB}(t_{test})$ //pressure in the system at test end in Pa

$Tend := T_{SB}(t_{test})$ $T_{ambient} := T_{initial}$ //temperature in the system at test end and ambient in K

$k_{mix}(tt) := .0163 \cdot \left(\frac{T_{SB}(tt)}{273}\right)^{\frac{3}{2}} \cdot \frac{273 + 170}{T_{SB}(tt) + 170}$ $k1 := k_{mix}$ //thermal conductivity of the mixture (effectively Argon), in W/mK **(how do we approx entire mixture?)**

$\rho_{mix}(tt) := \frac{P_{SB}(tt)}{(Cp\_mix(tt) - Cv\_mix(tt)) \cdot Tend}$ //density of the mixture, in kg/m^3

$\alpha_{mix}(tt) := \frac{k_{mix}(tt)}{\rho_{mix}(tt) \cdot Cp\_mix(tt)}$ $\alpha 1 := \alpha_{mix}$ //thermal conductivity of the mixture, in m^2/s

---

$T\_interface(tt) := To(tt) \cdot \left(\frac{k1(tt) \cdot \sqrt{\alpha 2}}{k1(tt) \cdot \sqrt{\alpha 2} + k2 \cdot \sqrt{\alpha 1(tt)}}\right)$

Interface temperature (T_i) between Argon gas and stainless steel wall with a 1D Cartesian model in K

$T\_i(tt) := T_{ambient} + T\_interface(tt)$

$T_{surface} := T_{initial}$ $A_s := 2 \cdot \pi \cdot (d_{SB})^2 \cdot \frac{1}{39.37^2} + 2 \cdot \pi \cdot \left(\frac{d_{SB}}{2}\right) \cdot L_{SB} \cdot \frac{1}{39.37^2}$ $A_s = 0.15298573$ $thick := 1.15 \cdot \frac{1}{39.37}$ $h := 5$

$T\_test\_cond\_ht(tt) := \frac{k_{mix}(tt) \cdot A_s}{thick \cdot Cv\_mix(tt) \cdot m\_SB(tt)} \cdot tt \cdot (T_{surface} - T_{SB}(tt)) + T_{SB}(tt)$

$P\_test\_cond\_ht(tt) := \frac{m\_SB(tt)}{V_{SB}} \cdot \frac{Ru}{MW_{mix}(tt)} \cdot (T\_test\_cond\_ht(tt))$

$\Delta P\_test\_cond\_ht(tt) := P_{SB}(tt) - P\_test\_cond\_ht(tt)$

1. Post-Test Heat Transfer Calcs: Convection HT via Yilmaz Newton's Law of Cooling Equation:

$Tend := T\_test\_total\_ht(t_{test})$

$k_{mix} := .0163 \cdot \left(\frac{Tend}{273}\right)^{\frac{3}{2}} \cdot \frac{273 + 170}{Tend + 170}$ $k_{mix} = 0.0186872$ $k1 := k_{mix}$ //thermal conductivity of the mixture (effectively Argon), in W/mK **(how do we approx entire mixture?)**

$\rho_{mix} := \frac{P_{end}}{(Cp\_mix(t_{test}) - Cv\_mix(t_{test})) \cdot Tend}$ $\rho_{mix} = 133.03656205$ //densty of the mixture, in kg/m^3

$\alpha_{mix} := \frac{k_{mix}}{\rho_{mix} \cdot Cp\_mix(t_{test})}$ $\alpha 1 := \alpha_{mix}$ $\alpha_{mix} = 0.00000027$ //thermal conductivity of the mixture, in m^2/s

$To := Tend - T_{ambient}$ $To = 19.71128665$

$T\_post\_test\_total\_ht_q :=$
- $T_{surface} \leftarrow T_{initial}$
- $T\_post\_test\_total\_ht_1 \leftarrow T\_test\_total\_ht(t_{test})$
- for $q \in 1, 2 .. nnn$
  - $k_{mix} \leftarrow .0163 \cdot \left(\frac{T\_post\_test\_total\_ht_q}{273}\right)^{\frac{3}{2}} \cdot \frac{273 + 170}{T\_post\_test\_total\_ht_q + 170}$
  - $Ppost\_test\_total\_ht_q \leftarrow \frac{m\_SB(t_{test})}{V_{SB}} \cdot \frac{Ru}{MW_{mix}(t_{test})} \cdot T\_post\_test\_total\_ht_q$
  - $\rho_{mix} \leftarrow \frac{Ppost\_test\_total\_ht_q}{(Cp\_mix(t_{test}) - Cv\_mix(t_{test})) \cdot T\_post\_test\_total\_ht_q}$
  - $\alpha_{mix} \leftarrow \frac{k_{mix}}{\rho_{mix} \cdot Cp\_mix(t_{test})}$

Combined Heat Transfer Effects:

$T\_test\_total\_ht(tt) := T_{SB}(tt) - \Delta T\_test\_cond\_ht(tt) - \Delta T\_test\_conv\_ht(tt)$

$P\_test\_total\_ht(tt) := \frac{m\_SB(tt)}{V_{SB}} \cdot \frac{Ru}{MW_{mix}(tt)} \cdot T\_test\_total\_ht(tt)$

$\Delta P\_test\_total\_ht(tt) := \Delta P\_test\_cond\_ht(tt) + \Delta P\_test\_conv\_ht(tt)$

$\Delta T\_test\_total\_ht(tt) := \Delta T\_test\_cond\_ht(tt) + \Delta T\_test\_conv\_ht(tt)$

$P_{end\_total\_ht} := P\_test\_total\_ht(t_{test})$ $P_{end\_total\_ht} \cdot \frac{14.7}{101300} = 1284.48537162$

$P\_test\_total\_ht(tt_i) \cdot \frac{14.7}{101300}$	$\Delta P\_test\_total\_ht(tt_i) \cdot \frac{14.7}{101300}$	$\Delta T\_test\_total\_ht(tt_i)$	$T\_test\_total\_ht(tt_i) =$
1194.3	0	0	300
1194.62493608	0.00007483	0.0000188	300.07241535
1194.94970118	0.00029928	0.00007517	300.14478332
1195.27429541	0.00067324	0.0001691	300.21710392
1195.59871884	0.00119666	0.00030056	

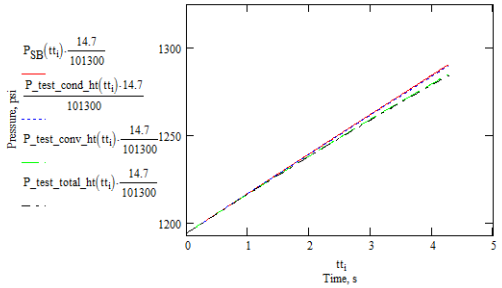

Condensation Analysis

$PH2O_q := \left(\frac{0.00175 \cdot 10^{-3}}{Moles_{total}(t_{test})}\right) \cdot Ppost\_test\_total\_ht_q$ $mass\_H2O := \frac{PROPEP\_moles_4 \cdot MW_4}{1000}$

$\Delta T\_H2O_q := \frac{T\_H2O\_300}{t_{equilib}} \cdot ttt_q$

$Ppost\_test\_total\_ht_q \cdot \frac{14.7}{101300} - PH2O_q \cdot \frac{14.7}{101300}$
1283.89596219
1281.09659112
1278.39876932

$PH2O_q \cdot \frac{14.7}{101300}$
0.58940943
0.5881243
0.58688578

$H\_PROP\_H2O := \frac{H\_species_4}{MW_4} \cdot X_4 \cdot 1000000 - \frac{(0.139)}{MW_4} \cdot X_4 \cdot 1000000$

$\Delta T\_H2O_q =$
0.09894999
0.19789998
0.29684997
0.39579996

$T\_H2O = 980.28830753$

$H\_PROP\_H2O = 123444.$

$T\_post\_test\_total\_ht\_conden_q :=$
- $T_{surface} \leftarrow T_{initial}$
- $T\_post\_test\_total\_ht\_conden_1 \leftarrow T\_test\_total\_ht(t_{test})$
- for $q \in 1, 2 .. nnn$
  - $k_{mix} \leftarrow .0163 \cdot \left(\frac{T\_post\_test\_total\_ht\_conden_q}{273}\right)^{\frac{3}{2}} \cdot \frac{273 + 170}{T\_post\_test\_total\_ht\_conden_q + 170}$
  - $Ppost\_test\_total\_ht_q \leftarrow \left(\frac{m\_SB(t_{test})}{V_{SB}} \cdot \frac{Ru}{MW_{mix}(t_{test})} \cdot T\_post\_test\_total\_ht\_conden_q\right) - PH2O_q$
  - $\rho_{mix} \leftarrow \frac{Ppost\_test\_total\_ht_q}{(Cp\_mix(t_{test}) - Cv\_mix(t_{test})) \cdot T\_post\_test\_total\_ht\_conden_q}$
  - $\alpha_{mix} \leftarrow \frac{k_{mix}}{\rho_{mix} \cdot Cp\_mix(t_{test})}$
  - $T\_interface \leftarrow To \cdot \left(\frac{k_{mix} \cdot \sqrt{\alpha 2}}{k_{mix} \cdot \sqrt{\alpha 2} + k2 \cdot \sqrt{\alpha_{mix}}}\right)$
  - $T\_i \leftarrow T_{surface} + T\_interface$
  - $T\_test\_cond\_ht_q \leftarrow \left[\frac{k_{mix} \cdot A_s}{thick \cdot (Cv\_mix(t_{test}) \cdot m\_SB(t_{test}))} \cdot ttt_q\right] \cdot (T\_i - T\_post\_test\_total\_ht\_conden_q) + T\_post\_test\_total\_ht\_conden_q$

APPENDIX C

SAMPLE MATHCAD SPREADSHEET OF STRAND BURNER BURNING RATE MODEL

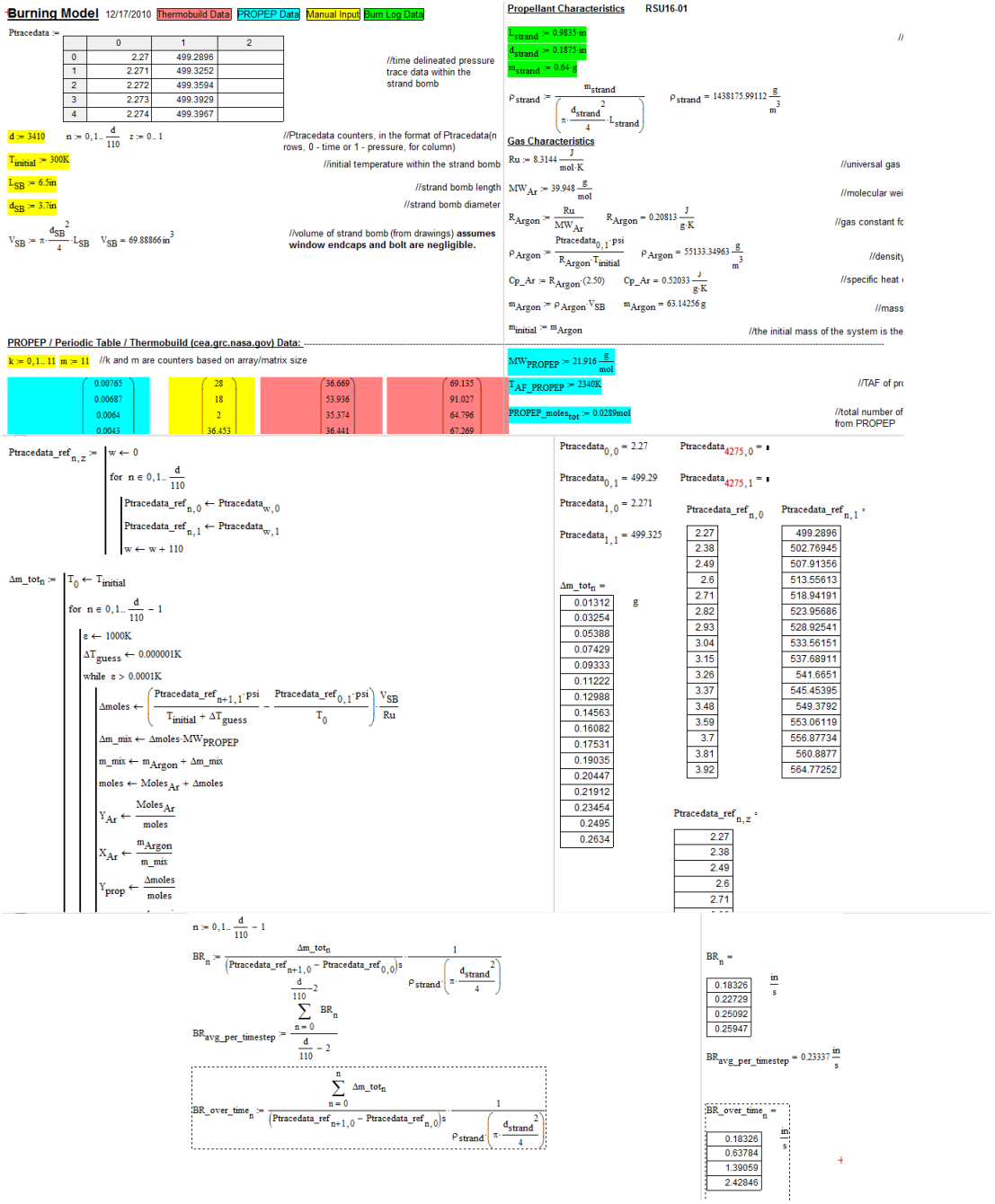

APPENDIX D

SAMPLE MATHCAD SPREADSHEET OF PROPELLANT COMBUSTION MODEL (MULTIMODAL)

Propellant Combustion Model V1.0 **07 / 13 / 10**

BDP Concept, Wide Dist., Multi-modal, AP Self-Deflagration, Separate Energy Balance

Binder Data

$\alpha_{binder} := 0.15$ //weight ratio of binder to oxidizer in the propellant

$\rho_{binder} := 0.95 \frac{g}{cm^3}$ //density of the binder from ProPEP and verified in a density converter

$E_{binder} := 15000 \frac{cal}{mol}$ //activation energy of the binder for surface decomposition in cal/mol

$A_{binder} := 3 \cdot 10^3 \frac{g}{cm^2 \cdot s}$ //Arrhenius frequency factor of the fuel in g/cm^2-sec 2.7 is Condon, 2.5 is BDP, 2.0 is Ras

$Q_{binder} := 50 \cdot \frac{cal}{g}$ //heat of pyrolysis (endothermic) (latent heat) of fuel in cal/g 1920 or 50 for SCC or BDP

Propellant Data:

$T_o := 298K$ //initial temperature of the propellant in C converted to K

$\rho_{prop} := 1.74 \cdot \frac{g}{cm^3}$

$D_{ox} := \begin{pmatrix} 20 \\ 200 \end{pmatrix} \cdot 10^{-6} \cdot m$ //an array of multiple diameters of oxidizer crystals before combustion in microns to create modal components (each a pseudo-propellant)

$j := 0..1$

$n := 1$

//an array of multiple ox to fuel ratios for each pseudo-propellant. The ratios are influenced by method from Gross and Beckstead (2009). The ox-to-fuel ratio is assumed to remain constant with propellant ox-to-fuel mass fractions.

$ox\_to\_binder\_ratio_j := \left(\frac{D_{ox_j}}{\alpha_{binder}}\right) \cdot \sum_{j=0}^{n} \left(\frac{\alpha_{ox}}{D_{ox_j}}\right)$

$ox\_to\_binder\_ratio = \begin{pmatrix} 6.23333 \\ 62.33333 \end{pmatrix}$

$volume\_ratio\_ox := \frac{\rho_{prop}}{\rho_{ox}} \cdot \alpha_{ox}$ $volume\_ratio\_ox = 0.77842$

$volume\_ratio\_binder := 1 - volume\_ratio\_ox$ $volume\_ratio\_binder = 0.22158$

$volume\_ratio\_pseudo\_prop_j := \frac{D_{ox_j}}{\sum_{j=0}^{n} D_{ox_j}} \cdot volume\_ratio\_ox$

$volume\_ratio\_pseudo\_prop = \begin{pmatrix} 0.70766 \end{pmatrix}$

Determination of Flame Standoff, Temperature, Mass loss, and Burning Rate via Iteration

Basic Calculations/Data outside of Iteration:

$\phi_1 := 3.83$ //first root of the first-order Bessel function - 3.83

$b_j := \frac{D_{ox_j}}{\sqrt{6}} \left[1 + \frac{\left(\frac{\rho_{ox}}{\rho_{binder}}\right)}{ox\_to\_binder\_ratio_j}\right]$ //characteristic dimension of the surface for each pseudo-propellant in m

$b = \begin{pmatrix} 1.07847 \times 10^{-5} \\ 8.42694 \times 10^{-5} \end{pmatrix} m$

Iteration Defining Parameters:

$P := 500psi$ //pressure of the system in psi

$T\_surface\_ox := 875.35K$ //guessed surface temperature of the oxidizer crystal in K

$C_{ign} := 10^{-9} \frac{s}{m^2}$ $t_{ign} := C_{ign} \cdot (D_{ox})^2 \cdot \exp\left(\frac{E_{ox}}{Ru \cdot T\_surface\_ox}\right)$ //ignition delay time - equation from 1977 Beckstead paper

$sosf := 5.83$ //guess sf/so for iteration

Flame Parameters

$C_g := 0.308 \frac{cal}{g \cdot K}$ //specific heat in cal/g-K of oxidizer combustion gases

$C_s := 0.3903 \frac{cal}{g \cdot K}$ //specific heat in cal/g-K of oxidizer solid phase

$\delta_{PF} := 1.5$ //reaction order in primary flame

$k_{PF} := 40 \frac{g}{cm^3 \cdot s \cdot atm^{\delta_{PF}}}$ //reaction rate constant for primary flame in gram/(cm^3-sec-atmδ)

$T_{AF} := 2850 \cdot K$ //adiabatic flame temperature of the propellant mixture,

$\delta_{AP} := 1.8$ //reaction order in AP/monopropellant flame

$T_{AP} := 1405K$ //combustion temp of the AP/oxidizer (and AP flame - adiabatic flame struct)

$E_{AP} := 30000 \frac{cal}{mol}$ //activation energy of AP (gas phase - in AP flame) in cal/mol

$A_{AP} := 54543 \frac{g}{cm^3 \cdot s \cdot atm^2}$ //Arrhenius frequency factor of the AP flame in g/cm^3-sec-atm^2

AP/Oxidizer Data

$A_s := 1.01882 \cdot 2.5004 \cdot 10^7 \frac{g}{cm^2 \cdot s}$ //Arrhenius frequency factor of the condensed oxidizer in g/cm^2-sec

$\alpha_{ox} := 1 - \alpha_{binder}$ //weight ratio of oxidizer to fuel in the propellant

$E_{ox} := 32000 \frac{cal}{mol}$ //activation energy for the combustion of the AP/oxidizer in cal/mol

$A_{ox} := 1.5665 \cdot 10^8 \frac{g}{cm^2 \cdot s}$ //Arrhenius frequency factor of the oxidizer in g/cm^2-sec

$\rho_{ox} := 1.9 \cdot \frac{g}{cm^3}$ //density of the AP/oxidizer from ProPEP and verified in a density converter

$E_s := 30000 \frac{cal}{mol}$ //activation energy for the combustion of the AP/oxidizer (condensed phase) in cal/mol

$\lambda_g := 0.29 \frac{W}{m \cdot K}$ //thermal conductivity of oxidizer gas in cal/(cm-sec-K)

$\Delta H_s := 138.5 \frac{cal}{g}$ //latent heat of solid AP

$\Delta H_{ev} := 526.5 \frac{cal}{g}$ //AP heat of vaporization at 298K

$\Delta H_g := 142.59 \frac{cal}{g}$ //latent heat of AP decomposition products

$A_{fh} := 0.3$ //ratio of peak diffusional distance to the effective heat transfer distance of the diffusional flame centered over the AP crystal

$B_{fh} := A_{fh} \cdot \left(\frac{1}{8}\right)$ //ratio of peak diffusional distance to the effective heat transfer distance of the diffusional flame centered over the binder - should be smaller than Afh - using half of Afh as a correlation to the heat flux mentioned in Gross & Beckstead (2009) or using 1/8Afh

$\begin{pmatrix} 3.95068 \times 10^{-11} \end{pmatrix}$

Mass Flux / Linear Burning Rate Calculations:

$$mflux_{ox} := A_{ox}\cdot\exp\left(\frac{-E_{ox}}{Ru\cdot T\_surface\_ox}\right)$$

$$mflux_{binder} := mflux_{ox}\, sosf\cdot\left(\frac{\alpha_{binder}}{\alpha_{ox}}\right)$$

$$r_{ox} := \frac{mflux_{ox}}{\rho_{ox}} \qquad r_{binder} := \frac{mflux_{binder}}{\rho_{binder}}$$

$$\beta_p := 1 - \frac{A_s\cdot\exp\left(\frac{-E_s}{Ru\cdot T\_surface\_ox}\right)}{mflux_{ox}}$$

$$Q_F := C_g\cdot\left(T_{AP} - T_{ref}\right) - C_s\cdot\left(T_o - T_{ref}\right) + \Delta H_g \quad \text{//heat content of adiabatic AP flame}$$

$$Q_L := \beta_p\cdot\left(\Delta H_{ev} - \Delta H_g\right) - \left(1 - \beta_p\right)\cdot Q_F \quad \text{//heat of gasification (latent heat) of AP/oxidizer in cal/g}$$

$$Q_{AP} := Q_F + Q_L \quad \text{//heat of release of AP flame in cal/g}$$

$$Q_{PF} := C_g\cdot\left(T_{AF} - T_o\right) + \alpha_{ox}\cdot Q_L + \left(1 - \alpha_{ox}\right)\cdot Q_{binder} \quad \text{//heat of release of Primary Flame in cal/g}$$

$$T\_surface\_binder := \frac{-E_{binder}}{\left(\ln\left(\frac{mflux_{binder}}{A_{binder}}\right)\cdot Ru\right)}$$

$$geo\_factor_P := \frac{1}{2}\left(1 + \frac{1}{\sqrt{3}}\right)\left(1 - \frac{r_{ox}}{r_{binder}}\right) + r_{ox}\cdot\frac{t_{ign_n}}{D_{ox}}$$

$$geo\_factor_N := \frac{1}{2}\left(1 - \frac{1}{\sqrt{3}}\right)\left(1 - \frac{r_{ox}}{r_{binder}}\right) + r_{ox}\cdot\frac{t_{ign_n}}{D_{ox}}$$

$$surface\_area_{ox} := \overrightarrow{\left[volume\_ratio\_pseudo\_prop\cdot\left[volume\_ratio_{ox} + 3\cdot volume\_ratio_{ox}\left[\left(geo\_factor_P\right)^2\right] + \left[\left(geo\_factor_N\right)^2\right]\right]\right]}$$

$$surface\_area_{ox\_check} := volume\_ratio\_pseudo\_prop\cdot\left[volume\_ratio_{ox} + 3\cdot volume\_ratio_{ox}\left[\left(geo\_factor_P\right)^2\right] + \left[\left(geo\_factor_N\right)^2\right]\right]$$

$$surface\_area_{binder} := volume\_ratio\_pseudo\_prop\cdot volume\_ratio_{binder}$$

$$surface\_area_{binder\_check} := volume\_ratio\_pseudo\_prop_n\cdot volume\_ratio_{binder}$$

$$total\_surface\_area := \overrightarrow{\left[volume\_ratio\_pseudo\_prop\cdot\left[1 + 3\cdot volume\_ratio_{ox}\left[\left(geo\_factor_P\right)^2\right] + \left[\left(geo\_factor_N\right)^2\right]\right]\right]}$$

$$mflux\_prop_{n-1} := \sum_{j=0}^{n-1}\left(mflux_{ox}\cdot surface\_area_{ox_j} + mflux_{binder}\cdot surface\_area_{binder_j}\right)$$

$$mflux\_prop_n := \frac{mflux_{ox}\cdot surface\_area_{ox_n} + mflux_{binder}\cdot surface\_area_{binder_n} + mflux\_prop_{n-1}\cdot\left(\sum_{j=0}^{n-1} total\_surface\_area_j\right)}{\sum_{j=0}^{n} total\_surface\_area_j}$$

Flame Standoff Distance Calculations

$$X_{D\_star} := A_{fh}\cdot b\cdot\left(\frac{1 - \alpha_{ox}}{\alpha_{ox}}\right)\cdot\phi_1 \quad \text{//diffusion flame height}$$

$$X_{Dox} := X_{D\_star}\cdot A_{fh} \quad \text{//diffusion flame height situated over oxidizer crystal}$$

$$X_{Dbinder} := X_{D\_star}\cdot B_{fh} \quad \text{//diffusion flame height situated over binder}$$

$$t_{ign} = \begin{pmatrix} \\ 3.95068\times10^{-9} \end{pmatrix} s$$

from Cohen technical meeting paper

$$mflux_{ox} = 1.58606\ \frac{g}{cm^2\cdot s}$$

$$mflux_{binder} = 1.63177\ \frac{g}{cm^2\cdot s}$$

$$r_{ox} = 0.32865\ \frac{in}{s} \qquad r_{binder} = 0.67624\ \frac{in}{s}$$

$$\beta_p = 0.48615$$

$$Q_F = 483.546\ \frac{cal}{g}$$

$$Q_L = -61.83577\ \frac{cal}{g}$$

$$Q_{AP} = 421.71023\ \frac{cal}{g}$$

$$Q_{PF} = 740.9556\ \frac{cal}{g}$$

$$T\_surface\_binder = 1.00487\times10^3\ K$$

$$geo\_factor_P = \begin{pmatrix} 0.40539 \\ 0.40539 \end{pmatrix}$$

$$geo\_factor_N = \begin{pmatrix} 0.10862 \\ 0.10862 \end{pmatrix}$$

//surface area of oxidizer pseudo-propellant, appears to be a ratio

$$surface\_area_{ox} = \begin{pmatrix} 0.08308 \\ 0.83078 \end{pmatrix}$$

$$surface\_area_{binder} = \begin{pmatrix} 0.01568 \\ 0.1568 \end{pmatrix}$$

$$\frac{surface\_area_{ox\_check}}{surface\_area_{binder\_check}} = 5.82813$$

$$total\_surface\_area = \begin{pmatrix} 0.09876 \\ 0.98758 \end{pmatrix}$$

$$mflux\_prop_{n-1} = 0.15735\ \frac{g}{cm^2\cdot s}$$

//total mass flux for various AP sizes of n-1, used when applicable

//total mass flux across entire propellant surface, using Ox parameters

$$mflux\_prop_n = 1.46277\ \frac{g}{cm^2\cdot s}$$

$$X_{D\_star} = \begin{pmatrix} 2.18676\times10^{-6} \\ 1.70869\times10^{-5} \end{pmatrix} m$$

$$X_{Dox} = \begin{pmatrix} 6.56029\times10^{-7} \\ \end{pmatrix} m$$

$$X_{Dbinder} = \begin{pmatrix} 8.20037\times10^{-8} \\ 6.40758\times10^{-7} \end{pmatrix} m$$

$$X_{ox\_star} := \frac{mflux_{ox}}{A_{AP} \cdot \exp\left(\frac{-E_{AP}}{Ru \cdot T_{AP}}\right) \cdot P^2}$$ //flame standoff distance for the AP/monopropellant flame

$X_{ox\_star} = 1.17375 \times 10^{-5}\,m$

$$\zeta PF\_binder := \frac{C_s \cdot mflux\_prop_n \cdot \left(X_{PF\_star} + X_{Dbinder}\right)}{\lambda_g}$$ //dimensionless flame height over binder

$$\zeta PF\_ox := \frac{C_s \cdot mflux\_prop_n \cdot \left(X_{ox\_star} + X_{Dox}\right)}{\lambda_g}$$ //dimensionless flame height over oxidizer

$\zeta PF\_binder = \begin{pmatrix} 0.15865 \\ 0.2047 \end{pmatrix}$ $\exp(-\zeta PF\_binder) = \begin{pmatrix} 0.8533 \\ 0.81489 \end{pmatrix}$

$\zeta PF\_ox = \begin{pmatrix} 1.02154 \\ 1.38998 \end{pmatrix}$

$$\zeta ox := \frac{C_g}{\lambda_g} \cdot mflux_{ox} \cdot X_{ox\_star}$$

$\zeta ox = 0.82781$

$$X_{PDF\_star} := X_{PF\_star} + X_{Dbinder}$$

$X_{PDF\_star} = \begin{pmatrix} 1.92472 \times 10^{-6} \\ 2.48347 \times 10^{-6} \end{pmatrix} m$

$$\beta_F := \frac{X_{ox\_star} - X_{PF\_star}}{X_{PDF\_star}} \cdot A_{fh}$$ //fraction of reactants involved in primary diffusion flame

$\beta_F = \begin{pmatrix} 1.54226 \\ 1.19527 \end{pmatrix}$

Temperature/Energy / Burning Rate Calculations:

$$\beta_{ox} := 1 - \frac{\left[mflux_{binder} \cdot surface\_area\_binder \cdot \left[C_s \cdot \left(T\_surface\_binder - T_o\right) + Q_{binder}\right]\right]}{\left(mflux_{ox} \cdot surface\_area\_ox + mflux_{binder} \cdot surface\_area\_binder\right) \cdot Q_{PF} \cdot \exp(-\zeta PF\_binder)}$$

$\beta_{ox} = \begin{pmatrix} 0.99206 \\ 0.92056 \end{pmatrix}$

$$T\_surface\_check\_ox_n := T_o + \frac{\beta_{ox_n} \cdot \frac{\beta_{F_n}}{A_{fh}} \cdot \left(mflux_{ox} \cdot surface\_area\_ox_n + mflux_{binder} \cdot surface\_area\_binder_n\right) \cdot Q_{PF} \cdot \exp\left(-\zeta PF\_ox_n\right) + \beta_{ox_n} \cdot \left(1 - \frac{\beta_{F_n}}{A_{fh}}\right) \cdot Q_{AP} \cdot mflux_{ox} \cdot surface\_area\_ox_n \cdot \exp(-\zeta ox)}{C_s \cdot mflux_{ox} \cdot surface\_area\_ox_n} - \frac{\Delta H_s + Q_L}{C_s}$$

$T\_surface\_check\_ox_n = 875.52049\,K$

$$BR := \frac{mflux\_prop_n}{\rho_{prop}}$$

$BR = 0.33097\,\frac{in}{s}$

APPENDIX E

TYPICAL COMBUSTION MODEL INPUT PARAMETERS FOR 80/20 AP/HTPB PROPELLANT

Binder Parameters	Oxidizer Parameters
α_{binder} = 0.2 ρ_{binder} = 0.95 g/cm^3 E_{binder} = 62.8 x 10^3 J/mol A_{binder} = 3 x 10^3 g/cm^2-s Q_{binder} = 50 cal/g	C_g= 0.308 cal/g-K C_s= 0.3903 cal/g-K A_s= 2.5 x 10^7 g/cm^2-s α_{ox} = 0.8 E_{ox}= 134 x 10^3 J/mol A_{ox}= 1.5665 x 10^8 g/cm^2-s ρ_{ox}=1.95 g/cm^3 E_s= 125.6 x 10^3 J/mol λ_g = 0.3 W/m-K ΔH_s = 138.5 cal/g ΔH_{ev} = 526.5 cal/g ΔH_g = 142.59 cal/g

Flame Parameters	Propellant Parameters
δ_{PF} = 1.5 $k_{PF} = 40 \ \frac{g}{cm^3 atm^{\delta_{PF}} s}$ T_{AF} = 2350 K T_{AP} = 1400 K E_{AP} = 30000 cal/mol A_{AP} = 54543 g/cm^3-s-atm^2	T_o = 300 K T_{ref} = 298 K $\rho_{prop} = 1.59 \ \frac{g}{cm^3}$ D_{ox} = 200 mm

APPENDIX F

CALCUATED COMBUSTION MODEL PARAMETERS FOR

80/20 AP/HTPB PROPELLANT

Binder Parameters (In process)	Oxidizer Parameters (In process)
α_{binder} = 0.2 ρ_{binder} = 0.95 g/cm^3 E_{binder} = 62.8 x 10^3 J/mol A_{binder} = 3 x 10^3 g/cm^2-s Q_{binder} = 50 cal/g	C_g= 0.308 cal/g-K C_s= 0.3903 cal/g-K A_s= 2.5 x 10^7 g/cm^2-s α_{ox} = 0.8 E_{ox}= 134 x 10^3 J/mol A_{ox}= 1.5665 x 10^8 g/cm^2-s ρ_{ox}=1.95 g/cm^3 E_s= 125.6 x 10^3 J/mol λ_g = 0.3 W/m-K ΔH_s = 138.5 cal/g ΔH_{ev} = 526.5 cal/g ΔH_g = 142.59 cal/g

Flame Parameters (In process)	Propellant Parameters (In process)
δ_{PF} = 1.5 k_{PF} = 40 $\frac{g}{cm^3 atm^{\delta_{PF}} s}$ T_{AF} = 2350 K T_{AP} = 1400 K E_{AP} = 30000 cal/mol A_{AP} = 54543 g/cm^3-s-atm^2	T_o = 300 K T_{ref} = 298 K ρ_{prop} = 1.59 $\frac{g}{cm^3}$ D_{ox} = 200 mm

APPENDIX G

FLAME ENERGY FLUX DIAGRAM

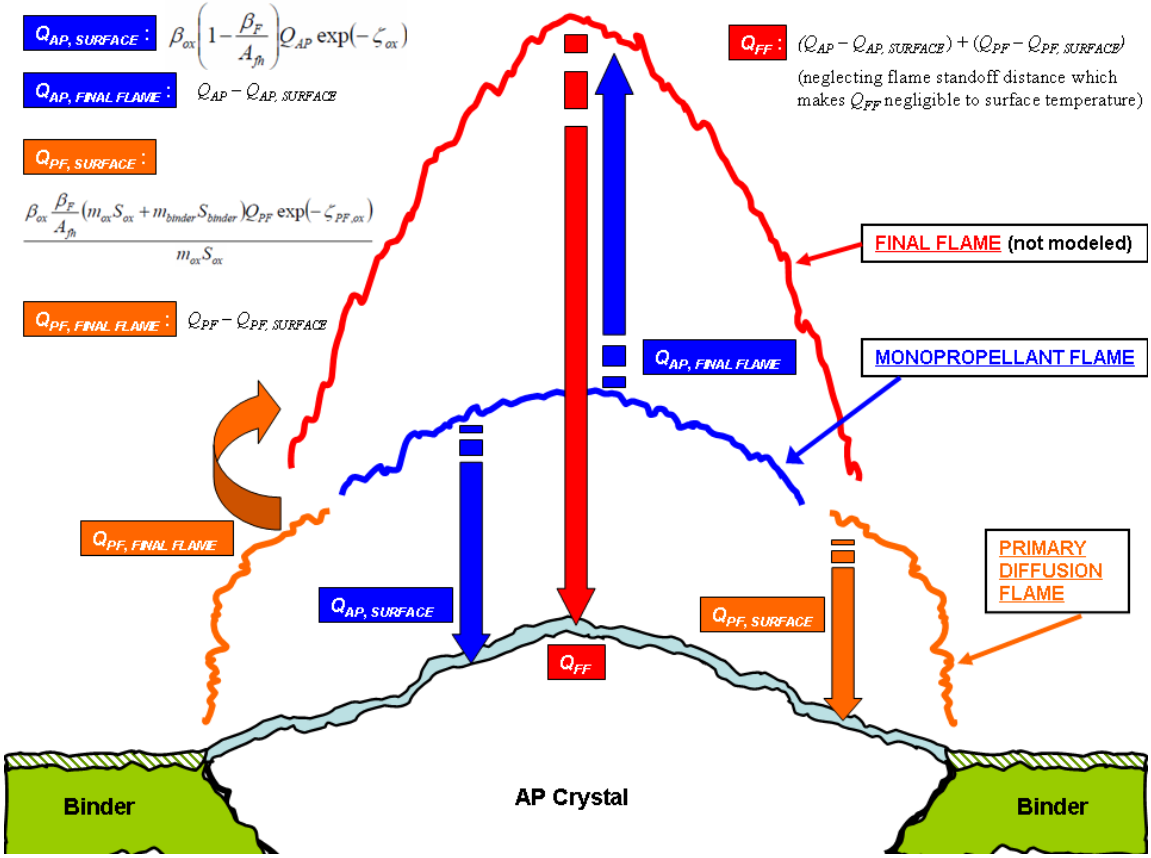

VITA

Name:	Corey Anthony Frazier
Address:	3123 TAMU College Station, TX 77843
Email Address:	corey_fraz@yahoo.com
Education:	B.S., Aerospace Engineering, University of Central Florida, 2004 M.S., Mechanical Engineering, University of Central Florida, 2007